第 22 回
核燃焼プラズマ
統合コード研究会

22nd Burning Plasma Simulation Initiative (BPSI) Meeting

日時：2024 年 12 月 19 日(木)－20 日(金)
場所：九州大学筑紫キャンパス応用力学研究所
2 階大会議室　および　オンライン

(Ver. 1, 2025 年 2 月 28 日発行)

合同会合

第 22 回核燃焼プラズマ統合コード研究会

22nd Burning Plasma Simulation Initiative (BPSI) Meeting

(Ver.2.1)

日時：2024 年 12 月 19 日(木)－20 日(金)
場所：九州大学筑紫キャンパス　応用力学研究所 2 階大会議室　および　オンライン

12 月 19 日(木)

12:45 – 13:00　会議登録 Registration
13:00 – 13:05　事務連絡 Business announcement
13:05 – 13:10　はじめに（村上) Opening remark

(座長：村上)
13:10 – 13:35　講演 1-1　本多（京大)
Progress and future development of the integrated model GOTRESS+
13:35 – 14:00　講演 1-2　福山（京大)
Progress and issues of integrated code TASK for magnetically-confined plasmas
14:00 – 14:25　講演 1-3　糟谷（九大)
Transport simulation for control of multiple kinds of impurities by using integrated code TASK

14:25 – 14:45　集合写真 group photo、休憩 break

(座長：糟谷)
14:45 – 15:10　講演 1-4　Hahm (SNU)
Zonal flow dynamics in the presence of fast ions
15:10 – 15:30　講演 1-5　田原（京大)
Kinetic modeling for energetic particle transport induced by electrostatic and magnetic fluctuations
15:30 – 15:55　講演 1-6　村上（京大)
Multiple resonance heating and supra-thermal electron behaviors in QUEST

15:55 – 16:05　休憩 break

(座長：本多)
16:05 – 16:30　講演 1-7　相羽（量研) online
Status of operation scenario development for JT-60SA initial research phase
16:30 – 16:45　講演 1-8　桑宮（九大)
Diagnostic simulation of experimental measurement of density fluctuations in

tokamak plasma by phase contrast imaging using a gyrokinetic simulation code

16:45 – 17:00　講演 1-9　　　堀岡（京大）

Integrated transport simulation of pellet injection discharge in LHD

17:00 – 17:15　講演 1-10　　　可児（名大）

Investigation of multivariable control gain for fusion power and electron density control by NB injection power and pellet injection using TOTAL

17:15 – 17:40　講演 1-11　　　横山（核融合研）online

Information from IMEG

17:40　散会

18:00 – 20:30　懇親会（独楽蔵　JR 大野城駅近）

12 月 20 日(金)

(座長：福山)

9:00 – 9:25　講演 2-1　河村（量研）

Recent progress of JA-DEMO divertor modeling by SOLPS-ITER

9:25 – 9:50　講演 2-2　Si (量研)

SOLPS-ITER simulation study for power exhaust in JA-DEMO divertor

9:50 – 10:15　講演 2-3　Wisitsorasak (KMUTT)

Development of Core-SOL-Divertor model for simulating tokamak with impurities

10:15 – 10:40　講演 2-4　矢本（量研) online

Kinetic modelling of W impurity transport in SOL/divertor plasmas by IMPGYRO code

10:40 – 10:50　休憩

(座長：河村)

10:50 – 11:15　講演 2-5　Choi (KAIST)

Physics study of confinement enhancement in KSTAR FIRE mode

11:15 – 11:35　講演 2-6　Chen (USTC)

Electromagnetic geodesic acoustic modes in up-down asymmetric tokamaks

11:35 – 11:55　講演 2-7　小山（九大)

Short-wavelength fluctuations on high-confinement mode

11:55 – 12:10　講演 2-8　宮本（九大)

Excitation of inward particle fluxes with nonlinear coupling and turbulence spreading in tokamak plasmas

12:10 – 13:10　昼休み Lunch break

(座長：森下)

13:10 – 13:35　講演 3-1　登田（核融合研)

Modeling of turbulent transport due to dissipative trapped electron mode in tokamak plasmas

13:35 – 13:50　講演 3-2　大谷（京大)

Automatic configuration of ECCD using genetic algorithm

13:50 – 14:05　講演 3-3　古田原（日大)

Particle and momentum transport analysis using multi-field singular value decomposition in plasma turbulence simulation

14:05 – 14:20　講演 3-4　川村（九大)

Analysis of MHD instabilities using mode decomposition in tokamak plasmas

14:20 – 14:30　休憩

（座長：登田）

14:30 – 14:55　講演 3-5　　　森下（京大）

Real-time prediction model and adaptive predictive control of LHD plasmas

14:55 – 15:10　講演 3-6　　　市川（京大）

Extension of the data assimilation system ASTI for the real time prediction of tokamak plasmas

15:10 – 15:25　講演 3-7　　　小澤（日大）

Nonlinear wave extraction of geodesic acoustic mode and turbulence modulation using conditional average method

15:25 – 15:40　講演 3-8　　　風見（日大）

Estimation of global turbulence profile from partial measurements using generative adversarial networks in fusion plasmas

(Session Leader：村上)

15:40 – 16:00　議論 Discussion

16:00 – 16:05　事務連絡 Business announcement

16:05　散会

Progress and future development of the integrated model GOTRESS+

M. Honda and R. Otani

Kyoto University, Nishikyo-ku, Kyoto 615-8530 Japan

GOTRESS / GOTRESS+ and their recent extension

In Japan, multiple integrated models for magnetic confinement fusion plasmas have been developed. Among them, we are developing a steady-state integrated model called GOTRESS+ [1], which has several unique features not found in other integrated models in Japan. These features include the incorporation of the EPED1 model for predicting pedestal width and height, the ability to directly obtain steady-state solutions, and the capability to stably run using the TGLF turbulent transport model.

GOTRESS+ is centered around the steady-state transport code GOTRESS, combined with equilibrium and current profile code ACCOME, neutral beam heating code OFMC, EPED1, and the ideal MHD stability analysis code MARG2D. Data exchange and workflow within the integrated model are managed by Python programs. GOTRESS+ has been successfully applied to the development of operational scenarios for JT-60SA [1] and JA-DEMO, a prototype reactor. In recent years, the number of users has been increasing at Kyoto University, Tottori University, and QST.

Recent advancements in GOTRESS include the introduction of an optimization method using a genetic algorithm to achieve the desired EC heating and current drive profile [2], the implementation of a dispersed initial value approach for the inherently sequential Nelder-Mead algorithm to select the most converged solution as the best solution, and the rewriting of GOTRESS's convergence algorithm using object-oriented programming in Fortran. With GOTRESS+, we successfully developed an MHD-stable operational scenario for JA-DEMO that satisfies most of the targeted figures of merit [2].

GOTRESS employs PIKAIA as the implementation of the genetic algorithm, enabling MPI parallel execution for each individual. For example, when using 100 individuals with 26 cores, one core is allocated to the host, while 25 cores are assigned to workers, resulting in each worker performing fitness calculations for four individuals. When combined with TGLF, which allows MPI parallel computation for each poloidal wavenumber, each worker calls 23 parallel instances of TGLF. This implementation is realized through MPMD (Multiple Program Multiple Data) [3]. In PIKAIA, the allocated MPI processes are efficiently utilized. However, when using the Nelder-Mead (NM) method, a global optimization technique that is not well-suited for MPI parallelization, the host and all workers perform the same optimization calculation, leading to inefficient use of computational resources. To address this, small perturbations are introduced to the initial values provided to the NM method, allowing all 26 cores to perform optimization calculations based on different initial values. The solution with the best fitness among them is adopted as the optimal solution. As a result, sufficient convergence of the temperature profile is achieved from the early stages of the iteration process in GOTRESS, shown in Fig. 1.

Surrogate modeling with Gaussian Process Regression (GPR)

A neural network model-based turbulent transport surrogate model [3] has issues with the inability to assess confidential interval and the unpredictability of performance when extrapolated. Therefore, we are attempting to create a surrogate model by utilizing the GPR method for probabilistically modeling the nonlinear relationship between input variables x and output variables y (a method for estimating the probability distribution of a function from data). The surrogate model based on GPR has advantages and disadvantages that contrast with those of neural network-based surrogate models. GPR performs well with a small amount of data and allows for the identification of confidence intervals. However, it faces challenges such as high computational costs when dealing with high-dimensional inputs and outputs or large datasets, as well as arbitrariness in kernel selection.

Focusing on the deep neural network (NN) kernels recently proposed, which incorporate the characteristics of NN models with multiple hidden layers into the kernel, we are developing an in-house GPR program called *dgpr* for implementing these NN kernels. In addition to possessing almost all the standard features typically found in GPR programs, *dgpr* utilizes the JAX library, enabling the use of automatic differentiation during hyperparameter optimization.

A dataset of 5,002 samples was prepared using 23-dimensional inputs and 2-dimensional outputs (electron and ion heat fluxes, Q_e and Q_i) generated by TGLF in GOTRESS. For training the GPR surrogate model with a NN kernel using ReLU as the activation function, 4,501 data points were used for training, and 501 for testing. As a comparison, a NN surrogate model was also constructed using the same dataset.

The prediction performance of both models on the test data was evaluated for Q_e and Q_i. The coefficient of determination R^2 for Q_e was 0.9996 for the GPR model and 0.9974 for the NN model. For Q_i, it was 0.9986 for the former and 0.9877 for the latter, demonstrating that the GPR surrogate model outperformed the NN surrogate model. In addition to good performance, the GPR model allows for confidence interval estimation, and the deviation in predictions for outliers is notably reduced. We plan to implement a GPR surrogate model into GOTRESS.

References

[1] M. Honda et al., Nucl. Fusion **61**, 116029 (2021).

[2] R. Otani et al., The 22nd BPSI Workshop, 3-2, RIAM, Kyushu Univ. (2024).

[3] M. Honda and E. Narita, Phys. Plasmas **26**, 102307 (2019).

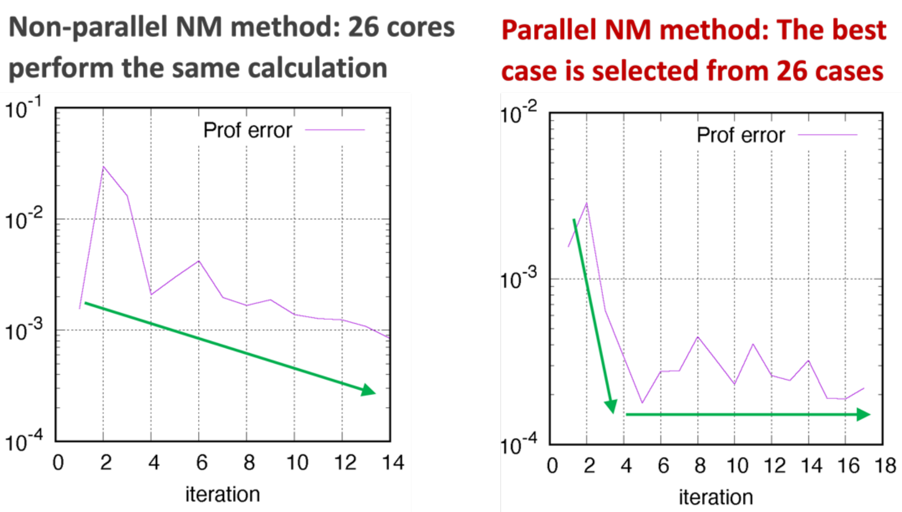

Fig. 1: Left Figure: Result of NM optimization where all processes use the same initial values. The convergence of profile error is slow. Right Figure: Result of NM optimization where the best solution is selected from calculations with perturbed initial values. The profiile error quickly reaches a sufficient level.

Progress and issues of integrated code TASK for magnetically-confined plasmas

Atsushi Fukuyama
Professor Emeritus, Kyoto University, Kyoto, Japan

The present status of the module structure of TASK is shown in Fig.1.

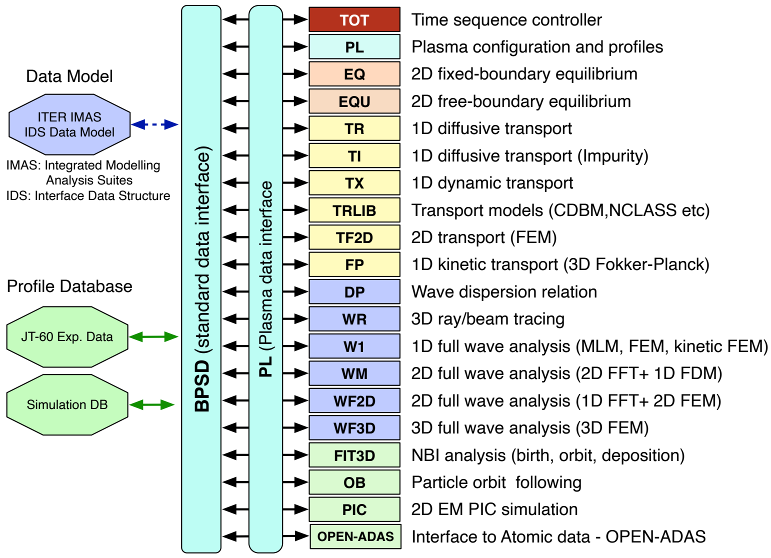

Fig.1: Module structure of TASK on 2024

Recent updates of TASK includes

- PL (plasma status): The particle species data have been extended to include the atomic number in addition to the atomic mass number and the charge state number so that the isotopes are identified.
- TR (core transport): More fusion processes, such as T-T and T-He_3, have been included so that D-D start up is fully described.
- FP (kinetic transport): Finite-orbit-width effects developed by Ota (Kyoto-U) are included.
- DP (dielectric tensor): Ring velocity distribution for NBI-heated plasma has been included.
- WR (ray tracing): Absorption at the relativistic cyclotron resonance resonance in toroidal plasmas has been corrected.

For kinetic full-wave analyses in hot plasmas, formulation of integral form of dielectric tensor and implementation to full-wave codes using the finite element analysis (FEM) are in progress. This scheme can be applied to describe waves with short wave length, such as Bernstein waves, and in the presence of energetic ions, and the effects of inhomogeneous magnetic field strength along the field line. The integral form of dielectric tensor can be obtained by replacing the velocity integral by positional integral along the particle orbit. For plasmas with Maxwellian velocity distributions, two types of kernel functions have been derived: the plasma dispersion kernel function (PDKF) for parallel motion and the plasma gyro kernel function (PGKF). Recently PDKF has been extended to parabolic inhomogeneity of magnetic field strength along the field line for describing toroidal plasmas where the magnetic field strength changes on a magnetic surface.

The kinetic full-wave analyses with one-dimensional inhomogeneity have applied to various cases:

- Unmagnetized case: Resonant laser-plasma interaction: For weak density gradient, analytical estimate of absorption rate is reproduced. For steep density gradient, stochastic heating appears even in the normal incident angle.
- Linear dependence of magnetic field strength: magnetic beach heating: Right-hand circularly polarized wave is absorbed before the wave arrives at the electron cyclotron resonance.
- Perpendicular to the magnetic field: Mode conversion to the Bernstein waves: In tokamak configuration, the ordinary (O) mode with optimum injection from the low field side is converted to the extraordinary (X) mode. The X mode is reflected as the backward shorter-wavelength X mode, reflected again near the upper hybrid resonance, mode-converted to the electron Bernstein wave, and finally absorbed near the electron cyclotron resonance. Fig.2 shows the sensitive dependence on the collision frequency of the wave and power deposition radial structure for the optimum injection case. Fig.3 shows the two-dimensional wave structure on horizontal plane resonance. In this case, tunneling and reflection of the waves with non-optimum injection angle are included.

Further extensions, such as implementation of IMAS interface for ITER, integration with AI and data-driven science, and coupling with reactor design, are in consideration.

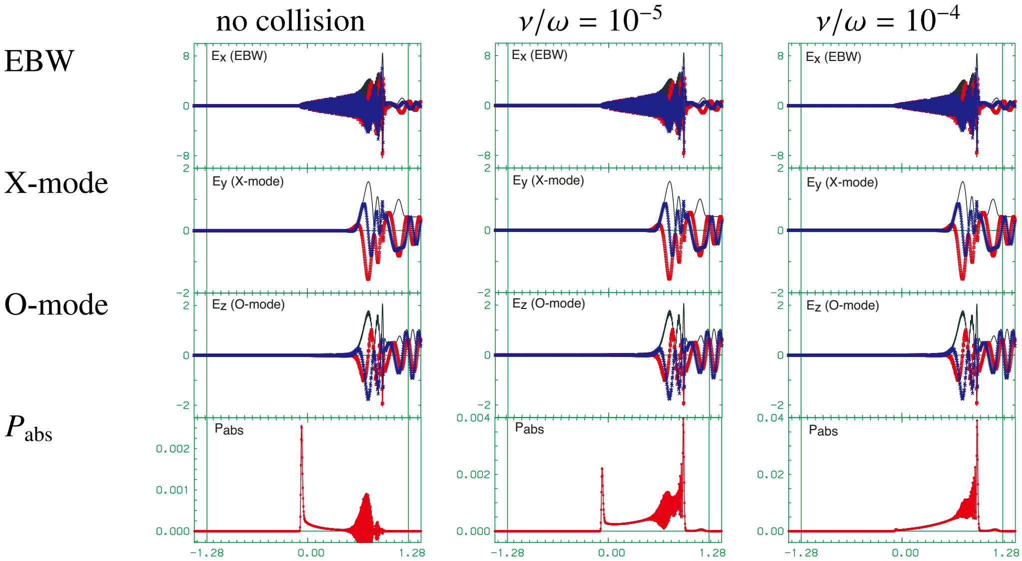

Fig.2: Competition of collisional and cyclotron duping

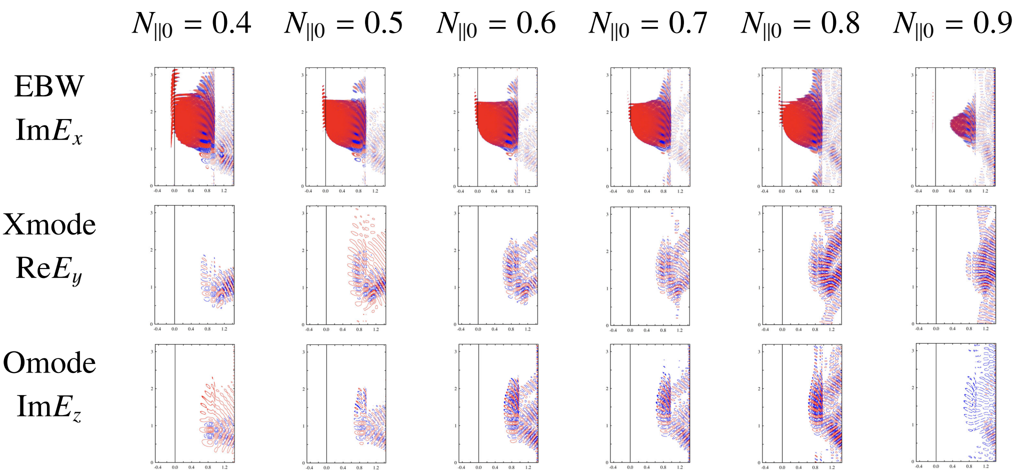

Fig.3: 2D kinetic analysis of O-X-B mode conversion in tokamak configuration

統合コードTASKを用いた複数種不純物制御のための輸送シミュレーション

Transport simulation for control of multiple kinds of impurities by using integrated code TASK

N. Kasuya[1,2], Y. Kawamura[2], A. Fukuyama[3], M. Yagi[4]

[1]RIAM, Kyushu University, Kasuga, Fukuoka, Japan

[2]IGSES, Kyushu University, Kasuga, Fukuoka, Japan

[3]Professor Emeritus, Kyoto University, Kyoto, Japan

[4]National Institute for Quantum and Radiological Science and Technology, Rokkasho, Aomori, Japan

E-mail: kasuya@riam.kyushu-u.ac.jp

1. Introduction

In tokamak devices, high-z impurities such as tungsten arising from a tokamak wall can merge into the core plasma, which significantly affect the plasma performance by radiation losses. In addition, argon and neon gases are used for thermal control in the scrape-off layer region, so their effect on the core plasma also should be evaluated. It is known that RF heating is effective for impurity control in the core region [1]. In that impurity transport process, neoclassical transport plays an important role [2]. The objective of this study is to evaluate the transport of many kinds of impurities in the core plasma using the integrated code TASK [3] to examine high-temperature plasma discharge scenarios. Using the developed transport calculation scheme [4], coupled transport calculation with bulk plasma and impurities are caried out for large experimental tokamak and future-generation tokamak plasmas.

2. Integrated simulation code TASK

TASK code consists of modular codes simulating equilibrium, transport, wave heating, energetic particle behavior, etc., and combination of these modules gives integrated transport analysis. In TASK code, a data exchange interface BPSD links several modules to make possible to carry out self-consistent simulations. TR module is mainly used to calculate the transport processes of the main plasma components (ions and electrons). TI module is for impurity transport, which calculates the transport processes of impurities of various charge numbers, including neoclassical, turbulent, and atomic processes. The transport coefficients for neoclassical transport are evaluated using NCLASS routine [5]. The coefficients for ionization and recombination of impurity ions are obtained from OPEN-ADAS database [6]. The code can be applied to analyze impurity transport dynamics during the formation of internal transport barriers [4].

3. Multiple kinds of impurity profiles

Core plasma impurity transport calculations are carried out by using TASK code with inclusion of high-Z tungsten, and mid-Z argon and neon. We aim to consider the impurity profiles under the experimental plasma profile in a large tokamak device, and those self-consistently determined by calculation of bulk and impurity plasma profiles. The effect of plasma rotation [4] is not considered here. For the impurity under the experimental plasma profile, the background plasma profile is fixed to that observed in JET tokamak device, and the steady-state impurity profiles are compared when tungsten (W), argon (Ar), and neon (Ne) are coming into the core from the plasma edge. The calculation results were checked in the case with one impurity species and with three impurity species calculated simultaneously. Figure 1 shows the radial profiles of the averaged charge number and line-radiation power for each ion species. This is the calculation result under the background plasma profile at the time when density peaking of the impurities does not arise in the center of the plasma. The comparison shows the same levels of the impurity ion density. The radiation power of W is dominant in the core plasma region, where W impurities are not fully ionized. On the other hand, the radiation power near the edge region is comparable for the three impurity species.

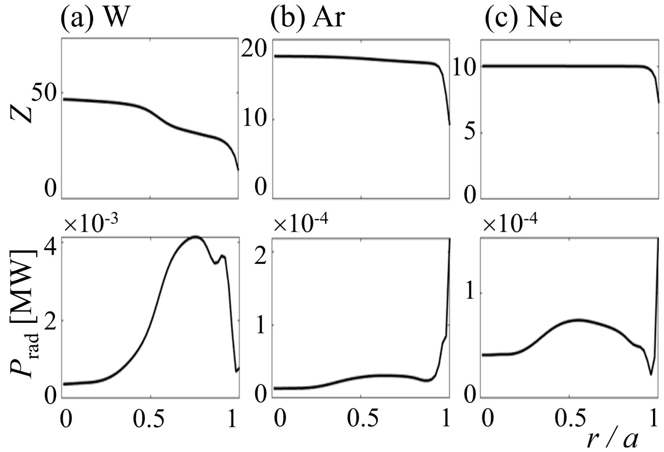

FIG. 1. Radial profiles of the averaged charge number and line-radiation power of impurities (a) W, (b) Ar, and (c) Ne calculated with experimental temperature and density profiles in JET.

For the self-consistent bulk and impurity profile calculation, a coupled calculation was carried out for the advanced scenario [7], in which an internal transport barrier is formed by additional lower hybrid wave heating LH with current drive. In the hybrid scenario, the bootstrap current fraction is increased by central heating, and in the advanced scenario, a negative magnetic shear region is created with LH local current drive in addition to the hybrid scenario (Fig. 2). Here, the current diffusive ballooning mode (CDBM) model is used for turbulent transport. The decrease in the magnetic shear leads to a decrease in the diffusion coefficient, which forms an internal transport barrier (ITB). The radiation power is reduced by about 10% after the additional LH (Fig. 2(f)).

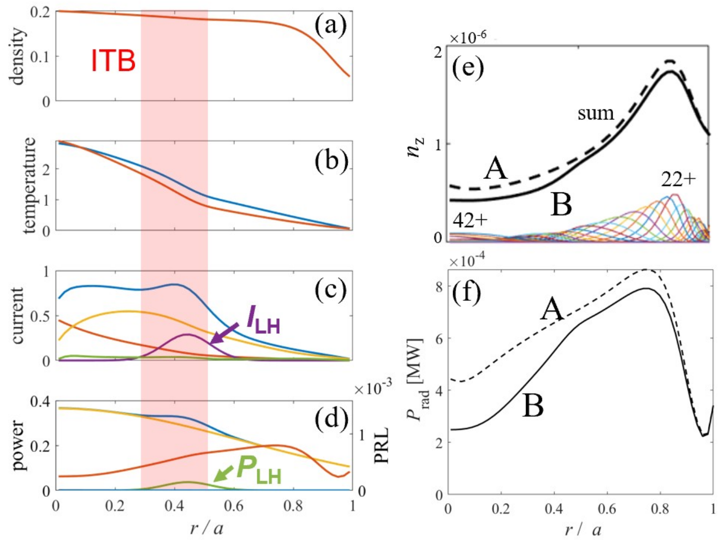

FIG. 2. (a) Density, (b) temperature, (c) plasma current, and (d) heating power profiles during the advanced mode. The ITB is formed in the area with red color. (e) Tungsten density (for each valence ion, and total) and (f) radiation power profiles, before (A) and after (B) ITB formation.

Transport calculations including burning reactions were also performed with the parameter set of ITER tokamak device. To see the impurity dynamics, response to a pulsed increase in the amount of impurity is investigated by entering Ne impurity from the plasma edge at the steady state (Fig. 3). This assumes the case with an impurity puff for thermal control of the diverter region. Increasing the impurity density at the periphery by a factor of 30 leads to a decrease in the plasma temperature in this region, which in turn increases the plasma density gradient, and the plasma density for the whole region including the central region (Fig. 3(f)). Then, the central plasma temperature also increases because the burning reaction is accelerated by the increase of the density (Fig. 3(e)). The edge impurity gives the global plasma response to increase both density and temperature in the core region.

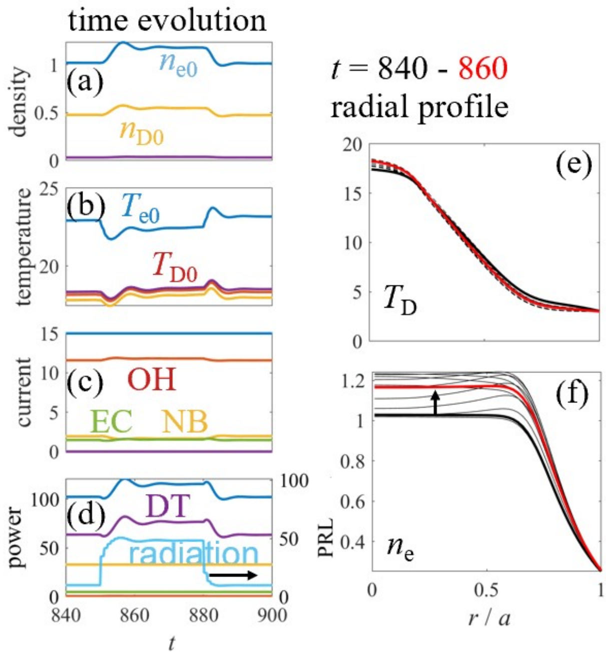

FIG. 3. Plasma response with increasing edge impurity Ne using the set of ITER tokamak parameters. The time evolutions of (a) density, (b) temperature, (c) plasma current, (d) radiation power, and the radial profiles of (e) ion temperature and (f) electron density are shown.

Acknowledgements

This work was partially supported by the collaboration program of QST on development research of the fusion DEMO reactor, and of RIAM of Kyushu University.

References

[1] R. Neu, *et al.*, Plasma Phys. Control. Fusion **44**, 811 (2002).
[2] C. Angioni, *et al.*, Nucl. Fusion **54**, 083028 (2014).
[3] http://bpsi.nucleng.kyoto-u.ac.jp/task/
[4] S. Mochinaga, *et al.*, Nuclear Fusion **64**, 066002 (2024).
[5] W. Houlberg, *et al.*, Phys. Plasmas **4**, 3230 (1997).
[6] http://open.adas.ac.uk/
[7] C. Gormezano, *et al.*, Nucl. Fusion **47**, S285 (2007).

Kinetic Modelling for Energetic Particle Transport Induced by Electrostatic and Magnetic Fluctuation in Tokamak Plasma

K. Tahara, D. Iio, Y. Yamamoto, and S. Murakami

Department of Nuclear Engineering, Kyoto University

1 Introduction

Plasma flow shear is widely recognized to play important roles in suppression of turbulent transport and in L-H transition. Spontaneous toroidal flows during ECH, without direct momentum input, are experimentally observed in tokamak and heliotron/stellarator plasmas [1–5], suggesting that ECH may be able to drive and control toroidal flows. A lot of theoretical and experimental studies have been conducted in order to understand the ECH-related flow generation mechanism [5–7]; however, it remains to be elucidated.

Our previous works focusing on SEs' behavior in LHD and HSX [5, 7] have revealed that the non-axisymmetric component of the magnetic field can enhance the radial diffusion of SEs generating an uncanceled toroidal torque. We have obtained a reasonable agreement with some cases of the experimental observations, indicating SEs' behavior could play an important role in the ECH-related flow generation.

In this study, we focus on electrostatic and magnetic fluctuations with a finite toroidal mode number due to micro-instability as an axisymmetry-breaking factor. The orbit-following simulations, investigating the effect of the fluctuations on SEs' behavior and the associated toroidal torque, have performed. We also have derived a kinetic model of fluctuation-induced SE transport for the electrostatic case.

2 Numerical model

We have applied GNET code [9] solving a linearized drift kinetic equation (DKE) in 5-D phase space of the deviation of the electron distribution function from that at equilibrium δf,

$$\left(\frac{\partial}{\partial t}+\dot{\mathbf{X}}\cdot\nabla+\dot{v}_\parallel\frac{\partial}{\partial v_\parallel}\right)\delta f=S^{\mathrm{QL}}+C\left(\delta f\right)-L^{\mathrm{loss}}, \tag{1}$$

where $\dot{\mathbf{X}}$ and $v_\parallel$ are the guiding center velocity and its parallel component to the equilibrium magnetic field, S^{QL}, C and L^{loss} are the quasi-linear heating source, the linear Coulomb collision operator, and the particle sink respectively. We consider a tokamak plasma in the presence of electrostatic and magnetic fluctuations, $\tilde{\phi}$ and $\tilde{\mathbf{A}}$. We assume the sinusoidal fluctuations consisting of 400 modes, (m, n) = (120-140, 110-130). Each mode takes a Gaussian distribution in the radial direction with its peak at the rational surface, $q = m/n$. The fluctuations temporally oscillate with the ion-drift frequency, one of the typical ion-scale micro-instabilities.

3 Results

Fig.1-(a) compares the radial profile of the SE flux, Γ_{e}, with/without fluctuations. Here $\Gamma_{\mathrm{e}}^{(+)}$ is the contribution of the positive-weighted component of SEs, $\delta f > 0$ to the radial flux, and $\Gamma_{\mathrm{e}}^{(-)}$ is of the negative one, $\delta f < 0$. It shows fluctuations enhance the radial transport of SEs. It is also found that the positive-weighted component of SEs less contributes to the radial flux in the presence of the electrostatic fluctuation. Since the positive-weighted SEs tend to have a higher energy than the negative ones due to the initial distribution given by the quasi-linear heating term, this indicates the SEs with lower energy generate a larger radial flux.

Fig.1-(b) shows the energy-dependency of the fluctuation-induced radial transport. The volume-integrated radial flux increases with the averaged initial energy in the energy region below ∼15 keV, where it peaks, and then decreases. It is also found that the SEs with positive weight make a less contribution to the radial transport, which is consistent to the result in Fig.1-(a). Fig.2-(a), (b), and (c) compare the energy-dependency of passing and trapped particles.

Fig.2-(a) and (b) indicate the fluctuation-induced transport of passing particles and trapped ones show the different dependency on particle energy. We have performed another simulation with the temporally stationary fluctuations, $\omega = 0$. Fig.2-(d) compared the results and those in the case of the drift frequency, $\omega = \omega_{*\mathrm{i}}$. It is also found the frequency model of the fluctuations has a significant effect on the SE transport.

In order to explain and understand the simulation results, we have derived a kinetic model for the fluctuation-induced SE transport based on the drift kinetic theory. In our model, the fluctuation-induced radial flux of passing particles is given as

$$\left\langle\hat{\mathbf{\Gamma}}_{\mathbf{k}_\perp}\cdot\nabla\chi\right\rangle_{\mathrm{ens}}^{(\mathrm{pass})}\sim-\frac{1}{2}\frac{{k_\alpha}^2\left|\hat{\phi}_{\mathbf{k}_\perp}\right|^2}{\left|\omega^T_{\mathrm{d},\mathbf{k}_\perp}\right|}\frac{\rho_{T_\mathrm{i}}}{L_{\mathrm{env}}}\times\left(-A_0+\frac{B_0}{x}+\frac{C_0}{x^2}\right)\frac{\partial}{\partial\chi}\left\langle\delta n^{(0)}\right\rangle, \tag{2}$$

where χ is a poloidal flux function, α is a field line label, $k_\alpha = -n$ is the α-component of the perpendicular wave number vector $\mathbf{k}_\perp$, $\hat{\phi}_{\mathbf{k}_\perp}$ is a Fourier component of the electrostatic fluctuation, E_0 is averaged particle energy, and $x := E_0/x \gtrsim 1$, $\omega^{\mathrm{T}}_{\mathrm{d},\mathbf{k}_\perp} = -n \langle \mathrm{d}\alpha/\mathrm{d}t \rangle$ is the Doppler shift due to magnetic drift of thermal electrons. ρ_{T_i} is the ion Larmor radius evaluated by the thermal velocity, L_{env} is the characteristic length of the envelope of the fluctuations satisfying $\rho_{T_\mathrm{i}} \ll L_{\mathrm{env}}$. The bracket $\langle F \rangle$ denotes the orbital average of a function F. The coefficients A_0, B_0, and C_0 satisfy $B_0 \sim C_0 \sim \mathcal{O}(1)$, $|A_0/B_0| \ll 1$, and $C_0 \propto \omega$. Similarly we obtain the trapped particle flux,

$$\left\langle \hat{\mathbf{\Gamma}}_{\mathbf{k}_\perp} \cdot \nabla\chi \right\rangle^{(\mathrm{trap})}_{\mathrm{ens}} \sim -\frac{1}{4} \frac{{k_\alpha}^2 \left|\hat{\phi}_{\mathbf{k}_\perp}\right|^2}{{\omega_\mathrm{b}}^2} |\omega^T_{\mathrm{d},\mathbf{k}_\perp}| \frac{\rho_{T_\mathrm{i}}}{L_{\mathrm{env}}} \times \left(A_1 x + B_1 x^{1/2}\right) \frac{\partial}{\partial \chi} \left\langle \delta n^{(0)} \right\rangle, \qquad (3)$$

where ω_b is the bounce frequency of thermal electrons, A_1 and B_1 satisfy $|B_1/A_1| \ll 1$ and $B_1 \propto -\omega$.

Eq.(2) is a decreasing function of particle energy, which can explain the tendency in the simulation results and Eq.(3), on the other hand, increases with energy. This model is consistent with the simulation results in Fig.2-(a) and (b).

Taking the ratio of Eqs.(2) and (3) in the lowest order terms yields

$$\left| \frac{\left\langle \hat{\mathbf{\Gamma}}_{\mathbf{k}_\perp} \cdot \nabla\chi \right\rangle^{(\mathrm{trap})}_{\mathrm{ens}}}{\left\langle \hat{\mathbf{\Gamma}}_{\mathbf{k}_\perp} \cdot \nabla\chi \right\rangle^{(\mathrm{pass})}_{\mathrm{ens}}} \right| \sim \left| \frac{\delta n^{(\mathrm{trap})}}{\delta n^{(\mathrm{pass})}} \right| {\varepsilon_\mathrm{M}}^2 {\varepsilon_\mathrm{E}}^{-1} \sim \mathcal{O}(\delta), \qquad (4)$$

which indicates passing particles dominantly affect the radial flux in the presence of electrostatic potential fluctuations. Eq.(4) well captures the tendency of the result in Fig.2-(c) comparing the contributions of passing and trapped particles, $|\Gamma^{(\mathrm{trap})}/\Gamma^{(\mathrm{pass})}| \sim \mathcal{O}(10^{-1})$ in $E = 10\,\mathrm{keV} - 30\,\mathrm{keV}$.

Eqs.(2) and (3) also include the effect of the frequency of the fluctuations. However, further analyses are needed to verify whether our model can explain the effect of the frequency as in Fig.2-(d), which is our future work.

4 Conclusion

We numerically investigate the effect of electrostatic and magnetic fluctuations on the radial transport of ECH supra-thermal electrons. It is found that electrostatic and magnetic fluctuations can enhance SE transport generating uncancelled toroidal torque. We have derived a transport model including kinetic effects indicating ion scale micro-instabilities have a resonant effect on the radial diffusion of SEs. This model can explain the different energy dependence between passing and trapped particles, and the significant effect of the fluctuation frequency in the electrostatic case.

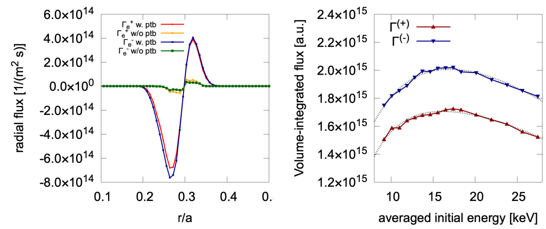

(a) radial particle flux (b) energy-dependency

Fig. 1: The fluctuation-induced SE radial transport. (a): radial profile of the particle flux. (b): averaged initial energy-dependency of the volume-integrated flux.

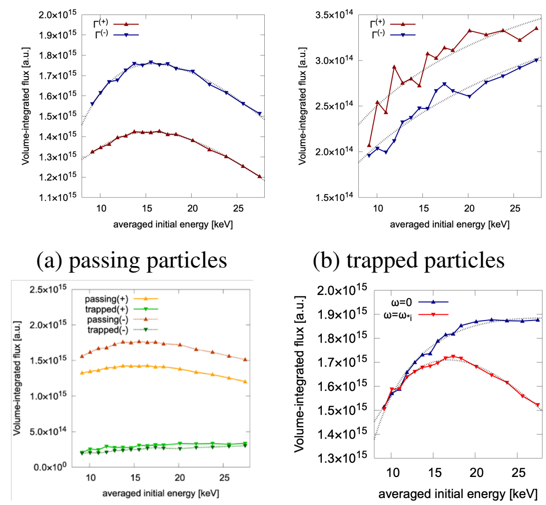

(a) passing particles (b) trapped particles

(c) passing vs. trapped (d) static vs. time-varying

Fig. 2: Energy-dependency of radial transport. (a): passing particles. (b): trapped particles. (c): comparison of passing and trapped particles. (d): comparison of the static case $\omega = 0$ and the time-varying case $\omega = \omega_{*\mathrm{i}}$.

References

[1] J. S. deGrassie, *et al.*, Phys. Plasmas **11**, 4323 (2004)

[2] L. Porte, *et al.*, Nucl. Fusion **47**, 952 (2007)

[3] M. Yoshida, *et al.*, Phys. Rev. Lett. **103**, 065003 (2009)

[4] R. S. Wilcox, *et al.*, Nucl. Fusion **56**, 036002 (2016)

[5] Y. Yamamoto, *et al.*, Phys. Plasmas **28**, 102501 (2021)

[6] J. D. Callen, *et al.*, Nucl. Fusion **49**, 085021 (2009)

[7] T. Yamamoto, *et al.*, Nucl. Fusion **62**, 064004 (2022)

[8] M. N. Rosenbluth, *et al.*, Nucl. Fusion **36**, 55 (1996)

[9] S. Murakami, *et al.*, Nucl. Fusion **40**, 693 (2000)

EC multiple resonance heating and Supra-thermal electron behaviours in QUEST

S. Murakami[1], Y. Ishida[1], H. Idei[2], T. Onchi[2], M. Hasegawa[2] and QUEST Team[2]

[1]Department of Nuclear Engineering, Kyoto University, Kyoto, Japan
email address: murakami@nucleng.kyoto-u.ac.jp
[2]Research Institute for Applied Mechanics, Kyushu University, Kasuga, Japan

Electron Cyclotron Current Drive (ECCD) is a leading candidate for the current drive method of a steady-state tokamak reactor. The major drawback of ECCD is that it is less efficient than the neutral beam current drive. Therefore, various studies have been conducted to increase the current drive efficiency of ECCD.

QUEST, a spherical tokamak at Kyushu University, has been instrumental in studying the generation of energetic electrons through electron cyclotron resonance heating (ECH). Designed with a major radius of 0.64 m and a minor radius of 0.4 m, QUEST operates at a magnetic field strength of 0.25 T. The primary purpose of QUEST is to explore advanced plasma confinement techniques and current drive mechanisms, particularly in low aspect ratio configurations. One of its unique features is the ability to perform high-power ECH and oblique injection, enabling detailed studies of supra-thermal electron dynamics and their influence on plasma stability.

Recently, energetic electrons with energies up to 200 keV have been observed in the electron cyclotron heating (ECH) plasma of QUEST[1]. These observations cannot be explained by simple second harmonic resonance heating. Notably, a toroidal current of approximately 80 kA was achieved with oblique ECH injection at a parallel wave number (N//) of 0.7. The acceleration of supra-thermal electrons (SEs) is theorized to be facilitated by third harmonic resonance, with additional acceleration from the fourth harmonic. This multi-harmonic heating process is believed to significantly contribute to the population of energetic electrons, although theoretical validation using kinetic theory is still not done.

This study investigates the generation of supra-thermal electrons through higher harmonic resonance heating and their impact on plasma behavior, particularly the toroidal current. We employ the GNET code[2-4], which solves a linearized drift kinetic equation for the deviation of the electron distribution function from the Maxwellian distribution ($\delta f = f - f_{Maxwell}$) by simulating ECH in a 5-dimensional phase space using the Monte Carlo method. The quasi-linear ECH driving term serves as a source term in velocity space, and we also include additional non-linear heating terms for the third and fourth harmonic resonances in this analysis.

In our GNET simulation, we assume plasma parameters of Te ~ 2 keV, Ti ~ 2 keV, and ne ~ 1.0 $\times 10^{18}$m^{-3}. We obtain the steady-state distribution (δf) with contributions from 2nd, 2nd + 3rd, and 2nd + 3rd + 4th harmonic resonance accelerations. Our results indicate a substantial formation of an energetic tail due to heating from the third and fourth harmonics, with the relative electron populations in the 100-200 keV and over 200 keV ranges showing good agreement. As N// increases, the formation of the energetic tail is enhanced, and a significant tail is observed at N// = 0.8. We find that the induced current increases monotonically with increasing N//, and the obtained electron current closely matches the experimental value, reaching up to 70 kA.

1. T. Onchi et al., Physics of Plasmas **28** (2021) 022505.
2. S. Murakami, et al., Nuclear Fusion **40** (2000) 693.
3. S. Murakami, et al., Nuclear Fusion **46** (2006) S425.
4. Y. Yamamoto, et al., Nuclear Fusion **62** (2022) 064004.

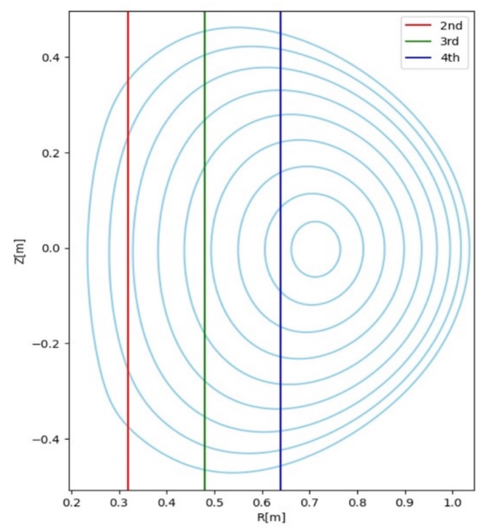

Fig. 1: Resonance locations of ECH in QUEST

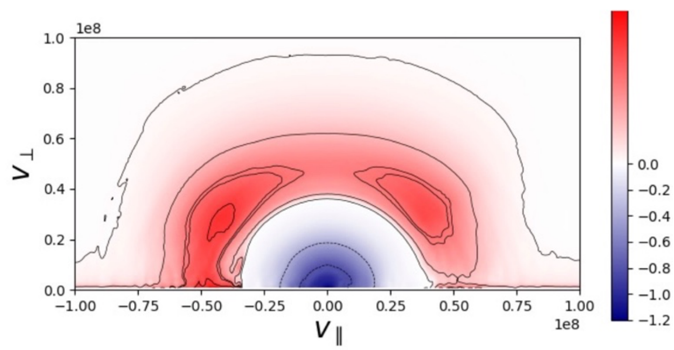

Fig. 2: Velocity space distribution of δf

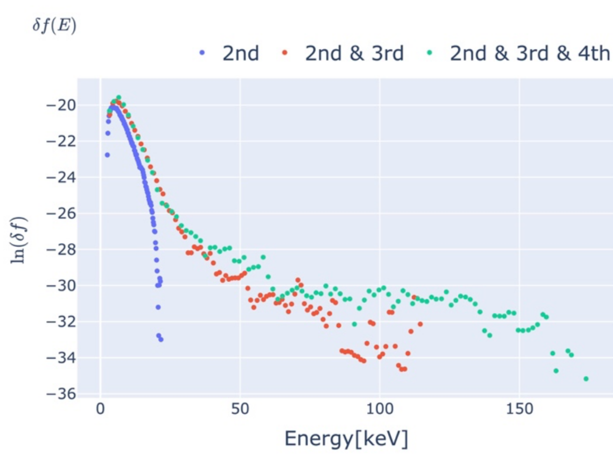

Fig. 3: Energetic electron distribution by ECH

Diagnostic simulation of experimental measurement of density fluctuations in tokamak plasma by phase contrast imaging using a gyrokinetic simulation code

Kosuke KUWAMIYA[1], Naohiro KASUYA[1,2], Kenji TANAKA[1,3]
IGSES, Kyushu Univ.[1], RIAM, Kyushu Univ.[2], NIFS.[3]

1. Research background and objectives

Improving the confinement performance of plasmas is crucial for the realization of nuclear fusion power generation. Turbulent transport plays a significant role in the plasma confinement [1]. Phase Contrast Imaging (PCI) is one of the methods for measuring turbulence in magnetically-confined plasmas. Phase change of an injected laser beam occurs due to density fluctuations, which is measured by PCI [2,3]. As PCI does not depend on specific plasma conditions and allows measurement across the entire plasma region, it has been adopted in various tokamak and helical devices. Numerical simulations have also been conducted for comparison with experiments [2,4].

In this study, we conduct PCI measurement simulations for the nuclear fusion experimental device JT-60SA. We simulate PCI measurements by combining magnetic field equilibrium calculations in the JT-60SA tokamak with fluctuation fields calculated by a gyrokinetic simulation code. By evaluating the line integration effect in the direction of the line of sight, we aim to enhance our understanding of the signals obtained from PCI measurements.

2. Turbulence measurement simulation

We perform simulations of PCI measurements on fluctuation field data in a three-dimensional tokamak magnetic configuration. This section describes an overview of that process.

2.1 Plasma Equilibrium

For the simulation of measurements, the geometry of the device and the plasma shape are used. The plasma shape is calculated using the tokamak equilibrium module EQU of the integrated code TASK [5]. The EQU module is capable of performing equilibrium calculations for free-boundary plasmas, including external coil currents.

2.2 Turbulence field

The turbulence to be measured is obtained from numerical simulations. Here, we use fluctuations calculated by the gyrokinetic code GENE [6]. GENE solves the gyrokinetic equations in a five-dimensional phase space, providing high-accuracy predictions of plasma turbulence as well as heat and particle transport. The three-dimensional distribution of fluctuations in the JT-60SA tokamak was simulated by mapping the density fluctuations calculated by GENE onto the tokamak geometry obtained from TASK/EQU.

2.3 PCI measurement simulation

PCI measurement is used to measure the wavenumber spectrum of density fluctuations [4]. The incident laser is scattered by the density fluctuations, and the interference between this scattered wave and the reference wave produces a two-dimensional pattern related to the wavenumber k of the fluctuation. Since the obtained signal is integrated along the line of sight, it becomes necessary to reconstruct local density fluctuation information from this signal. In this simulation, images of density fluctuations integrated along the measurement line of sight are provided as the measurement results.

3. Results of data analysis

3.1 Equilibrium and Turbulence Calculation

Figure 1 shows the coil current values used to obtain the equilibrium magnetic field configuration with TASK/EQU and an example of density fluctuation data calculated by the GENE code. The plasma parameters are major radius $R = 2.9$m, minor radius $a = 1.2$m, plasma volume $V_p = 140\text{m}^3$, triangularity $\delta = 0.44$, and elongation $\kappa = 1.9$. The poloidal cross-section of the tokamak plasma shows the fluctuation data mapped onto a region at normalized minor radius $\rho = 0.76$ with a width of d$\rho = 0.13$.

Table. 1 coil current

coil name	current (MA turn)
CS1	1.26
CS2	0.40
CS3	4.53
CS4	6.03
EF1	-0.68
EF2	-1.54
EF3	4.64
EF4	5.05
EF5	0.09
EF6	-2.20

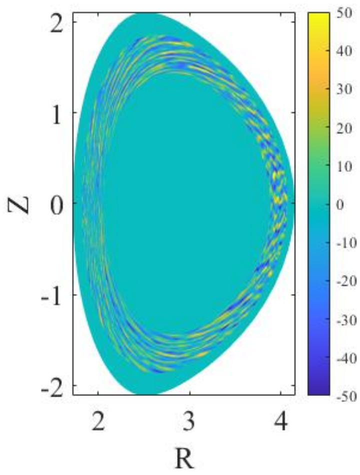

Fig. 1 Density fluctuations calculated by GENE, mapped onto the tokamak equilibrium configuration.

3.2 PCI measurement simulation

In JT-60SA, measurements using Tangential Phase Contrast Imaging (TPCI), where the laser is injected tangentially to the magnetic field direction near the equatorial plane, are planned [2]. Using the TPCI beam path for JT-60SA, as shown in Fig. 2, we calculated the integrated density fluctuation image.

Figure 3(a) presents the integrated signal image obtained through the simulation of PCI measurements based on the fluctuation data shown in Fig. 1. In this simulation, the PCI line of sight in this TPCI simulation observes both the high-field and low-field side of the tokamak. Since the fluctuation data are localized, the integrated signal includes the summation of the localized contributions from $B_2 \sim B_4$ (high-field side) and B_1, B_5 (low-field side) in Fig. 2.

Figure 3(b) shows the two-dimensional wavenumber spectrum of the integrated signal. The coordinates (x, y) represent the directions perpendicular to the beam line, which correspond approximately to the (r, θ) directions on the high-field side and to the (ϕ, θ) directions on the low-field side. Here, r, θ, and ϕ represent the radial, poloidal, and toroidal directions, respectively. Figure 4 shows the 2-D spectrum of the local density fluctuations. From comparison between Figs. 3 and 4, the peak within the red dashed circle in Fig. 3 is found to be the (r, θ) fluctuation components on the high-field side in Fig. 4(c), while the peak at ($k_x\rho_i$, $k_y\rho_i$) = (0, 0.12) corresponds to the (ϕ, θ) fluctuation components on the low-field side in Figs. 4(a) and (e).

In the local signals, asymmetry in k_y is observed, reflecting the tilt of the magnetic field lines at each measurement location as in Figs. 4(b) and (d). These variations in fluctuation components suggest possibility to distinguish local information from the integrated signal by using the magnetic field direction.

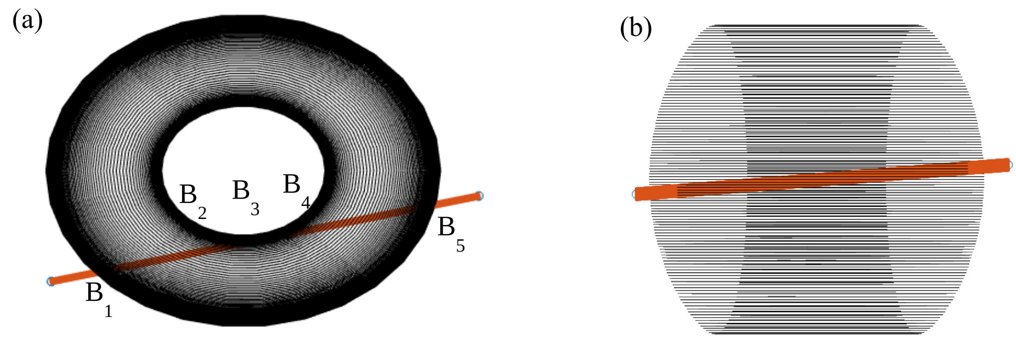

Fig. 2 TPCI measurement line of sight (orange lines). The views from (a) above and (b) the side are shown.

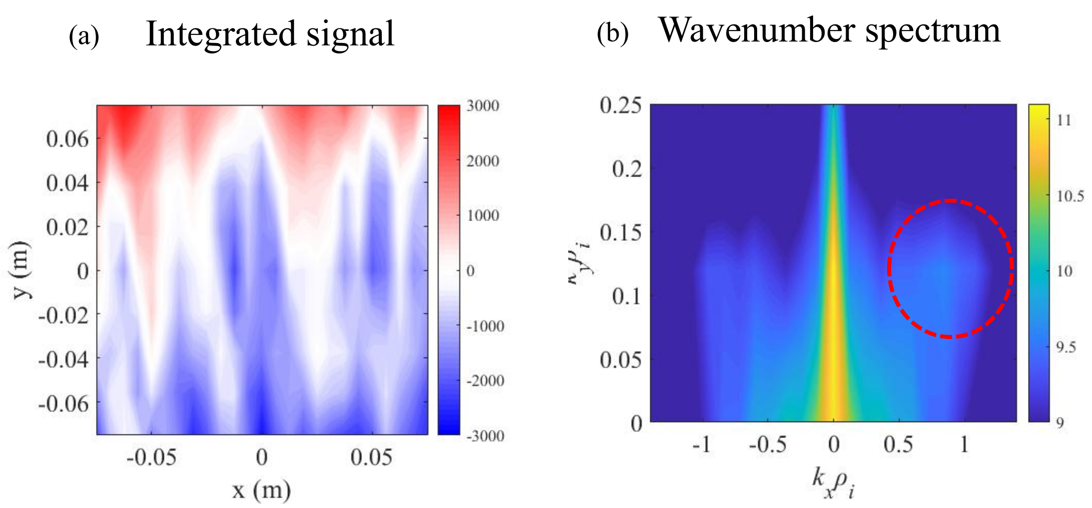

Fig. 3 PCI Signal Simulation. (a) Snapshot of line-integrated density and (b) its wavenumber spectrum are shown.

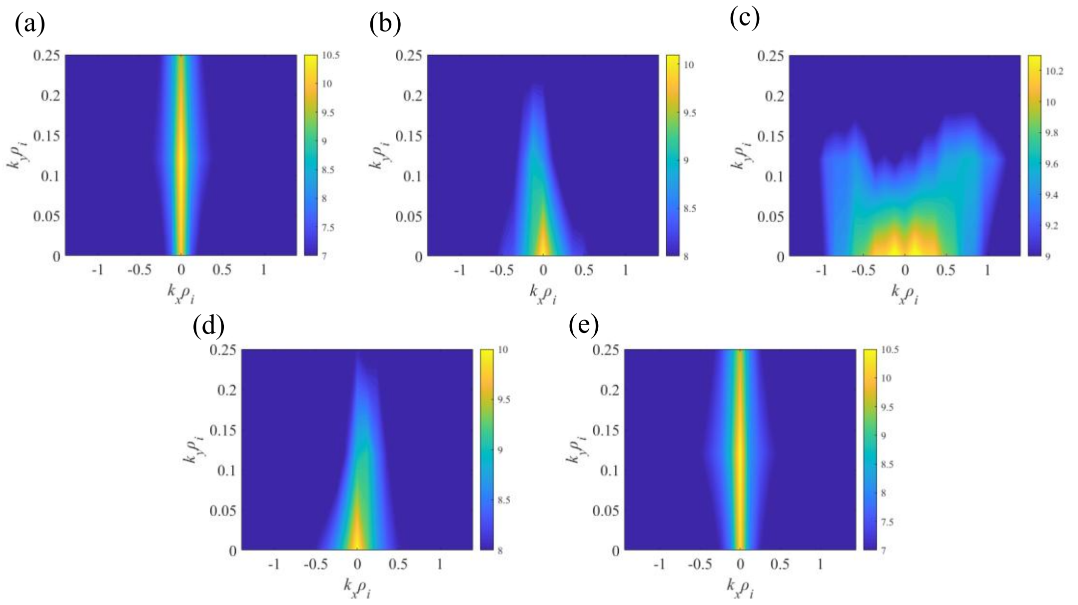

Fig. 4 Wavenumber spectrum of local density fluctuations. (a) to (e) correspond to those at the positions B_1 to B_5 in Fig. 2.

4. Conclusion

In this study, we constructed a PCI measurement simulation routine and performed calculations using the magnetic field configuration of the JT-60SA tokamak plasma. We applied the TPCI diagnostic arrangement for JT-60SA and presented the integrated density fluctuation signal and its two-dimensional wavenumber spectrum. Comparison with the local wavenumber spectrum at each measurement position has given the information how the wavenumber spectrum of the integrated signal is composed of a combination of signals from different positions.

References

[1] P. H. Diamond, *et al.*, Plasma Phys. Control. Fusion **47**, R35 (2005).

[2] S. Coda, *et al.*, Nucl. Fusion **61**, 106022 (2021).

[3] K. Tanaka, *et al.,* Rev. Sci. Instrum. **79**, 10E702 (2008).

[4] N. Kasuya, *et al*., Nucl. Fusion **58**, 106033 (2018).

[5] https://bpsi.nucleng.kyoto-u.ac.jp/task/

[6] F. Jenko, *et al*., Phys. Plasmas **58**, 1904 (2000).

Integrated transport simulation of pellet injection discharge in LHD

Yuto Horioka, Kyoto Univ. Department of Nuclear Engineering

To keep fusion plasma, powerful heating and continuous fuel supply are essential. The primary methods of fuel supply to plasma include the gas puffing method, which injects neutral hydrogen gas from the periphery of the plasma, and the fuel pellet injection method, which directly supplies fuel to the core plasma by injecting solid fuel pellets at high speed. The gas puffing is of course an important fueling method, but in high-temperature and high-density plasmas, this method faces a challenge, as the neutral gas ionizes at the plasma edge, preventing effective fuel supply to the core plasma. On the other hand, the fuel pellet injection method not only enables direct fuel supply to the core plasma but also has been shown to provide additional benefits, such as improving plasma confinement properties. Therefore, it is being actively researched as a promising fuel supply technique.

Since fusion plasma involves various complex physical phenomena, its control requires advanced multivariable predictive control. To address this, We have developed a predictive control system called ASTI, which utilizes real-time integrated transport simulations. This system employs the integrated transport code TASK3D [1] as its predictive model. TASK3D can simulate the overall plasma behavior by coupling modules that describe physical processes within the plasma, including heating and fuel supply. Currently, TASK3D can predict density changes caused by gas puffing; however, it has not yet achieved real-time predictions for fuel pellet injection. Therefore, this study aims to develop a fuel pellet injection module capable of real-time prediction to achieve predictive control of density changes caused by fuel pellet injection.

In this study, the Large Helical Device (LHD) has been selected as the plasma device of interest, as it has extensive experimental data on pellet injection and ongoing implementation of the ASTI system. The LHD, owned by the National Institute for Fusion Science (NIFS), is a helical-type plasma confinement device, as shown in Fig. 1. This device enables the stable generation of high temperature plasma and precise measurement of internal plasma parameters, and it has achieved numerous research milestones in the field of magnetically confined plasma.

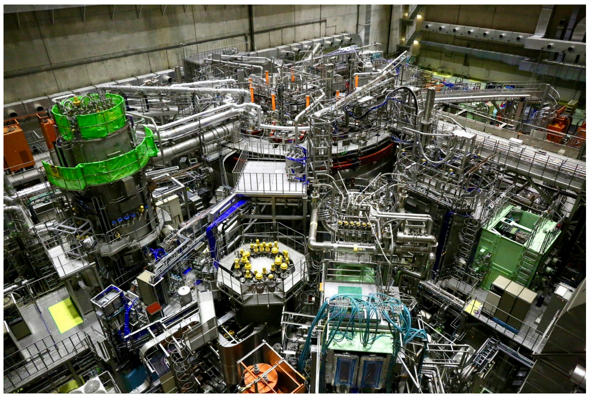

Fig. 1: Photo of the entire LHD

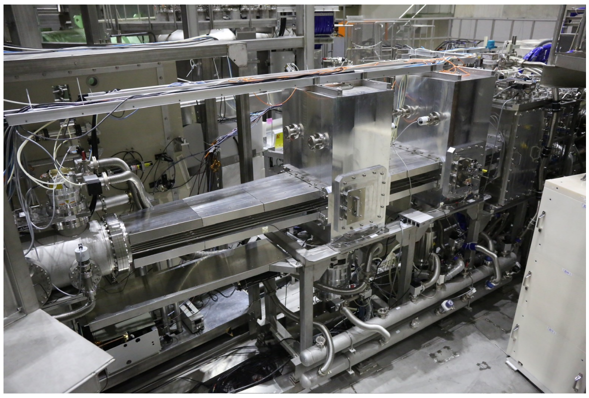

Fig. 2: 20-barrel solid hydrogen pellet injector

At LHD, a 20-barrel solid hydrogen pellet injector system, shown in Fig. 2, is in operation [2]. This system allows for the sequential injection of up to 20 cylindrical fuel pellets with diameters and lengths of 1.4 mm, 3.0 mm, 3.4 mm, and 3.8 mm at speeds of approximately 1200 m/s during a single plasma discharge.

The phenomena occurring during pellet injection can be briefly described as follows. When a pellet enters the plasma, it is exposed to the heat flux from the high-temperature and high-density background plasma, causing the pellet material to ablate. The ablated pellet particles form a neutral gas cloud that surrounds the pellet in a spherical shape, shielding it from the background plasma heat flux. A portion of

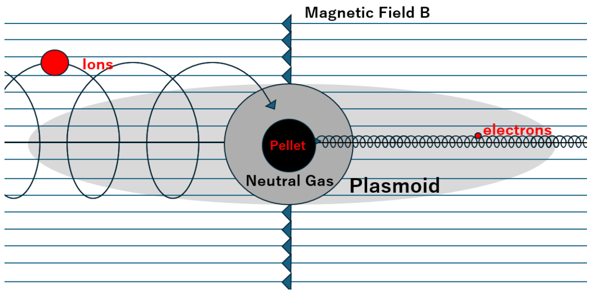

Fig. 3: Image of pellet injection phenomena

this neutral gas becomes ionized, resulting in the formation of a high-density, low-temperature plasmoid compared to the background plasma, which further envelops the neutral gas cloud. These processes are illustrated in the schematic diagram shown in Fig. 3. After a certain period, the plasmoid detaches from the pellet and begins to move independently before eventually homogenizing with the background plasma. In a single pellet injection process, several tens of plasmoids are generated.

The fundamental pellet ablation model primarily used is the Neutral Gas Shielding (NGS) model described earlier. In this study, two different models based on the theories proposed by P.B. Parks et al. [3] and S.L. Milora et al. [4] were implemented to allow for comparison and evaluation. Additionally, since it has been reported that the heat flux from fast ions generated by Neutral Beam Injection (NBI) heating cannot be ignored [5], an implementation of the model proposed by Y. Nakamura et al. [6], which takes fast ion effects into account, was also carried out by coupling it with the NBI module in TASK3D.

For the plasmoid motion model, the equation of motion proposed by P.B. Parks et al. [7] was implemented.

Using the particle and heat sources obtained from these models, an integrated simulation was conducted to analyze particle and heat transport following pellet injection. Figure 4 and 5 shows a portion of the calculation results. In Figure 4, the initial plasma parameters were set based on experimental data from LHD, and the simulation results of pellet injection were compared with the experimental values. Figure 5 presents the result of the integrated transport simulation.

The calculation time of the integrated code is within real-time, enabling real-time prediction of

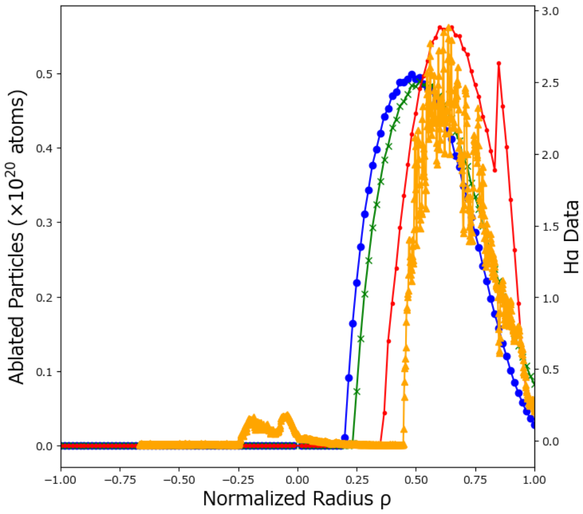

Fig. 4: Comparison of Pellet Penetration Length by Each Models

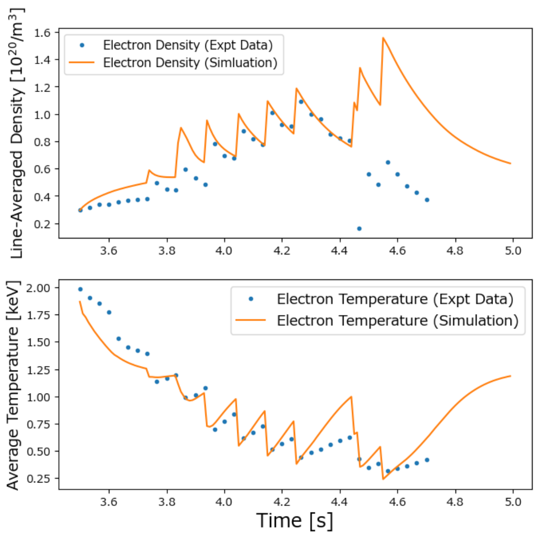

Fig. 5: Result of Integrated Transport Simulation

pellet injection discharges in LHD using the developed module. More detailed results and discussions will be presented at the presentation.

References

[1] S. Murakami *et al.*, Plasma phys. control. fusion **57** (2015)
[2] R. Sakamoto *et al.*, Rev. sci. instrum **84** (2013)
[3] P.B. Parks, and R.J. Turnbull, Phys. Fluids **21** (1978)
[4] S.L. Milora, and C.A. Foster, IEEE Trans. Plasma Sci. **6** (1978)
[5] M. Hoshino *et al.*, Plasma and Fusion Research **1** (2006)
[6] Y. Nakamura, H. Nishihara, and M. Wakatani, Nuclear Fusion **26,** 907 (1986).
[7] P.B. Parks *et al.*, Phys. Plasma **7** (2000)

Investigation of multivariable control gain for fusion power and electron density control by NB injection power and pellet injection using TOTAL
TOTAL を用いた NB 入射とペレット入射による核融合出力・電子密度制御における多変数制御ゲインの検討

*Kazutoshi Kani, Takaaki Fujita, Atsushi Okamoto, Yuichi Kawachi, Seiya Tanaka

Nagoya Univ.

1 Introduction

The design of fusion DEMO reactors is progressing, and among the challenges, the control of core plasma is a significant issue. In the reactor, numerous physical quantities are interrelated. Also, due to the high neutron flux and high heat flux environment, as well as the need to ensure the surface area of the blanket, there are constraints on the installation of diagnostic instruments and actuators. Thus, multivariable control using limited diagnostic instruments and actuators becomes necessary[1]. Additionally, real-time simulation using measured data is required to predict physical quantities that are difficult to measure. This requires the development of integrated codes that simulate the core plasma. The integrated code TOTAL we use is a 1.5D equilibrium and transport code that performs 1D particle and thermal transport analysis and 2D magnetic equilibrium analysis. TOTAL has the advantage of relatively low computational cost, making it suitable for real-time simulation, and it also has the multivariable feedback control function. In this study, we examined multivariable PID control gains, aiming to construct appropriate multivariable control logic for DEMO reactor plasmas using the multivariable feedback control function of TOTAL.

2 Multi-variable control using TOTAL

TOTAL has multivariable feedback control function. It allows for the high degree of freedom setting of controlled and manipulated variables and performs control simulations. The control employs PID control, as represented by equations (1), (2), and (3).

$$X_j(t) = X_j^{pre}(t) + X_j^{base}(t) + \Sigma_k C_j^k(t) \tag{1}$$

$$C_j^k(t) = G_{p,j}^k \left(e_k(t) + \frac{1}{\tau_{i,j}^k} \int e_k(\tau) d\tau + \tau_{d,j}^k \frac{de_k(t)}{dt} \right) \tag{2}$$

$$e_k(t) = Y_k^{target} - Y_k(t) \tag{3}$$

Here, X_j is the j-th manipulated variable, X_j^{pre} is the pre-programmed value, X_j^{base} is the base (steady-state) value, C_j^k is the correction value of the j-th manipulated variable determined by the k-th controlled variable, $G_{p,j}^k$ is the proportional control gain for controlling the k-th controlled variable with the j-th manipulated variable, $\tau_{i,j}^k$ is the integral time constant, $\tau_{d,j}^k$ is the derivative time constant, $e_k(t)$ is the deviation of the k-th controlled variable, Y_k^{target} is the target value of the k-th controlled variable, and Y_k is the k-th controlled variable. Conventionally, the constants $G_{p,j}^k$, $\tau_{i,j}^k$, and $\tau_{d,j}^k$ required for these calculations have been determined by rules of thumb. In this study, we attempted to determine the proportional control gain $G_{p,j}^k$ based on step response as a generalizable determination method. The control objectives considered were multivariable control of electron density and fusion output using neutral beam (NB) injection power and pellet fueling rate. For the computational conditions, the plasma parameters of JA DEMO were used as references[2]. The time evolution of the main parameters considered in this study is shown in Figure 1.

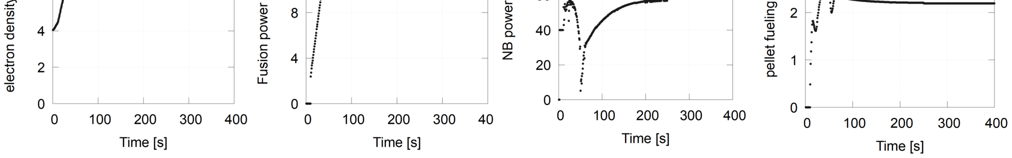

Fig.1: Time evolution of main plasma parameters. (From left: electron density, fusion output, NB injection power, and pellet injection rate.)

The electron density reaches its target value $\bar{n_e}^{tgt} = 8.32 \times 10^{19}$ [m^{-3}] at approximately $t \sim 40$ s, the fusion power reaches its target value $P_{fus}^{tgt} = 1462$ [MW] at $t \sim 40$ s, the NB injection power stabilizes at its equilibrium value $P_{NB}^{eq} \sim 58.2$ [MW] at $t \sim 200$ s, and the pellet fueling rate stabilizes at its equilibrium value $f_{pellet}^{eq} \sim 2.195 \times 10^{19}$ [s^{-1}] at $t \sim 250$ s.

3 Examination of multi-variable control gains

As described in Section 2, we attempted to determine the multivariable PID proportional control gains for electron density control and fusion power control using step responses caused by NB injection power and pellet fueling rate. Here, the step response is defined as the deviation of the controlled variables in response to step changes in the manipulated variables. The specific determination procedure is as follows:

i. Turn off feedback control at the time when each parameter has stabilized ($t = 250s$).

ii. At $t = 260s$, change each manipulated variable by $\pm 10\%$ and calculate the corresponding response as the response matrix $\boldsymbol{A}$.

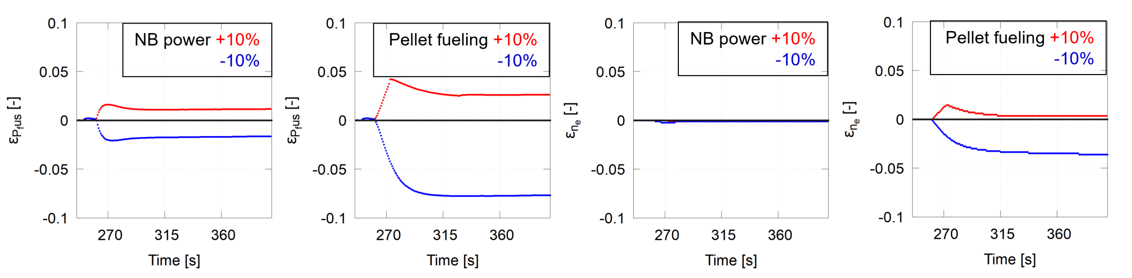

Fig.2: Responses of electron density and fusion power to $\pm 10\%$ step changes in NB injection power and pellet fueling rate.

At this time, the deviations of the controlled variables (vertical axis in the figure above), ε, are normalized with respect to their target values as $\varepsilon_a = (a - a^{tgt})/a^{tgt}$. Additionally, in the response matrix $\boldsymbol{A}$, the combinations of manipulated variables and controlled variables—(NB injection power, fusion power) and (pellet fueling rate, electron density)—are set as diagonal elements (main control relationships). The slope of the line connecting two points of controlled variable deviations ($\varepsilon_{\bar{n_e}}, \varepsilon_{P_{fus}}$) corresponding to manipulated variable changes ($\Delta P_{NB}/P_{NB}^{eq}, \Delta f_{pellet}/f_{pellet}^{eq}$) of $\pm 10\%$ is used as the elements of the matrix. The response matrix $\boldsymbol{A}$ is calculated as follows:

$$\begin{pmatrix} \varepsilon_{P_{fus}} \\ \varepsilon_{\bar{n_e}} \end{pmatrix} = \boldsymbol{A} \begin{pmatrix} \Delta P_{NB}/P_{NB}^{eq} \\ \Delta f_{pellet}/f_{pellet}^{eq} \end{pmatrix} \tag{4}$$

$$\boldsymbol{A} = \begin{pmatrix} a_{11} & a_{12} \\ a_{21} & a_{22} \end{pmatrix} = \begin{pmatrix} 0.1406 & 0.5434 \\ 0.0000 & 0.2103 \end{pmatrix} \tag{5}$$

iii. Calculate the inverse matrix $\boldsymbol{A}^{-1}$. Additionally, by transforming Equation 4, the following results are obtained:

$$\boldsymbol{A^{-1}} = \begin{pmatrix} a_{11}^{*} & a_{12}^{*} \\ a_{21}^{*} & a_{22}^{*} \end{pmatrix} = \begin{pmatrix} 7.116 & -18.38 \\ 0.0000 & 4.755 \end{pmatrix} \tag{6}$$

$$\begin{pmatrix} \Delta P_{NB} \\ \Delta f_{pellet} \end{pmatrix} = \begin{pmatrix} P_{NB}^{eq} \frac{a_{11}^{*}}{P_{fus}^{tgt}} (P_{fus}^{tgt} - P_{fus}) + P_{NB}^{eq} \frac{a_{12}^{*}}{\bar{n_e}^{tgt}} (\bar{n_e}^{tgt} - \bar{n_e}) \\ f_{pellet}^{eq} \frac{a_{21}^{*}}{P_{fus}^{tgt}} (P_{fus}^{tgt} - P_{fus}) + f_{pellet}^{eq} \frac{a_{22}^{*}}{\bar{n_e}^{tgt}} (\bar{n_e}^{tgt} - \bar{n_e}) \end{pmatrix} \tag{7}$$

iv. Calculate the multivariable proportional control gains. When performing actual multivariable control, focusing on proportional control, the control (calculation) is performed as follows:

$$\begin{aligned} \begin{pmatrix} \Delta P_{NB} \\ \Delta f_{pellet} \end{pmatrix} &= \boldsymbol{G_p} \begin{pmatrix} e_{P_{fus}} \\ e_{f_{pellet}} \end{pmatrix} \\ &= \begin{pmatrix} G_{11}(P_{fus}^{tgt} - P_{fus}) + G_{12}(\bar{n_e}^{tgt} - \bar{n_e}) \\ G_{21}(P_{fus}^{tgt} - P_{fus}) + G_{22}(\bar{n_e}^{tgt} - \bar{n_e}) \end{pmatrix} \end{aligned} \tag{8}$$

By comparing Equations (7) and (8) (highlighted parts in red), the multivariable proportional control gain matrix was determined as follows.

$$\boldsymbol{G_p} = \begin{pmatrix} 0.2833\ [-] & -1.286\times10^{-17}\ [\mathrm{MW}\cdot\mathrm{m}^3] \\ 0.0000\ [\mathrm{m}^{-3}\cdot\mathrm{MW}] & 1.254\times10^{2}\ [-] \end{pmatrix} \tag{9}$$

4 Control test

To evaluate the validity of the multivariable proportional control gains calculated in Section 3, particularly the off-diagonal elements that provide corrections to NB injection power from deviation of electron density, a control test was conducted. The content of the control test are that the target value of the electron density is varied while maintaining the target value of the fusion output constant.

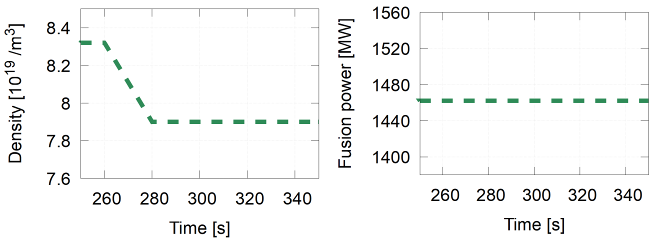

Fig.3: Target values for electron density (left) and fusion output (right) during the control test.

Regarding the above test content, two cases were compared: one with the off-diagonal elements of $\boldsymbol{G_p}$, and the other without (i.e., using a simple combination of two single input single output controls). The results are shown in the following figure.

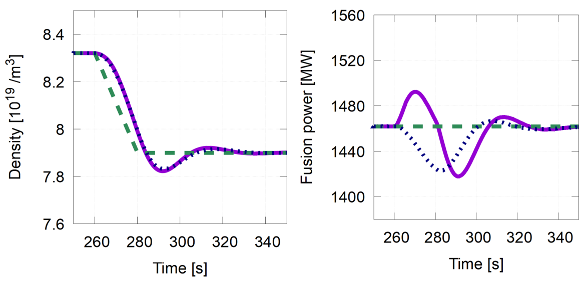

Fig.4: Results of the control test. The green dashed line represents the target value, the purple solid line represents the case where the off-diagonal elements of the gain matrix were considered, and the navy dotted line represents the case where the off-diagonal elements of the gain matrix were ignored.

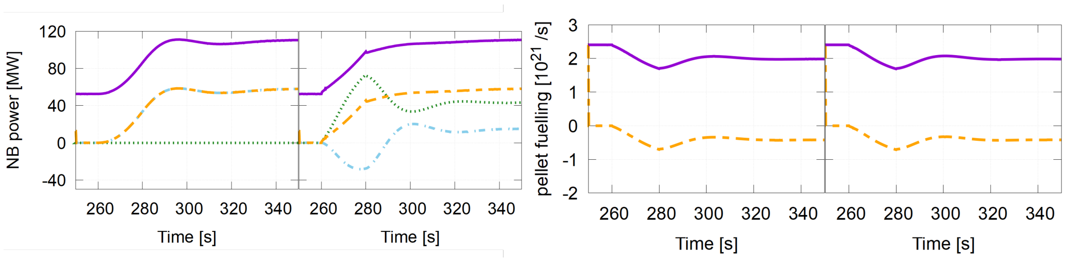

Fig.5: Time evolution of NB injection power and pellet fueling rate during the control test. The left side of each figure shows the case without the off-diagonal term of the gain, and the right side shows the case with it. In NB injection power,purple solid line represents total NB injection power, blue dash-dotted line represents correction by diagonal term G_{11}, green dotted line represents correction by non-diagonal term G_{12}, and orange long and short dash line represents total correction. In pellet injection rate, purple solid line represents total pellet fueling rate and orange long and short dash line represents total correction.

In the results of electron density control, no significant differences were observed between the cases where the off-diagonal elements of $\boldsymbol{G_p}$ were considered and where they were not. However, in fusion output control, significant differences arose between the two cases. The time variations of each manipulated variable for both cases are shown in Fig.5.

In pellet fueling rate, no obvious differences between the presence and absence of the off-diagonal elements. However, in NB injection power, significant differences were observed. The effect of off-diagonal term, which gives correction (increase) to NB injection power from the deviation of electron density (decrease), was significantly different. As a result of the off-diagonal term's effect, the NB injection power increased, causing the fusion output to exceed the target value. To bring it back to the target value, a negative correction was applied to the NB injection power by the diagonal term.

To confirm the generality of the control test above, another control test was carried out with a different speed of reducing the electron density. The target value of the electron density and fusion output are shown in Fig.6.

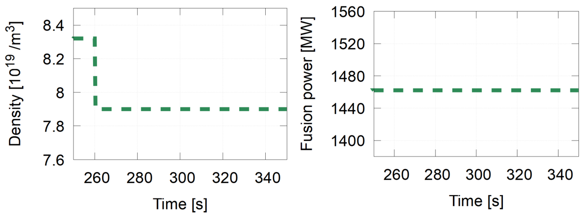

Fig.6: Target values for electron density (left) and fusion output (right) during the second control test.

And the results are shown in the following figure.

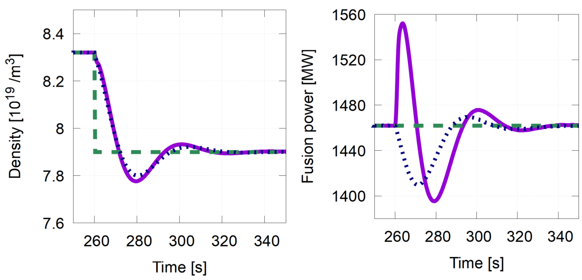

Fig.7: Results of the control test. The colours of the lines represent the same as in Fig.4.

The change in the target value of the electron density was steeper than in the first control test, so the change in fusion output was correspondingly larger. Overall, however, the results were the same as in the previous control test. The time evolution in manipulated variables shows that, same as in the previous test, the effect of the off-diagonal term is larger in NB injection power, while the effect of the off-diagonal term is absent in the pellet fueling rate.

Based on these results, a new control test was conducted after revising the values of $\boldsymbol{G_p}$. The following revisions were made:

- Halve the off-diagonal elements (G_{12}) of the gain matrix
- Double the diagonal elements (G_{22}) of the gain matrix

The results are shown in the following figure.

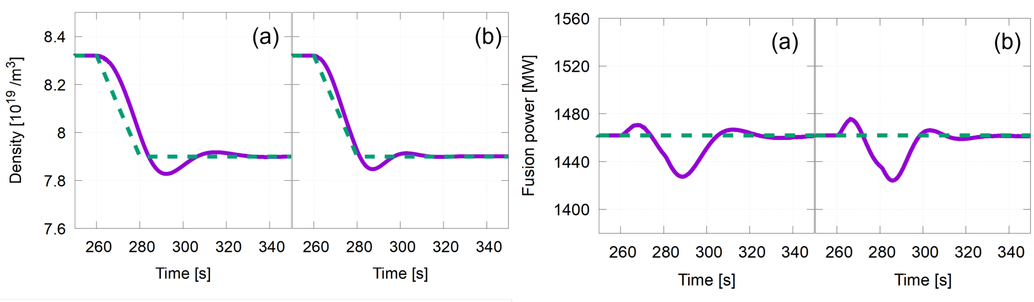

Fig.8: Results of the control test conducted after revising the gain values. Green dashed line represents the target value, purple solid line represents the results of the control test.

In test result (a), oscillations in fusion output were reduced. In test result (b), in addition to reduced oscillations in fusion output, it was confirmed that the electron density and fusion power reached the target value more quickly. From these results, it is suggested that the off-diagonal elements G_{12} of the gain matrix were overestimated, and the diagonal elements G_{22} were underestimated.

5 Summary

In this study, we assumed multivariable PID control of electron density and fusion output in DEMO reactor plasma using NB injection power and pellet fueling rate. We attempted to determine the proportional control gains through a general method using step responses, conducted control tests using the calculated control gains, and evaluated their values. As a result, it was suggested that the diagonal element G_{22}, which adjusts the pellet fueling rate based on deviation of electron density, was underestimated, while the off-diagonal element G_{12}, which adjusts the NB injection power based on changes in electron density, was overestimated. Therefore, the results indicated that there is room for improvement in the method of determining control gains.

As future prospects, we envision improving the determination method for proportional control gains, and search a general determination method for derivative and integral time constants, for which provisional values were used in this study, and calculating multivariable control gains for new combinations of manipulated variables and controlled variables.

Acknowledgment

This work was supported by the Research and Development Collaboration on DEMO Reactors of QST.

References

[1] Working group report on Diagnostics & Control for fusion DEMO, Joint Special Design Team for Fusion DEMO, September 2023.

[2] Y. Sakamoto et al., 25th IAEA Int. Conf. on Fusion Energy(St. Petersburg, Russia, 2014), FIP/3-4Rb.

Progress report on application of SOLOS-ITER to JA-DEMO divertor modeling

G. Kawamura[1], H. Si[1], N. Asakura[2], K. Hoshino[3], Y. Sakamoto[1], M. Yagi[1]
[1]QST Rokkasho Japan, [2]QST Naka Japan, [3]Keio Univ. Japan

1. Introduction

Recently more and more universities, research institutes, and private companies have strong interests on development of fusion DEMO reactors all over the world, however there are still technological gaps toward DEMO reactors under the current situation, where we have to wait for a decade for the first plasma of ITER. One of the essential issues is divertor design and its operation scenarios. The divertor concept with a reference design of a DEMO reactor has to be completed without waiting for ITER experiments, though ITER results should be taken into account in the final divertor design. In such a situation, numerical studies based on plasma physics and experiment data of existing devices are indispensable for divertor design studies, and development of numerical codes is a pressing issue. However, a numerical model and simulation always involve some uncertainties and physically unclear input parameters, and therefore validations by experiments and sensitivity studies of the physical models and adjustable parameters in the codes are needed.

In JA-DEMO divertor research, SONIC code [1,2] has been mainly used to make a reference design of the divertor and to improve it continuously. However, it often happens that different numerical models give different results because physical models, boundary conditions, reaction-rate databases, and even some conventional assumptions are different more or less. One of the standard numerical divertor transport simulation code is SOLPS-ITER [3,4], and it is widely used for many fusion devices. That code has an ability to handle particle drifts such as magnetic drift and E×B drift, which have a significant effect on the inboard-outboard energy flux balance and the detachment onset [5,6]. Such an advanced physical model is thought to be useful to improve reliability of JA-DEMO design beyond the current one and could make further optimization possible in the future.

2. Application of SOLPS-ITER to JA-DEMO

SOLPS-ITER code is an integrated simulation code for transport modeling of tokamak divertor plasma, impurity, and neutral particles. The plasma including impurity ions are solved by Braginskii-type fluid equations for each charge state of each species, and the neutral particles of hydrogen isotopes and impurities are solved by Monte-Carlo particle tracing. The schematic diagram of the integration of these two codes is shown in Fig. 1.

We have introduced SOLPS-ITER on the JFRS-1 supercomputer system in 2024. The equilibrium field, the shape of the vacuum vessel, divertor target, and the dome structure are needed for a SOLPS-ITER calculation. We converted the SONIC format of the equilibrium field file, version 161215v2, to the SOLPS-ITER format, and also obtained the wall geometry data from

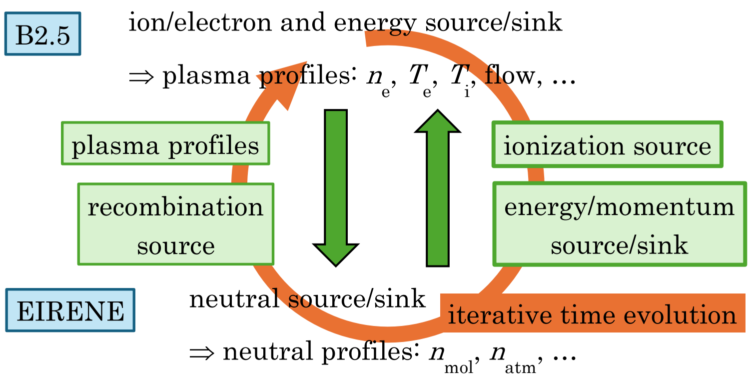

Fig. 1: schematic diagram of SOLPS-ITER code, which consists of the plasm fluid code B2.5 and the neutral kinetic code EIRENE. They iteratively solve time evolution till obtaining a steady state.

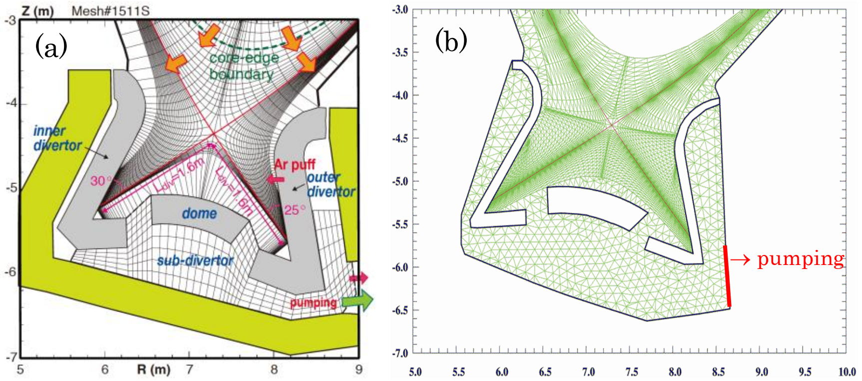

Fig. 2: calculation meshes of (a) SONIC [1] and (b) SOLPS-ITER at the divertor region. We note that the calculation regions of plasma and neutral particles are similar each other but not the same.

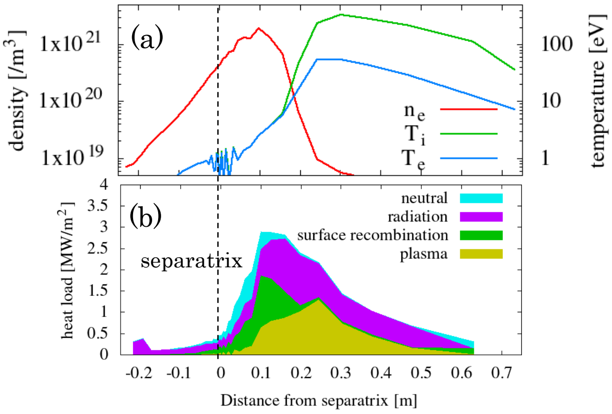

Fig. 3: a preliminary result of outboard divertor target profiles, (a) electron density, electron and ion temperatures and (b) heat load. The separatrix electron density of 2.6×10^{19} /m^3 with deuterium and argon puff. The cross-field transport coefficients are $D = 0.3$ m^2/s and $\chi_e = \chi_i = 1.0$ m^2/s.

the previous SONIC calculations of JA-DEMO. The calculation mesh of SONIC and the newly developed mesh for SOLPS-ITER are shown in Fig. 2.

After trial calculations to find a relevant set of the input parameters such as the pumping coefficient, deuterium and argon puffing rate, heating power, we successfully obtained a numerically converged result qualitatively consistent with a typical operation condition. An example of plasma profiles at the outboard divertor target is shown in Fig. 3. A partial detachment is observed with the heating power of 300 MW with 194 MW radiation power. Helium and argon impurities are included, and the drift effects are disabled on this calculation.

3. Improvement of calculation performance

SOLPS-ITER solves plasma dynamics by time integral to obtain a steady state, and the typical calculation time is longer than a month if we start a calculation from the uniform initial state, and in some cases, especially with drifts, the calculation time can be longer than a year [5]. Most of the calculation of SOLPS-ITER is spent on neutral transport calculation because a large number of particles have to be traced to reduce Monte-Carlo noise.

MPI parallelization is available for neutral tracing, i.e. EIRENE code, however the performance did not scale with the number of MPI processes on JFRS-1 when we introduced the code, and the performance seems to be unreasonably unstable. Fig. 4 shows the calculation time per iteration, i.e., one B2.5 run and one EIRENE run. The two lines in red and green represent the calculation time with the original SOLPS-ITER code on one and two nodes, respectively. We used various numbers of processes per node and found that the performance has a degradation except for certain numbers of MPI processes per node such as 8 and 16. We investigated the source code and found that the degradation was caused by inefficient use of the MPI reduction processing command mpi_reduce() in the post-process gathering the data from each process after the Monte-Carlo calculations. A mpi_reduce() call was used for each 1D sub-array in a 2D array, and

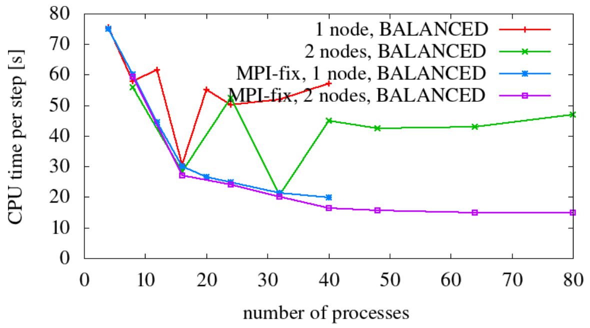

Fig. 4: comparison of the calculation time per iteration with/without the MPI-issue fix.

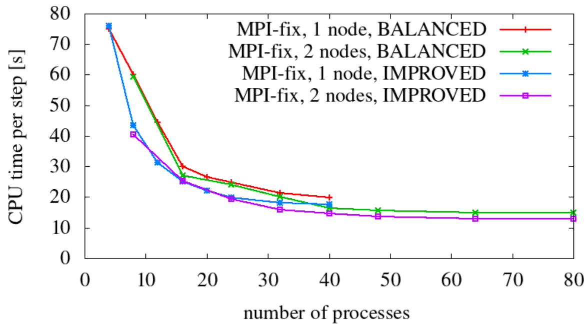

Fig. 5: comparison of the calculation time per iteration the original and improved workload balancing schemes.

approximately 20,000 calls of mpi_reduce() were made per iteration, and that caused a data-communication issue even inside a node. We reproduced the same issue with a simple test program and solved the issue by rewriting mpi_reduce() calls for each 1D sub-array to one mpi_reduce() call for the entire 2D array. We note that the issue depends on MPI libraries. The SOLPS-ITER code with this MPI-fix has a stable performance shown in Fig. 4 with the two lines in blue and purple. This fix enables a flexible selection of number of MPI processes and realizes use of the entire CPU resources in each node on JFRS-1.

The parallelization of neutral particle tracing is realized by dividing the entire workload into almost the same amounts of multiple workloads. EIRENE uses multiple particle sources corresponding to different physical processes such as the surface recombination at the divertor targets, volume recombination inside plasma, gas puffing, and so on. Particle tracing time is much different depending on the sources and also changes according to physical conditions. The original EIRENE code has a workload distribution scheme, so called "BALANCED strategy," and used as a default scheme for SOLPS-ITER. That scheme distributes particles to multiple MPI processes based on the averaged calculation time for a particle in the previous iterations. The time-measurements are performed for each particle source, and the scheme tries to optimize the distribution to minimize the elapsed time of an iteration. Table 1 shows the distribution of the workload by the BALANCED strategy with 12 MPI processes in a test case of JA-DEMO including helium and argon impurities. The distribution table changes according to physical conditions and also iterations for optimization, however we found that the table often contains many small workloads shown in Table 1. Such a complicated allocation causes extra MPI communications inside stratum groups and could lead to inefficient and unstable optimization.

We developed a new workload distribution scheme and implemented as the "IMPROVED strategy" in EIRENE. This scheme allocates small workloads to the rank 0 process at first to minimize the communication from the other processes to the rank 0 process after particle tracing. Also, it tries to allocate the workload of each stratum as a block to multiple processes to avoid small and many divisions. The particle tracing time, the post-processing time, and the communication time are measured separately as before but are used more accurately to estimate the calculation time for each process. The original BALANCED strategy uses the MPI non-blocking communication mpi_ireduce() for the communication within each particle-source group to avoid waiting for the end of other processes and to start particle tracing for another strata, however the processing order of the sources is not relevant and cannot fully make use of the non-blocking communication. We changed the processing order according to the situation of the workload distribution to improve performance. The new workload distribution is shown in Table 2. The estimated calculation time for each process becomes similar, and the longest time becomes shorter than the original distribution that in Table 1. A comparison of the two schemes is shown in Fig. 5. We used a converged result for this test in Fig. 5. The two lines in red and green

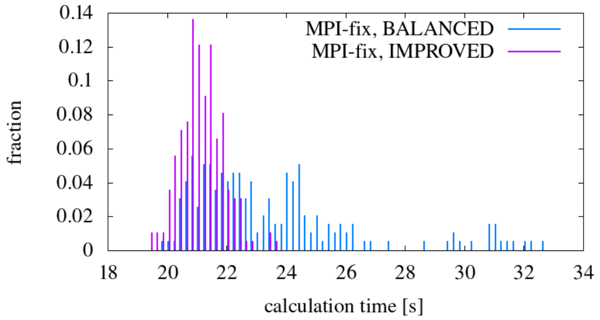

Fig. 6: histogram of the calculation time per iteration for the original and the new parallelization strategies. The simulations use 200 iterations, i.e., time steps.

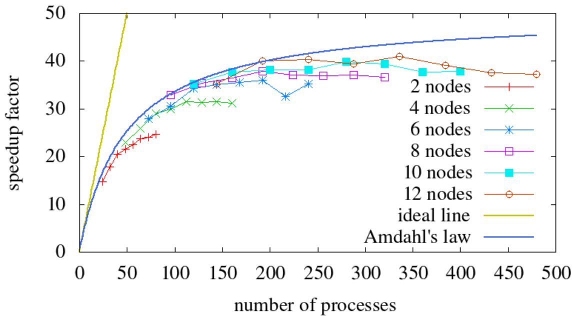

Fig. 7: strong scaling for various combination of process numbers and node numbers. Ideal speed up line and the Amdahl's law with 98% parallel portion were plotted together.

correspond to the original BNALANED strategy and the other two lines in blue and purple correspond to the new IMPROVED strategy. Although the degree of improvement in this case is not so significant, clear improvement is achieved regardless of the number of processes or nodes. Also, we made tests with initial uniform plasma profile and artificially modified conditions to see the improvement before convergence. We confirmed that the degree of improvement is larger than that in Fig. 5.

Fig. 6 is a comparison of histogram of the calculation time per iteration, and the new IMPROVED strategy is more stable in performance. We performed test calculations with various combinations of process numbers and node numbers and plotted the strong scaling in Fig. 7. The numbers of processes per node are 12, 16, 20, 24, 28, 32, 36, and 40. Each node on JFRS-1 has two CPU sockets with Intel Xeon Gold 6148 (2.4GHz/20cores), 768 GiB DDR4-2666 memory, and EDR InifiniBand connection. A small performance degradation occurred when many CPUs per node are used. The reason for that is thought to be degradation of the clock frequency of the CPUs due to thermal limit. The envelope of the data points was well along with the Amdahl's law curve with 98% parallel portion. From the above results, we expect that the new parallelization scheme has better and more stable performance in the entire calculation and shorten a convergence calculation.

4. Summary

We successfully introduced SOLPS-ITER code on JFRS-1 to simulate JA-DEMO divertor plasma. The calculation mesh and wall geometry files are generated from the magnetic equilibrium and the wall shapes used by SONIC. A preliminary calculation was performed after selecting the input parameters such as heating power, pumping coefficient, puffing rate of deuterium and argon, and so on, and then we confirmed that the result is qualitatively consistent with a typical operation condition. In order to accelerate the research, we made two technical developments on the parallelization performance. The first improvement is a fix of degradation on MPI reduction process due to too many calls of mpi_reduce(). This improvement solved unstable performance depending on the number of processes per node. The other improvement is an optimization of workload distribution on processes. This improvement uses a simpler and more robust algorithm to allocate workload for processes and realize better and more stable parallelization performance. These improvements were provided to the SOLPS-ITER group and are available at the git repository at ITER for all the users.

Acknowledgements

The authors would like to thank Dr. Xavier Bonnin at ITER Organization for technical assistance on SOLPS-ITER. This work was carried out using the JFRS-1 supercomputer system at Computational Simulation Centre of International Fusion Energy Research Centre (IFERC-

CSC) in Rokkasho Institute for Fusion Energy of QST (Aomori, Japan).

References

[1] N. Asakura *et al.*, Nucl. Mater. Energy **26** (2021) 100864, 10.1088/1741-4326/ac2ff4.
[2] N. Asakura *et al.*, processes **10** (2022) 872, 10.3390/pr10050872.
[3] X. Bonnin *et al.*, Plasma Fusion Res. **11** (2016), 1403102, 10.1585/pfr.11.1403102.
[4] S. Wiesen *et al.*, J. Nucl. Mater. **463** (2015) 480, 10.1016/j.jnucmat.2014.10.012.
[5] E. Kaveeva *et al.*, Nucl. Fusion **58** (2018) 126018, 10.1088/1741-4326/aae162.
[6] J.S. Park *et al.*, Nucl. Fusion **58** (2018) 126033, 10.1088/1741-4326/aae865.

Table 1: the original workload allocation table for each MPI process. The first and the last columns are the MPI rank and the estimated total calculation time in second for each process, respectively. The columns numbered from 1 to 20 are the allocated calculation time for each particle source, so called strata in EIRENE. The shaded cells are the leader processes of stratum groups, which gather data from other processes in the same group and send it to the process with the rank 0 at the end.

rank	1	2	3	4	5	6	7	8	9	10	11	12	13	14	15	16	17	18	19	20	total
0	15.13	0.57		2.58														8.04			26.3
1		16.37		1.68	8.22																26.3
2	11.95	1.19	3.18	0.87																	17.2
3		1.25		17.23																	18.5
4		1.25		1.86	15.13																18.2
5	11.72	1.20				3.41															16.3
6		4.41		0.88	10.46		11.97														27.7
7	11.16	1.18		1.94				3.97													18.2
8		3.36		2.07					0.20				0.24			1.09			11.43		18.4
9	2.43	3.75								10.09											16.3
10	11.25	1.12									3.15									0.73	16.2
11		1.20		2.00								0.23		0.19	0.03		0.05	14.62			18.3

Table 2: the improved workload allocation table for each MPI process. We note that the estimated time in the last column does not include MPI communication time, and the workload is distributed to have similar calculation time including such a communication time.

rank	1	2	3	4	5	6	7	8	9	10	11	12	13	14	15	16	17	18	19	20	total
0			3.11			3.12		4.44	0.18	0.55	2.66	0.17	0.24	0.14	0.02	1.07	0.04			0.74	16.5
1							1.08			9.07									11.45		21.6
2							11.50											10.10			21.6
3				9.23														12.36			21.6
4				21.59																	21.6
5				2.42	19.56																22.0
6					21.61																21.6
7		21.87			0.12																22.0
8	0.09	21.52																			21.6
9	21.55																				21.5
10	21.99																				22.0
11	21.98																				22.0

First SOLPS-ITER Simulation for Power Exhaust in JA-DEMO Divertor

H. Si[1], G. Kawamura[1], N. Asakura[2], K. Hoshino[3], H. Seto[1], Y. Sakamoto[1], M. Yagi[1]

[1]QST Rokkasho, [2]QST Naka, [3]Keio Univ.

In parallel with the progress of ITER construction, many countries express increasing interest in post-ITER programs toward the realization of fusion power. Since the middle of the 2000s, Japanese reactor studies have been devoted to DEMO conceptual designs. Japan is currently working on the design activity of a steady-state Japanese DEMO (JA-DEMO) with a plasma major radius of 8.5 m and fusion power of 1.5 GW[1]. The huge power exhaust concept and an appropriate divertor design are the common critical issues.

According to the physics design of JA-DEMO, the exhausted thermal power P_{sep} from the core plasma to the open field region reaching the wall surfaces, i.e., the scrape-off layer (SOL), is reported to 250 ~ 300 MW, which is about 2 ~ 3 times larger than ITER. Therefore, it is one of the biggest challenges for the design and operation of JA-DEMO to handle such a huge heat flux onto the plasma-facing components, especially the divertor targets. This motivates the exploration of possible solutions to dissipate power efficiently in the SOL and divertor region to ensure the maximum steady-state power load at the divertor target below 10 MW m^{-2} (the engineering limit of heat load for tungsten divertor targets) in JA-DEMO. Previously the divertor power exhaust for JA-DEMO has been investigated by the SONIC code[2]. So, it is a high priority task to evaluate the performance of power exhaust for JA-DEMO divertor by SOLPS-ITER code[3][4] and then make a comparison, which may contribute to the improvement of prediction capability by integrated divertor codes.

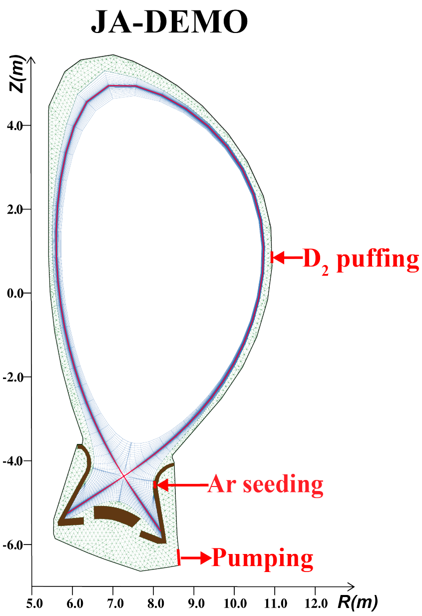

Fig.1 The divertor geometry for JA-DEMO and physical meshes for plasma (blue) and for neutrals (green). Locations of fuel gas injections (D_2), seeding impurity (Ar) and the pumping are marked in red

With the same equilibrium magnetic configuration used by SONIC, firstly the SOLPS-ITER mesh for JA-DEMO divertor was developed including a quadrangular grid (blue) for B2.5 plasma code and triangular grid (green) for EIRENE neutral code, as shown in figure 1. The injection positions of fueling gas D_2 and radiation impurity Ar are also marked in red. The puffing rate for D_2 is fixed to be 7.0×10^{22} atoms/s and the seeding rate for Ar is scanned from 1.0×10^{19} to 1.0×10^{20} atoms/s respectively. According to the plasma scenario of JA-DEMO, the total input power flowing from the core to the boundary plasma is assumed to be $P_{core/egde}$ = 250/300 MW. Owing to the core plasma radiation loss, there will be less power crossing the separatrix. Similar to the previous results by SONIC, both inner and outer divertor target can achieve the partial detachment with low electron and ion temperature (~1 eV) at the strike point, which will cause the less erosion of divertor targets and increase the lifetime of divertor target. Moreover, the corresponding heat load including surface recombination, radiation load and neutral flux load as well as plasma heat flux at the inner and outer divertor target can be controlled well below the engineering limit of 10 MW m^{-2}, as shown in figure 2.

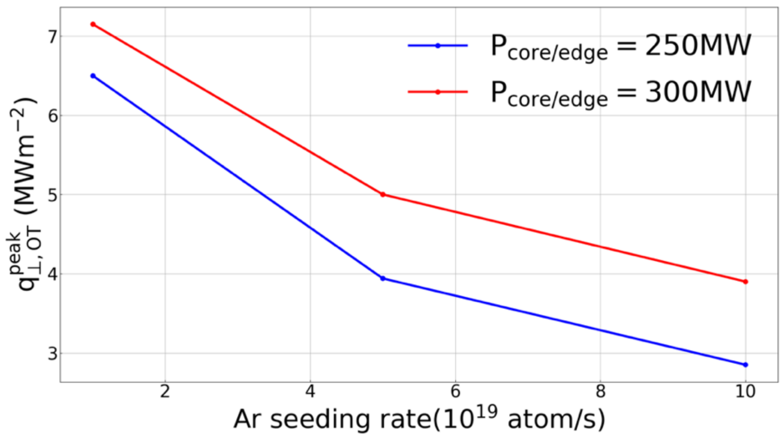

Fig.2 The peak heat load on the outer divertor target as a function of Ar seeding rate with $P_{core/egde}$ = 250/300 MW

In summary, for JA-DEMO seeding Ar impurity can increase the corresponding radiation power loss efficiently, so it is so significant for controlling heat load on the divertor targets. Under different scenarios ($P_{core/edge}$ = 250 and 300 MW), the heat flux density and electron temperature at the divertor targets can be controlled well(<10MW/m^2) with low $n_{e,sep}$ = $2.0\sim3.5 \times 10^{19}$ m^{-3}. The reduction in the heat load and target T_e by SOLPS-ITER are so far qualitatively consistent with those by SONIC. In future, the operation window of the target heat load, $n_{e,sep}$ and impurity concentration in the plasma edge will be investigated as a function of Ar seeding and D-gas puff rates for the two $P_{core/edge}$ cases.

Acknowledgment

SOLPS-ITER simulations were carried out within the framework of the BA DEMO Design Activity, using the JFRS-1 supercomputer system at CSC, IFERC, Rokkasho, Japan.

References

[1] Tobita, K. et al. Fusion Sci. Technol. 75 (2019) 372-383.

[2] Asakura N. et al. Nucl. Fusion 61 (2021) 126057.

[3] Bonnin X., Dekeyser W., Pitts R., Coster D., Voskoboynikov S. and Wiesen S. Plasma Fusion Res. 11（2016） 1403102

[4] Wiesen S. et al. J. Nucl. Mater. 463 (2015) 480

Development of Core-SOL-Divertor Model for Simulating Tokamak Plasmas with Impurities

Apiwat WISITSORASAK[1)], Naohiro Kasuya[2)],Atsushi Fukuyama[3)]

[1)]*Department of Physics, King Mongkut's University of Technology Thonburi, Bangkok, Thailand*
[2)]*Research Institute for Applied Mechanics, Kyushu University, Fukuoka, Japan*
[3)]*Department of Nuclear Engineering, Kyoto University, Kyoto, Japan*

20 December 2024

The dynamics of plasma in the scrape-off layer (SOL) is critically important. To simulate plasma in this region, one may reduce the complexity of the problem by only considering transport along a magnetic field line. Hayashi et al. (Journal of Nuclear Materials, 363, 1044-1049, 2007) proposed the dynamic five-point model based on a fluid description for determining local plasma properties at five specific locations along the SOL and divertor regions. In this work, we extend the five-point model by including the effects of impurities in the SOL region. These models will provide boundary conditions for impurity transport in the core and can be used for simulating complex plasmas in both the core and SOL regions.

Keywords: impurity transport, scrape-off layer (SOL), tokamak, 5-point model

1 Introduction

Impurities in tokamak plasma introduce several deleterious effects on the overall performance of the devices. A large amount of impurities can dilute the fuel and reduce the rate of fusion reactions. Furthermore, one of the most immediate effects is the loss of radiated power, which leads to lower plasma temperatures. For example, impurity ions such as oxygen and carbon, originating from the tokamak vessel, strongly cool the plasma near the edge. However, excessive edge cooling destabilizes the plasma and leads to plasma disruption, which can severely damage the wall and other structures [1]. On the other hand, metal ions from the plasma-facing components, such as tungsten, can travel farther from the edge and cause significant radiation in the core. This prevents the plasma from reaching a high enough temperature for ignition. Hence, the concentration of impurities should be minimized. For a tokamak with a divertor configuration, the impurities should be pumped away near the divertor; otherwise, they will accumulate in the vessel. Despite the downside effects of impurities, the radiation of plasma impurities nevertheless has some helpful consequences. Injection of noble gases such as argon or neon is intentionally used to increase radiation in the edge region of the plasma. A well-controlled amount of these seeded impurities helps to disperse the plasma power exhaust over wider surface areas and reduce the temperature in front of the plasma-facing components.

2 Methodology

To dynamically model the SOL and divertor plasma, one may reduce the complexity of the problem by considering only the transport along a magnetic field line. Instead of using a 1D or 2D transport model, one can focus on the relevant physical quantities of the plasma at specific points along the field line. The simplest model is the so-called two-point model, which considers only two points: the upstream (or stagnation point) and the target point. However, the two-point model does not account for asymmetric transport. A five-point model was originally proposed by Hayashi-san to study thermoelectric instability. It can also be used to model the dynamic response of SOL-divertor plasma during an ELM crash, which may induce thermoelectric instability and large SOL currents [2]. The model also only considers the transport of hydrogenic species without explicitly including impurities. In this work, we first describe the five-point model. The impurity transport will be solved in the background of the hydrogenic species and will be introduced later in this section.

The geometry of the five-point model is shown in Figure 1. The model considers the flux tube closest to the separatrix in single-null or double-null plasmas. The flux tube is divided into four regions. The fluid equations are integrated and reduced to a set of nonlinear algebraic equations with physical variables at the five positions.

author's e-mail: apiwat.wis@kmutt.ac.th

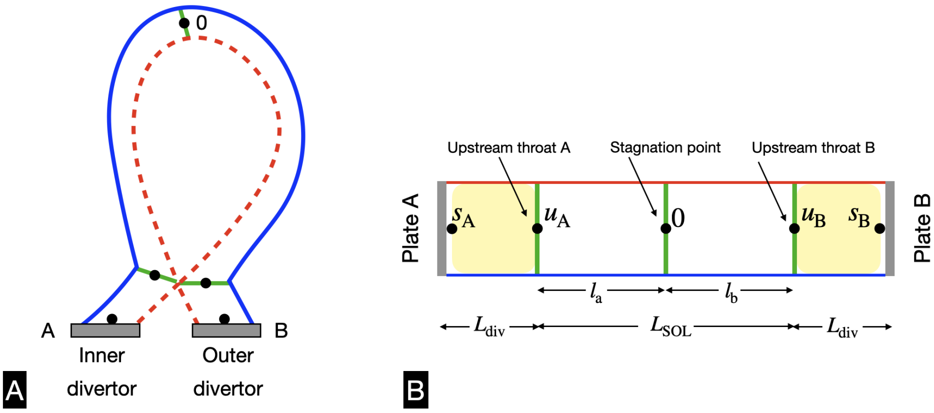

Fig. 1 Schematic diagram showing the geometry of the five-point model which considers the transport along the magnetic field.

2.1 Model Equations

The transport equations of the hydrogenic species can be summarized as follows.

$$L_{\mathrm{SOL}}\frac{\mathrm{d}n_0}{\mathrm{d}t} = -\Gamma_{\mathrm{uB}} - \Gamma_{\mathrm{uA}} + S_0 L_{\mathrm{SOL}}, \tag{1}$$

$$L_{\mathrm{div}}\frac{\mathrm{d}n_{sB}}{\mathrm{d}t} = \Gamma_{uB} - \Gamma_{sB} + S_B L_{\mathrm{div}}, \tag{2}$$

$$L_{\mathrm{div}}\frac{\mathrm{d}n_{sA}}{\mathrm{d}t} = \Gamma_{uA} - \Gamma_{sA} + S_A L_{\mathrm{div}}, \tag{3}$$

$$\frac{m_i}{2}\left(l_b + (1+R_B)L_{\mathrm{div}}\right)\frac{\mathrm{d}\Gamma_{uB}}{\mathrm{d}t} = n_0(T_{e,0} + T_{i,0}) - n_{sB}\left(2T_{e,sB} + (1+g)T_{i,sB}\right), \tag{4}$$

$$\frac{m_i}{2}\left(l_a + (1+R_A)L_{\mathrm{div}}\right)\frac{\mathrm{d}\Gamma_{uA}}{\mathrm{d}t} = n_0(T_{e,0} + T_{i,0}) - n_{sA}\left(2T_{e,sA} + (1+g)T_{i,sA}\right), \tag{5}$$

$$\begin{aligned}\frac{3}{2}\frac{\mathrm{d}n_0 T_{e0}}{\mathrm{d}t} &= -Q_{e,uB} - Q_{e,uA} - J(\phi_{uB} - \phi_{uA}) \\ &\quad + (W_{e0} + W_{e,eq,0})L_{\mathrm{SOL}},\end{aligned} \tag{6}$$

$$\frac{3}{2}\frac{\mathrm{d}n_0 T_{i0}}{\mathrm{d}t} = -Q_{i,uB} - Q_{i,uA} + (W_{i0} + W_{i,eq,0})L_{\mathrm{SOL}}, \tag{7}$$

$$\begin{aligned}\frac{3}{2}\frac{\mathrm{d}n_{sB} T_{e,sB}}{\mathrm{d}t} &= Q_{e,uB} - Q_{e,sB} - J(\phi_{uB} - \phi_{sB}) \\ &\quad + (W_{e,B} + W_{e,\mathrm{eq},B})L_{\mathrm{SOL}},\end{aligned} \tag{8}$$

$$\begin{aligned}\frac{3}{2}\frac{\mathrm{d}n_{sA} T_{e,sA}}{\mathrm{d}t} &= Q_{e,uA} - Q_{e,sA} - J(\phi_{uA} - \phi_{sA}) \\ &\quad + (W_{e,A} + W_{e,\mathrm{eq},A})L_{\mathrm{SOL}},\end{aligned} \tag{9}$$

$$\frac{3}{2}\frac{\mathrm{d}n_{sB} T_{i,sB}}{\mathrm{d}t} = Q_{i,uB} - Q_{i,sB} + (W_{i,B} + W_{i,\mathrm{eq},B})L_{\mathrm{SOL}}, \tag{10}$$

$$\frac{3}{2}\frac{\mathrm{d}n_{sA} T_{i,sA}}{\mathrm{d}t} = Q_{i,uA} - Q_{i,sA} + (W_{i,A} + W_{i,\mathrm{eq},A})L_{\mathrm{SOL}}. \tag{11}$$

The equations for the impurity species are as follows: here, $j = 1, 2, 3, ..., z_{\mathrm{max}}$ denotes the ionization states.

$$L_{\mathrm{SOL}}\frac{\mathrm{d}n_{j,0}}{\mathrm{d}t} = -\Gamma_{j,\mathrm{uB}} - \Gamma_{j,\mathrm{uA}} + L_{\mathrm{SOL}}\left(n_{j-1,0}\alpha_{j-1,0} - n_{j,0}\alpha_{j,0}\right), \tag{12}$$

$$L_{\mathrm{div}}\frac{\mathrm{d}n_{j,\mathrm{sA}}}{\mathrm{d}t} = \Gamma_{j,\mathrm{uA}} - \Gamma_{j,\mathrm{sA}} + L_{\mathrm{div}}\left(n_{j-1,\mathrm{sA}}\alpha_{j-1,\mathrm{sA}} - n_{j,\mathrm{sA}}\alpha_{j,\mathrm{sA}}\right), \tag{13}$$

$$L_{\mathrm{div}}\frac{\mathrm{d}n_{j,\mathrm{sB}}}{\mathrm{d}t} = \Gamma_{j,\mathrm{uB}} - \Gamma_{j,\mathrm{sB}} + L_{\mathrm{div}}\left(n_{j-1,\mathrm{sB}}\alpha_{j-1,\mathrm{sB}} - n_{j,\mathrm{sB}}\alpha_{j,\mathrm{sB}}\right), \tag{14}$$

$$\begin{aligned}\frac{m_Z}{2}\left(l_{\mathrm{b}} + (R_j+1)L_{\mathrm{div}}\right)\frac{\mathrm{d}\Gamma_{j,\mathrm{uB}}}{\mathrm{d}t} &= n_{j,0}T_{\mathrm{H},0} - 2n_{j,\mathrm{sB}}T_{\mathrm{H,sB}} \\ &\quad + \frac{m_Z}{\tau_j}\left[\frac{1}{2}n_{j,0}v_{\mathrm{H},0} + \frac{1}{2}n_{j,\mathrm{sB}}v_{\mathrm{H,sB}} + \frac{m_Z}{2}\left(l_{\mathrm{b}} + (R_j+1)L_{\mathrm{div}}\right)\Gamma_{j,\mathrm{uB}}\right]\end{aligned}$$

$$+m_z\left(l_\mathrm{b}+(R_j+1)L_\mathrm{div}\right)\left(\alpha_{j-1,\mathrm{uB}}\Gamma_{j-1,\mathrm{uB}}-\alpha_{j,\mathrm{uB}}\Gamma_{j,\mathrm{uB}}\right), \tag{15}$$

$$\begin{aligned}\frac{m_Z}{2}\left(l_\mathrm{b}+(R_j+1)L_\mathrm{div}\right)\frac{\mathrm{d}\Gamma_{j,\mathrm{uA}}}{\mathrm{d}t} &= n_{j,0}T_{\mathrm{H},0}-2n_{j,\mathrm{sA}}T_{\mathrm{H,sA}}\\ &+\frac{m_Z}{\tau_j}\left[\frac{1}{2}n_{j,0}v_{\mathrm{H},0}+\frac{1}{2}n_{j,\mathrm{sA}}v_{\mathrm{H,sA}}+\frac{m_Z}{2}\left(l_\mathrm{b}+(R_j+1)L_\mathrm{div}\right)\Gamma_{j,\mathrm{uA}}\right]\\ &+m_z\left(l_\mathrm{b}+(R_j+1)L_\mathrm{div}\right)\left(\alpha_{j-1,\mathrm{uA}}\Gamma_{j-1,\mathrm{uA}}-\alpha_{j,\mathrm{uA}}\Gamma_{j,\mathrm{uA}}\right).\end{aligned} \tag{16}$$

2.2 Algorithm

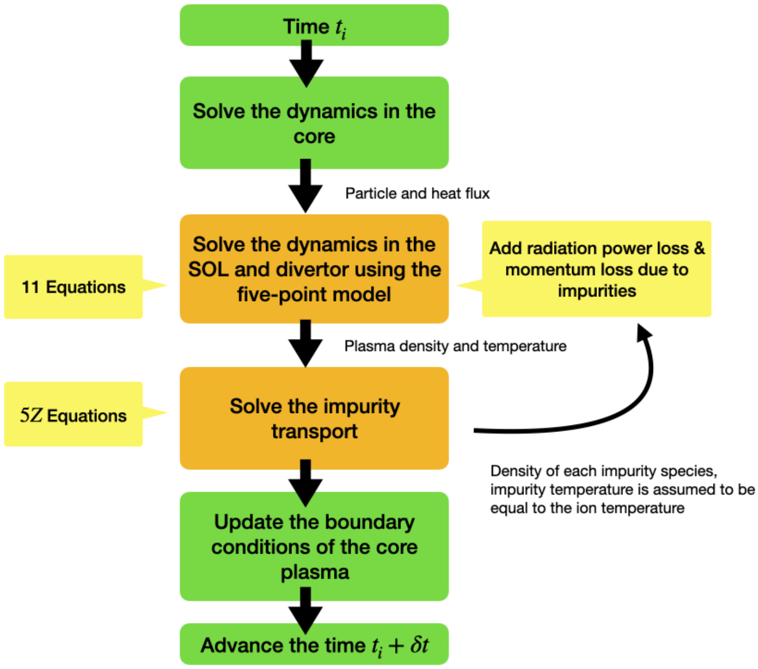

Fig. 2 Algorithm for solving the extended five-point model.

The impurity transport model can be coupled with the original five-point model to predict the densities and temperatures of both hydrogenic and impurity species. This combined model shall be named the SOL module. The SOL module can then be integrated into the main plasma simulation for the core region as follows (see Figure 2):

- At each time step, the main simulation numerically solves the plasma dynamics in the core and provides the particle and heat fluxes to the SOL module.
- In the SOL module, the original five-point model is first solved using the classical Runge-Kutta method (RK4), yielding the densities and temperatures at specific points along the field line.
- Assuming that the impurity ions share the same temperature as the main ions, the impurity transport model is then solved to determine the densities of the impurity species.
- These impurity densities are returned to the core simulation, updating the boundary conditions for the next time step.

3 Results and Discussion

In the present work, we have developed a computer code using Fortran programming to solve the dynamical equations for the densities and temperatures in the core, the scrape-off layer (SOL), and the divertor regions, as described in the previous section. This model requires the geometry of the SOL and divertor regions, the particle flux from the core, and the heat flux from the core as input information. The user must also specify the type of main plasma ions and impurity species.

To demonstrate the usability of the code, we have assumed that the characteristic lengths of the SOL and divertor regions are L_SOL = 100 m and L_div = 4 m, respectively. Protons are assumed to be the main plasma ions, and carbon is assumed to be the impurity species. We further assume that the particle flux from the core linearly increases from 2.0×10^{22} s^{-1} to 3.2×10^{22} s^{-1} within 0.1 ms, and the heat flux similarly increases from 2.0 MW to 2.2 MW within 0.1 ms. Figure 3 illustrates

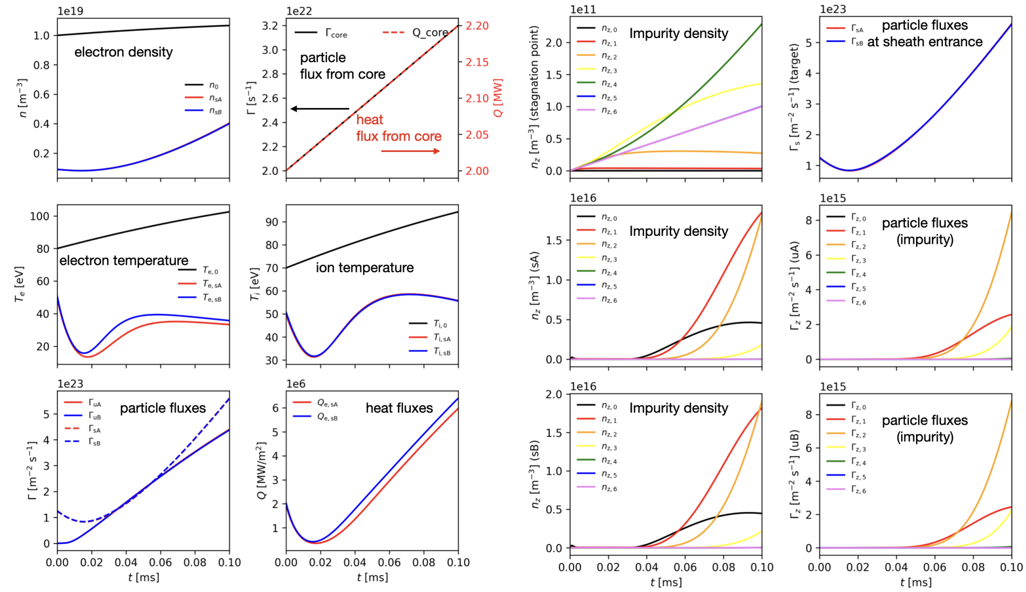

Fig. 3 Case 1: Low particle and heat fluxes. The figures show the time evolution of the plasma densities (n_0, n_{sA}, n_{sB}), temperatures (T_{e0}, T_{i0}, $T_{e,sA}$, $T_{e,sB}$, $T_{i,sA}$, $T_{i,sB}$), particle and heat fluxes (Γ_{uA}, Γ_{uB}, Γ_{sA}, Γ_{sB}), and impurity densities of different charge states (n_j) at different locations.

the electron densities, electron temperatures, ion temperatures, particle fluxes, heat fluxes, impurity densities, and impurity particle fluxes at each location.

4 Summary

We have successfully extended the five-point model to include the effects of impurities in the SOL regions. The model consists of 11 + 5Z dynamical equations, which can be numerically solved using the classic Runge-Kutta method. The model requires geometric information of the SOL and divertor regions, as well as the types of the main plasma ions and impurities, and their initial values as input. A Fortran program has been developed to simulate the dynamics of the plasma in the SOL and divertor regions based on this model. It allows us to compute the evolution of the densities and temperatures at each location along the SOL and divertor regions. Note that this model assumes that the impurities have the same temperature as the main plasma ions.

In future work, we plan to extend the model to simulate the SOL plasma in the detached regime, where high recycling fluxes occur near the divertor targets. To couple the extended 5-point model to the transport calculations in the core region, we will implement a new module for the TASK code, namely TASK/SOL, which is based on this model. Validation of the model with experimental data or other simulation codes will be conducted.

Acknowledgement

This project is financially supported by the Research Institute for Applied Mechanics, Kyushu University, under the International Joint Research Program for 2024, and by the Thailand Science Research and Innovation (TSRI) Basic Research Fund for the fiscal year 2024 under project number 197267.

References

[1] P. C. Stangeby *et al.*, *The plasma boundary of magnetic fusion devices*, vol. 224. Institute of Physics Publishing Bristol, 2000.

[2] N. Hayashi, T. Takizuka, and M. Hosokawa, "Modeling of dynamic response of sol-divertor plasmas to an elm crash," *Journal of nuclear materials*, vol. 363, pp. 1044–1049, 2007.

Kinetic modelling of W impurity transport in SOL/divertor plasmas by IMPGYRO code

Shohei YAMOTO[1)], Yuki HOMMA[1)], and Kazuo HOSHINO[2)]

[1)]QST, [2)]Keio Univ.

Tungsten (W) is currently regarded as one of the most feasible candidates for the plasma-facing components (PFCs). Once the W impurities sputtered from the PFCs penetrate the main plasma, the large radiation cooling and fuel dilution, which leads to the deterioration of the main plasma performance, take place. Therefore, to control W impurity transport are indispensable for future fusion reactors. To understand W transport, we are continuing to develop the kinetic impurity transport code IMPGYRO for SOL/divertor in fusion reactors. The IMPGYRO has obtained following unique features compared to other existing kinetic impurity transport codes through the 15-years development activity; (i) the exact Larmor motion of impurity ions are computed so that the effects of drifts are automatically taken into account, (ii) the Coulomb collision between impurities and background plasma ions are modelled by the Binary Collision Method which kinetically calculates more precise friction and thermal forces, and (iii) the background plasma transport and impurity transport are computed self-consistently by the coupled calculation with SOL/divertor plasma transport code such as SOLPS-ITER.

In this study, the effect of drifts of background plasma to W impurity transport has been investigated. The background plasma parameters of ITER are computed by the SOLPS-ITER code. The W generation is assumed to be a point source located on the outer target for simplicity. Therefore, the sputtering process of W is neglected. The two cases are compared: (A) W transport on the background plasma without drifts, (B) W transport on the background plasma with drifts. In case A, the W impurities are transported towards the outer midplane by the thermal force. Then, they penetrate into the core edge boundary. On the other hand, in case B, the W impurities reached to the core edge is transported to the region just above X-point and then part of the W impurities re-enters the SOL. Above trend results in low W flux into the core boundary. Above result suggests that the effect of drifts of background plasma can play a key role not only in the main plasma but also in the SOL/divertor regions, with regards to the W impurity transport.

22nd Burning Plasma Simulation Initiative (BPSI) Meeting
RIAM, Kyushu University, Fukuoka, Japan, December 19-20, 2024

Physics Study of Confinement Enhancement in KSTAR FIRE mode

G.J. Choi, Y.-S. Na[2], T.S. Hahm[2], C. Sung[1], H. Han[3], S.J. Park[2], D. Kim[1], C.H. Heo[2], J.H. Lee[2], S.C. Hong[3], J. Kang[3], J. Candy[4], Y.W. Cho[5] and B.J. Kang[6]

[1] Department of Nuclear and Quantum Engineering, KAIST, Korea
[2] Department of Nuclear Engineering, Seoul National University, Korea
[3] Korea Institute of Fusion Energy, Korea
[4] General Atomics, USA
[5] Nanyang Technological University, Singapore
[6] National Institute for Fusion Science, Japan

Recently, a novel stationary internal transport barrier (ITB) was established in KSTAR tokamak in NB (neutral beam) heated plasmas [1,2]. Physics studies have revealed that fast ions play crucial roles to this new enhanced confinement regime, so it is coined to Fast-Ion-Regulated Enhancement (FIRE) mode. A noticeable characteristic of the FIRE mode is that there is no significant change in the Alfvenic activities during the transition and in early phase.

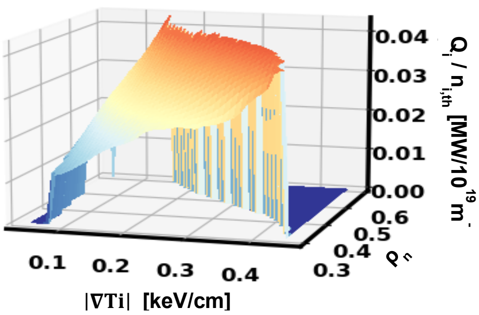

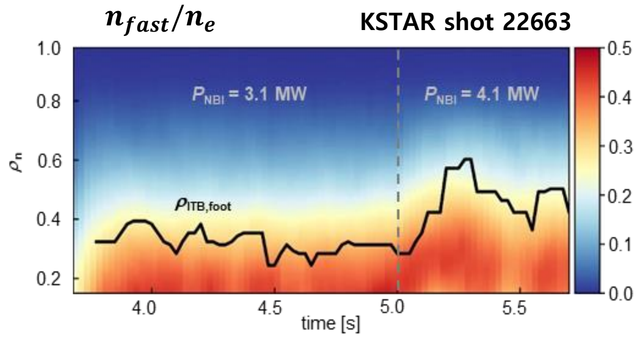

Figure 1. Ion energy flux landscape (left) and radial-time plot of fast ion fraction in KSTAR FIRE mode (right). The formation of S-curve in the flux-gradient relation can be found on the left, and correlation of ITB foot with fast ion fraction can be found on the right.

Gyrokinetic simulations [3], analytic theory [4,5] and predictive modeling [6] have shown that all the three of electromagnetic (EM) effect, dilution, and ExB shearing contribute to suppression of turbulent transport in the FIRE mode. Note that the dilution of thermal ions due to significant fast ion population is the simplest, and thus fundamental, effect of fast ions as a different ion species. The important role of dilution in KSTAR FIRE mode reminds us of the usefulness of the concept of energetic particles, which denotes the high-energy non-thermal part in the full fast ion distribution.

Gyrokinetic simulations of ITG (Ion Temperature Gradient) turbulence stability with Maxwellian and realistic fast ion distributions have shown that fast ion distribution doesn't have a significant impact on turbulence. This result indicates that wave-particle interactions between ITG turbulence and fast ions is not significant in KSTAR FIRE mode.

Analytic theories of dilution effect on nonlinear turbulence suppression by zonal flow self-generation [4,5] have shown that frequency mismatch among the main and sideband turbulence modes, the main defender of the zonal flow self-generation in the collisionless limit, is significantly reduced by dilution so that bifurcation to the enhanced confinement regime becomes easier with larger fast ion fraction. In the case of broadband turbulence, the frequency mismatch is characterized by qv_{gx}, the radial group velocity v_{gx} multiplied by zonal flow radial wavenumber q.

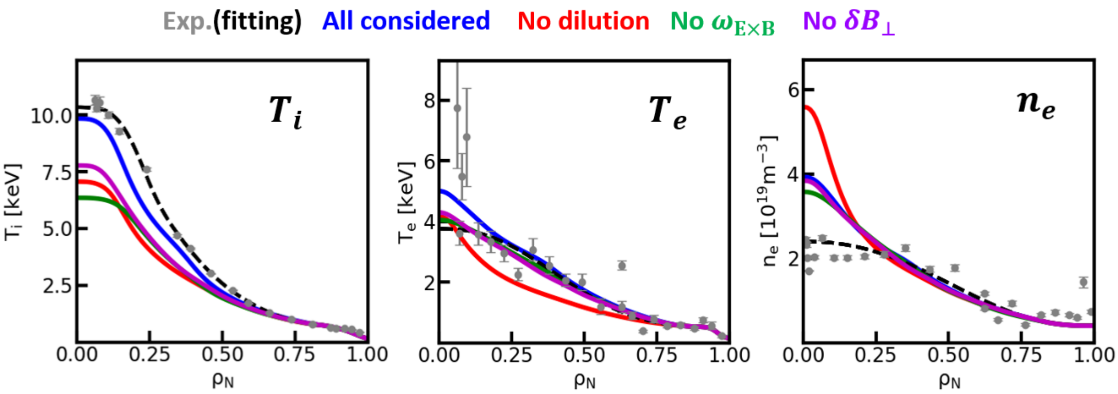

Figure 2. Result of predictive modeling using TRIASSIC. The ion temperature (left) clearly shows that all the dilution, ExB shear and EM effect contribute to the confinement enhancement in FIRE mode.

A very recent work on the edge turbulence characteristics in KSTAR FIRE mode has revealed that the FIRE mode edge has an I-mode characteristics [7]. That is, the FIRE mode edge has temperature pedestal with L-mode-like edge density profile. Furthermore, weakly-coherent mode (WCM) has been observed after entering the FIRE mode from density fluctuation spectra, measured by Beam Emission Spectroscopy (BES). Cross-bicoherence analyses further showed nonlinear interaction of WCM with zonal flow (2-4 kHz) at the radial location where WCM is the strongest.

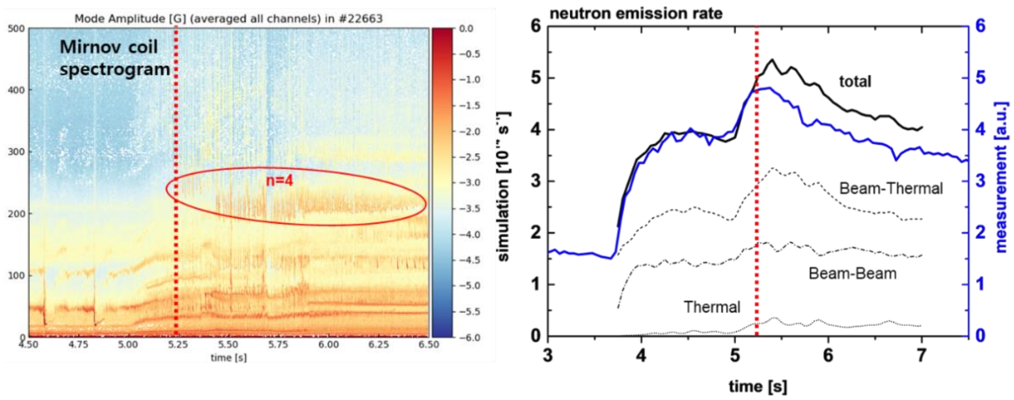

Figure 3. Experimental observations of the excitation of Alfvenic modes in the later phase of FIRE mode (left) and accompanied confinement degradation (right).

In the later phase of the KSTAR FIRE mode, significant changes in the Alfvenic activities, such as excitation of TAE (toroidal Alfven eigenmode), eventually degrade plasma performance, preventing further confinement enhancement [6]. In addition to the TAE, a core-localized lower-frequency Alfvenic mode is often observed, which has a weak impact on the performance for weaker B_T=1.8 T, whereas the impact is quite significant for higher B_T=2.5 T. Physics analysis using gyrokinetic simulation on the Alfvenic modes in the later phase of FIRE mode is ongoing.

References

[1] H. Han, S.J. Park et al., Nature 609, 269 (2022)
[2] H. Han et al., Phys. Plasmas 31, 032506 (2024)
[3] D. Kim et al., Nucl. Fusion 63, 124001 (2023)
[4] T.S. Hahm et al., Phys. Plasmas 30, 172501 (2023)
[5] G.J. Choi, P.H. Diamond and T.S. Hahm, Nucl. Fusion 64, 016029 (2024)
[6] Y.-S. Na et al., under review in Nucl. Fusion (2025)
[7] C.H. Heo et al., accepted to Nucl. Fusion (2025)

Excitation of inward particle fluxes with nonlinear coupling and turbulence spreading in tokamak plasmas

R. Miyamoto[1], N. Kasuya[1,2], M. Yagi[3]

[1]IGSES Kyushu Univ., [2]RIAM Kyushu Univ., [3]QST.

1. Introduction

In a fusion reactor, particle supply to core plasma is an important issue to sustain high density plasma. The pellet injection method is effective to supply fuel particles to the core plasma. In pellet injection, peaking density profiles are temporally formed and associated fluctuations have been observed [1]. In such regions, it is known that a particle flux toward the center of the core plasma is generated [2]. The inward fluxes are also observed in the global simulation [3], therefore, we carry out the global turbulence simulation to understand the sustainment mechanism of the inward particle fluxes.

2. Simulation model

The reduced MHD code R5F [4] was used for the simulations. The code solves the time evolution of five fields (electrostatic potential ϕ, vector potential in the magnetic field direction A, velocity in the magnetic field direction V, density N, and electron temperature T_e) in three spatial dimensions using the vorticity equation, ohm's law, equation of ion motion in the magnetic field direction, continuity equation, and evolution equation for electron temperature;

$$\frac{d}{dt}\nabla_\perp^2 F = -\nabla_\parallel \nabla_\perp^2 A + \mu_{i\perp}\nabla_\perp^4 F - [2r\cos\theta, p] - \frac{q}{\varepsilon}\mu_i \frac{1}{r}\frac{\partial}{\partial r} r\left(V + \frac{q}{\varepsilon}\frac{\partial F}{\partial r}\right) - \frac{q}{\varepsilon}\frac{m_e}{m_i}\mu_e \frac{1}{r}\frac{\partial}{\partial r} r\left(V + \frac{q}{\varepsilon}\frac{\partial F}{\partial r} + \delta\nabla_\perp^2 A\right), \tag{1}$$

$$\frac{d}{dt}\left(A - \delta^2 \frac{m_e}{m_i}\nabla_\perp^2 A\right) = -\nabla_\parallel F + \eta_\parallel \nabla_\perp^2 A + \nabla_\parallel \delta P_e - 4\mu_{e\perp}\delta^2 \frac{m_e}{m_i}\nabla_\perp^2\nabla_\perp^2 A + \alpha_T \delta \nabla_\parallel T_e + \delta \frac{m_e}{m_i}\mu_e\left(V + \frac{q}{\varepsilon}\frac{\partial F}{\partial r} + \delta\nabla_\perp^2 A\right), \tag{2}$$

$$\frac{dV}{dt} = -\nabla_\parallel p + 4\mu_{i\perp}\nabla_\perp^2 V - \mu_i\left(V + \frac{q}{\varepsilon}\frac{\partial F}{\partial r}\right) - \frac{m_e}{m_i}\mu_e\left(V + \frac{q}{\varepsilon}\frac{\partial F}{\partial r} + \delta\nabla_\perp^2 A\right), \tag{3}$$

$$\frac{dN}{dt} + \beta\frac{dp}{dt} = -\beta\nabla_\parallel(v + \delta\nabla_\perp^2 A) + \eta_\perp \beta \nabla_\perp^2 p + \beta[2r\cos\theta, \phi - \delta p_e], \tag{4}$$

$$\frac{3}{2}\frac{dT_e}{dt} - \frac{\beta_e}{\beta}\frac{dn}{dt} = -\alpha_T \delta\beta_e \nabla_\parallel \nabla_\perp^2 A + \chi_{e\perp}\nabla_\perp^2 T_e + \varepsilon^2 \chi_{e\parallel}\nabla_\parallel^2 T_e - \frac{5}{2}\delta\beta_e[2r\cos\theta, T_e], \tag{5}$$

where $F = \phi + (\beta_i/\beta)\delta P_e$, $P_e = N + T_e$, $d_t := \partial_t + [\phi,\ ]$, $\nabla_\parallel := \nabla_\parallel^{(0)} - [A,\ ]$. The set of equations is normalized by the small radius a for the length and by the poloidal Alfvén time $a/(\varepsilon v_a)$ for the time, where ε is the inverse aspect ratio and v_a is the Alfvén velocity. The calculation parameters used for the simulation are as follows; small radius r=0.5 m, plasma beta $\beta_e = \beta_i = 5\times 10^{-3}, \beta = \beta_e + \beta_i$, inverse aspect ratio $\varepsilon = 0.33$, ion skin length $\delta = 10^{-2}$, mass ratio $m_e / m_i = 1/1836$, resistivity $\eta_\perp = 10^{-5}$, $\eta_\parallel = 10^{-5}$, thermal diffusion coefficient $\chi_{e\perp} =$

$10^{-5}, \chi_{e\parallel} = 10^{-5}$, the perpendicular ion and electron viscosity coefficients $\mu_{i\perp} = 10^{-5}, \mu_{e\perp} = 10^{-5}$, neoclassical viscosity coefficients $\mu_i = 4.6 \times 10^{-5}, \mu_e = 1.4 \times 10^{-3}$, and thermal coefficient $\alpha_T = 0.71$. In this study, the calculations were carried out by introducing an initial background density profile with a gaussian type peak (peak intensity:S_{amp}, peak width:Δ)

$$N(r,\theta,\zeta)|_{t=0} = N_0 \left[(1-r^8)^8 + S_{amp}\{\exp(-\xi_1^2/2\Delta^2) - \exp(-\xi_2^2/2\Delta^2)\}\right], \qquad (6)$$

where N_0 is a normalization factor, $\xi_1 = r - r_s, \xi_2 = 1 - r_s$ with peak position $r_s = 0.8$ and peak width $\Delta^2 = 0.003$. By this profile, 'strong turbulence region' with the largest density gradient and 'weaker turbulent region' with the negative density gradient are generated around $r = r_s$ (Fig. 1).

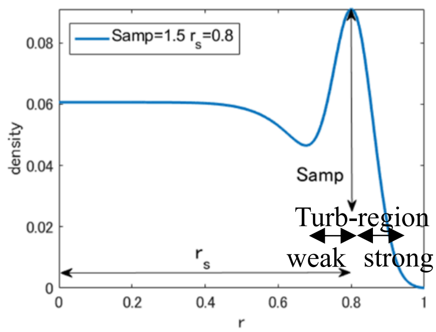

Fig. 1 Initial density profile with an inverted density gradient

3. Analysis results

This simulation uses the value $S_{amp} = 1.5$ [3]. From the continuity equation, the turbulent particle fluxes Γ_{turb} is given by the following form;

$$\Gamma_{turb} = \sum_{m,n} \left\{(1+\beta)N_{m,n}\frac{\partial\phi_{-m,-n}}{r\partial\theta} + \beta A_{m,n}\frac{\partial V_{-m,-n}}{r\partial\theta} + \beta\delta A_{m,n}\frac{\partial\nabla_\perp^2 A_{-m,-n}}{r\partial\theta}\right\}. \qquad (7)$$

The first term of this equation is relatively larger than the other terms, because the coefficient of the first term is larger, so we focused on this term in this analysis.

Figure 2(a) shows the radial profile of the turbulent particle fluxes. The inward particle fluxes were observed around $r = 0.75$. Figure 2(b) shows the time evolution of the particle fluxes averaged over $r = 0.7 \sim 0.76$ as following equation;

$$\Gamma_{inward} := \frac{\int_{0.7}^{0.76} \Gamma_{turb} r dr}{\int_{0.7}^{0.76} r dr}. \qquad (8)$$

Note that the integral region corresponds to the area where the inward fluxes are generated. In the latter part of the nonlinear phase (phase B), the particle fluxes are significantly increased compared to those in phase A. The analysis of the Fourier modes shows that the mode with $(m,n) = (-5,2)$ contributes to the increase in the particle fluxes in particular (Fig. 3), where m and n are the poloidal and toroidal mode number, respectively.

Next, so as to identify the driving source of the $(-5,2)$ mode, we evaluated the energy balance of the fluctuation;

$$\frac{\partial}{\partial t}\left(\frac{1}{2}\left|N_{m,n}\right|^2\right) = \left(1+\beta+\frac{2}{3}\beta_e\right)^{-1} \mathrm{Re}(L+NL_1+NL_2+NL_3), \tag{9}$$

where L in the right-hand side is the linear driving force term and $NL_1 \sim NL_3$ are the nonlinear driving force terms due to nonlinear coupling. Figure 4 shows the time evolution of the energy balance of the $(-5,2)$ mode, showing that the mode is strongly excited at $t = 97 \sim 120$ and is driven nonlinearly (NL_1) at $t = 97 \sim 113$ (defined as phase C-1). This nonlinear kick triggers the excitation of the $(-5,2)$ mode. Figure 5 shows the nonlinear mode coupling contribution to the $(-5,2)$ mode in this phase C-1. Typical nonlinear coupling contributions are $(-8,3)+(3,-1) \rightarrow (-5,2)$ and $(-10,4)+(5,-2) \rightarrow (-5,2)$. The $(3,-1) = (-3,1)^*$ component is a resonant mode with $q = 3$ rational surface at $r = 0.83$ in the outer strong turbulent region. The $(3,-1)$ mode becomes unstable in the strong turbulence region at first, and in C-1 phase, spreads radially to the weak turbulence region (turbulence spreading) as in Fig. 6.

Thus, in the weak turbulence region $r = 0.7 \sim 0.8$, the fluctuations mainly the $(-5,2)$ mode is excited and sustained by nonlinear coupling. The non-local mechanism is revealed in which the propagation of the fluctuations into the weak turbulent region by turbulence spreading further strongly drives the inward particle fluxes.

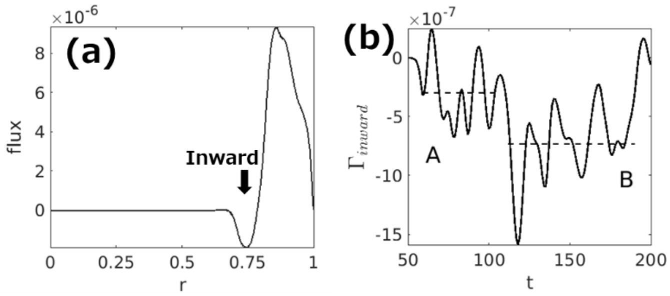

Fig. 2 (a) Snapshot of the radial profile of the particle fluxes $(t = 118)$. (b) Time evolution of Γ_{inward} defined as (8). Note that dashed lines for phases A and B represent averaged levels of the inward fluxes in each phase.

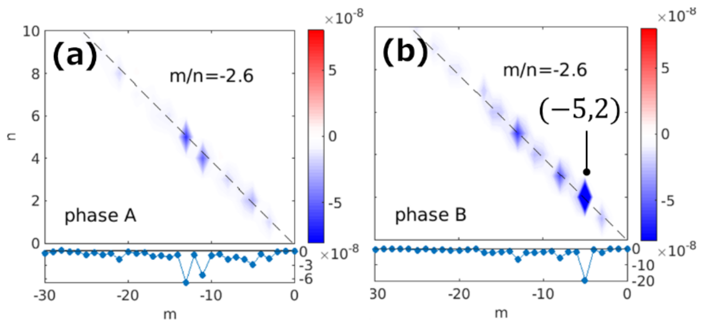

Fig. 3 Fourie mode decompositions of the particle fluxes averaged over (a) $t = 72 \sim 107$

(phase A) and (b) $t = 108 \sim 196$ (phase B). The bottom panels are the sum of n components.

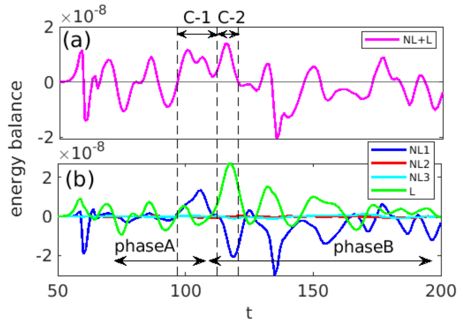

Fig. 4 Time evolution of the energy balance at $r = 0.75$. The terms in the (a) left and (b) right hand side of Eq. (9) are shown.

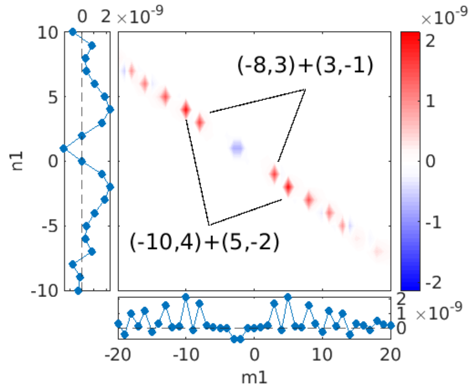

Fig. 5 Nonlinear coupling contribution to the $(-5{,}2)$ mode at $r = 0.75$ averaged over $t = 97 \sim 113$ (phase C-1). The left and bottom panels are the sum of m_1 and n_1 components, respectively.

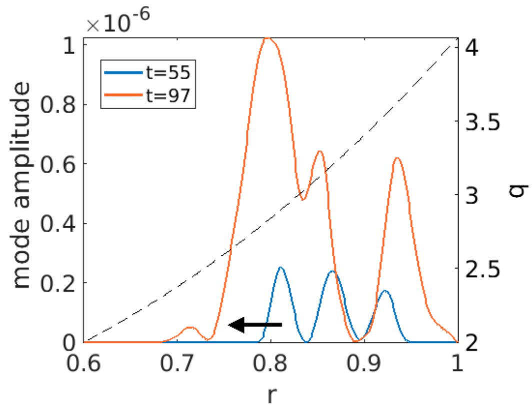

Fig. 6 Temporal change of the radial profile of the amplitude of the $(-3{,}1)$ mode at $t = 55$ and $t = 97$. The dashed line represents the safety factor profile. Note that the resonant rational surface of this mode $q = 3$ is located at $r = 0.83$.

4. Conclusion

The turbulence simulation was performed by introducing an initial background density profile with a peak near the plasma edge, and the radial inward turbulent particle fluxes were nonlinearly sustained. We evaluated its driving mechanism with the Fourier mode decomposition. The $(-5,2)$ mode contributes to the increase in the particle fluxes. Quantitative analyses of the energy balance of this fluctuation showed a dominant pair of mode coupling in the nonlinear driving force term. As a result, the non-local mechanism to enhance the inward particle fluxes is clarified, in which turbulence spreading for excitation and nonlinear couplings for sustainment are important in the weak turbulence region.

Reference

[1] S. Ohshima, *et al*, Sci. Reps., **12,** (2022) 14204.

[2] M. Yagi, *et al*, 16th BPSI Meeting (2018) 2-1.

[3] H. Todoroki, *et al*, Plasma Fusion Res. **18**, (2023) 1203052.

[4] M. Yagi, *et al.*, Nucl. Fusion **45**, (2005) 900.

Modeling of turbulent transport due to dissipative trapped electron mode in tokamak plasmas

S. Toda[1,2], M. Nunami[1,3], and N. Kasuya[4]
[1] *National Institute for Fusion Science*
[2] *Graduate Institute for Advanced Studies, SOKENDAI*
[3] *Graduate School of Science, Nagoya University*
[4] *Research Institute for Applied Mechanics, Kyushu University*

Turbulent transport is one of the most important subjects in research of toroidal plasmas. The purpose of this study is to quantify turbulent transport. Microscopic plasma instabilities are studied using electromagnetic gyrokinetic simulations. The trapped electron mode (TEM) where normalized electron collision frequency is less than unity[1] is called dissipative-TEM (d-TEM) in a high collisional regime. Plasma experiments at the PLATO device at the Research Institute for Applied Mechanics, Kyushu University have been started. Transport simulations using integrated code are carried out on the PLATO tokamak to forecast plasma performance and plasma profiles in the PLATO are predicted using an empirical model in the integrated code, the TASK code. In these plasmas, the electron collision frequency is typically less than the electron bounce collision frequency and the ion collision frequency is larger than the ion bounce collision frequency. Therefore, these plasmas are in a high collisional regime and the d-TEM is predicted to be unstable. We focus on the d-TEM and the ITG mode by using local gyrokinetic simulations. The GKV code[2] is used for local flux tube gyrokinetic simulation, using the Sugama (S) collision model operator[3] or the Lenard-Bernstein (LB) collision model operator.

The plasma profiles predicted by the TASK code in the PLATO are used. The linear simulation results using the S and LB collision operators are compared. The dependences of linear growth rate γ, and real angular frequencies ω, on the normalized poloidal wavenumber $k_y\rho_\mathrm{e}$, are studied, where k_x and k_y are the radial and poloidal wavenumbers, respectively. Using the S collision operator, the instabilities predicted in this study are driven by the d-TEM in the regions $0.005 \leq k_y\rho_\mathrm{e} \leq 0.020$ at $\rho = 0.47$ and $0.005 \leq k_y\rho_\mathrm{e} < 0.040$ at $\rho = 0.65$. The real angular frequency changes from the electron to ion diamagnetic drift motion direction at $\rho = 0.47$ and $\rho = 0.65$ when the poloidal wavenumber increases. This d-TEM is driven by the density gradient in this study. The d-TEM is predicted to be unstable at $\rho = 0.81$ in the all-poloidal wavelength region studied here. The linear growth rate for the d-TEM at $\rho = 0.81$ becomes larger than that at $\rho = 0.47$ because of the increase of R/L_n, therefore, the d-TEM becomes more unstable in the outer radial region. On the other hand, the ITG mode is excited in the regions $0.020 < k_y\rho_\mathrm{e} < 0.060$ at $\rho = 0.47$ and $0.040 \leq k_y\rho_\mathrm{e} < 0.060$ at $\rho = 0.65$. Instabilities in this study are found to be ballooning-typed. Using the LB collision operator, only the d-TEM is unstable in the $0.005 < k_y\rho_\mathrm{e} < 0.030$ region at all radial points. The differences between the results using S and LB collision operators are found. These are because the field particle part is included with momentum conservation and the collisionality term depends on the velocity in the S collision model operator[3]. If the gradient of T_i becomes larger using the LB collision operator, the ITG mode is found.

Next, we study the linear response of the zonal flows using the S and LB model collision operators. The linear response function of zonal flows $\mathcal{R}_{\tilde{k}_x}(t)$ is defined as $\mathcal{R}_{\tilde{k}_x}(t) = \left\langle \tilde{\phi}_{\tilde{k}_x,\tilde{k}_y=0}(t) \right\rangle / \left\langle \tilde{\phi}_{\tilde{k}_x,\tilde{k}_y=0}(t=0) \right\rangle$, where $\tilde{\phi}(= \phi/(T_\mathrm{e}\rho_\mathrm{e}/(eR)))$ is the electrostatic potential fluctuation. The residue levels at $\rho = 0.47$,

$\rho = 0.65$ and $\rho = 0.81$, which is defined as the value of $\mathcal{R}_{\tilde{k}_x}(t = 2500)$ here, are studied. The residue level using the S collision operator is larger than that using the LB one. The zonal flow decay time is defined as $\int_0^{2500} \mathcal{R}_{\tilde{k}_x}(t)dt$ in this article. The zonal flow decay time using the S collision operator is found to be twice as large as that using the LB collision operator. The linear simulation results suggest that the effect of the zonal flows on the turbulent transport using the S collision operator in the nonlinear simulation results is larger than that using the LB collision operator.

A nonlinear gyrokinetic simulation is carried out. Nonlinear gyrokinetic analysis results are studied for the time evolutions of the squared turbulent potential fluctuation, $\mathcal{T}\left(= \Sigma_{\tilde{k}_x,\tilde{k}_y\neq 0}\left\langle|\tilde{\phi}_{\tilde{k}_x,\tilde{k}_y}|^2\right\rangle/2\right)$ and the squared zonal flow potential, $\mathcal{Z}\left(= \Sigma_{\tilde{k}_x,\tilde{k}_y=0}\left\langle|\tilde{\phi}_{\tilde{k}_x,\tilde{k}_y}|^2\right\rangle/2\right)$. Time evolutions for the squared potential fluctuations using the S and LB collision model operators are compared at $\rho = 0.47$, $\rho = 0.65$ and $\rho = 0.81$. To study the effect of the zonal flows, the values of $\bar{\mathcal{T}}$ and $\bar{\mathcal{Z}}$ at $\rho = 0.47, 0.65$ and 0.81 are examined. The symbol $^-$ represents the averaged values of $\mathcal{T}$ or $\mathcal{Z}$ of time t normalized by $R/v_{\rm te}$ from 3000 to 5000. The effect of the zonal flows on the turbulence by the S collision operator is predicted to be much larger than that by the LB one. The values of $\bar{\mathcal{Z}}/\bar{\mathcal{T}}$ at $\rho = 0.47, 0.65$ and 0.81 using the S and LB collision model operators are studied. The values of $\bar{\mathcal{Z}}/\bar{\mathcal{T}}$ using the S collision model operator are larger than those using the LB collision model operator. Next, the transport level is evaluated by the nonlinear simulation results. The averaged values over the time interval after the nonlinear saturation for $Q_{\rm e}$, $\chi_{\rm e}$, $Q_{\rm i}$, $\chi_{\rm i}$, Γ and D using the S and LB collision model operators are obtained, where Q_j is the energy flux and χ_j is the energy diffusivity for the species j. Here, Γ is particle flux and D is particle diffusivity. Energy and particle fluxes at $\rho = 0.47, 0.65$ and 0.81 are studied. The energy and particle diffusivities at $\rho = 0.47, 0.65$ and 0.81 are also studied. In almost cases, the transport levels using the S collision model operator are found to be smaller than those using the LB due to the effect of the zonal flows[4]. The set of the data is the basis for modeling the turbulent transport.

The electron and ion energy diffusivities are started to be modeled by the function $\chi_j/\chi_{\rm e}^{\rm GB} = C_{1j}\bar{\mathcal{T}}^{a_j}/(C_{2j} + \bar{\mathcal{Z}}^{b_j}/\bar{\mathcal{T}})$ for the species j. The effect of zonal flows is considered to be more effective for lower wavenumbers. The heat and particle flux spectra have peaks at the similar location at $k_{\rm y}\rho_{\rm e} = 0.005$ for d-TEM/ITG mode in the PLATO. Therefore, the values of b_j for the species j are similar. On the other hand, the value of $b_{\rm e}$ is smaller than that of $b_{\rm i}$ for ITG mode in the Large Helical Device[5], because the poloidal wavenumber spectra of $Q_{\rm e}$ take peaks at larger $k_{\rm y}\rho_{\rm i}$ values than those of $Q_{\rm i}$.

REFERENCES

[1]B. B. Kadomtsev and O. P. Pogutse, *Reviews of Plasma Physics, edited by M. Leontovich*, Vol. 5 (consultants Bureau, New York, 1970).

[2]T.-H. Watanabe and H. Sugama, Nucl. Fusion **46**, 24 (2006).

[3]H. Sugama, T. H. Watanabe, and M. Nunami, Phys. Plasmas **16**, 112503 (2009).

[4]S. Toda, M. Nunami, and N. Kasuya, Physics of Plasmas **31**, 032511 (2024).

[5]S. Toda, M. Nakata, M. Nunami, A. Ishizawa, T.-H. Watanabe, and H. Sugama, Phys. Plasmas **26**, 012510 (2019).

Automatic configuration of ECCD using genetic algorithm

R. Otani, M. Honda, S. Murakami
Kyoto University

1 Introduction

In JA-DEMO, it is expected that electron cyclotron (EC) heating will be performed using a large number of gyrotrons compared to current plasma experiment. By appropriately setting the input power of each gyrotron, it will become possible to flexibly tailor the EC current profile. However, manually configuring the settings of numerous gyrotrons to achieve an arbitrary current drive profile is challenging, and automation is required. In this study, a method for automatically configuring the conditions of the gyrotrons is developed using genetic algorithm, which is one of the mathematical optimization techniques. Additionally, using this method, integrated simulations for JA-DEMO are conducted to develop operation scenario that avoid MHD instabilities.

2 Numeric method

Heating and current drive by EC waves are evaluated using EC-hamamatsu[1] code, which analyzes the propagation of EC waves based on the ray tracing method. In the ray tracing method, interactions between EC waves generated by different gyrotrons are not considered, and the propagation of each EC wave is evaluated independently. In this case, the EC current profile driven by multiple gyrotrons becomes the linear sum of the EC current profile driven by each gyrotron. In other words, the total EC current profile $\boldsymbol{J}_{ec}[\mathrm{MA/m^2}]$, driven by gyrotrons with input frequency f and direction (θ, ϕ), is expressed as the linear combination of the unit-power EC current distributions $\boldsymbol{j}_{ec}(f, \theta, \phi)[\mathrm{MA/(m^2 \cdot MW)}]$, as described by (1):

$$\boldsymbol{J}_{ec} = \sum_i c_i \boldsymbol{j}_{ec}(f, \theta, \phi), \qquad (1)$$

where c_i denotes the input power of the i-th gyrotron. Here, (1) assumes that a plasma equilibrium is not altered by the EC current. As an example, Fig.1 shows the EC current profile $\boldsymbol{j}_{ec}(f, \theta, \phi)$ for each of the eight gyrotrons when driven with an EC power of 1 MW, and the EC current profile $\boldsymbol{J}_{ec}$ when they are used simultaneously at $c_i = 1\mathrm{MW}$, and it can be seen that $\boldsymbol{J}_{ec}$ can be found by combining $\boldsymbol{j}_{ec}(f, \theta, \phi)$.

The power $\boldsymbol{c}^*$ of the gyrotrons that constitute the desired EC current profile $\boldsymbol{J}_{target}$ is given by

$$\boldsymbol{c}^* = \arg\min_{\mathbf{c}} \|\boldsymbol{J}_{target} - \sum_i c_i \boldsymbol{j}_{ec}(f, \theta, \phi)\|^2 \qquad (2)$$

and is reduced to a mathematical optimization problem.

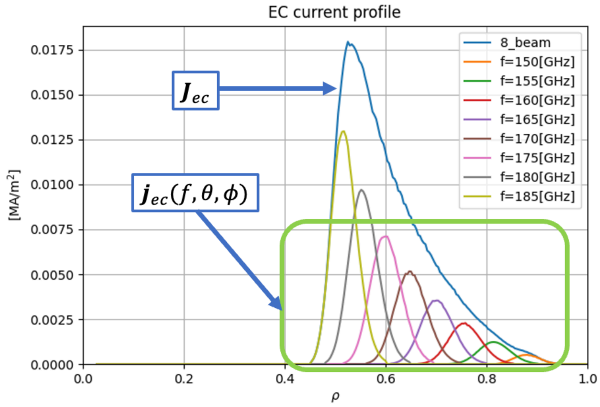

Fig.1: EC current profile driven by multiple gyrotrons

In this study, the genetic algorithm, characterized as an optimization method less prone to local minima, is used to determine $\boldsymbol{c}^*$.

Next, the changes in the magnetic field are reflected in $\boldsymbol{J}_{ec}$, which is constructed from the obtained $\boldsymbol{c}^*$. This is because the change in the equilibrium magnetic field caused by the EC waves is not considered in (1). In this study, ACCOME [2], which calculates the equilibrium magnetic field and plasma current self-consistently, is used to obtain an equilibrium magnetic field that is consistent with $\boldsymbol{J}_{ec}$. Then, the calculations are iterated until the equilibrium magnetic field and EC current converge. Therefore, in this method, the following calculations are repeated to construct the desired EC current profile.

1. For each gyrotron, the EC current profile $\boldsymbol{j}_{ec}(f, \theta, \phi)$ driven per unit power is calculated using EC-hamamatsu code.
2. The power $\boldsymbol{c}^*$ of the gyrotrons that constitute the desired EC current profile $\boldsymbol{J}_{target}$ is determined using genetic algorithm.
3. The equilibrium magnetic field that is consistent with $\boldsymbol{J}_{ec}$ is calculated using ACCOME.

Fig.2 shows the target profile $\boldsymbol{J}_{\mathrm{target}}$ with a Gaussian distribution shape, as well as the EC profile $\boldsymbol{J}_{ec}(\mathrm{itr})$ obtained at each iteration of the calculation. The EC current profile $\boldsymbol{J}_{ec}(\mathrm{itr0})$ in the early steps is significantly different from the target profile, but it is confirmed to converge sufficiently to the target profile after a few iterations.

3 Development of operation scenario of JA-DEMO

By incorporating this method into the integrated code GOTRESS+[3], an integrated simulation capable of real-

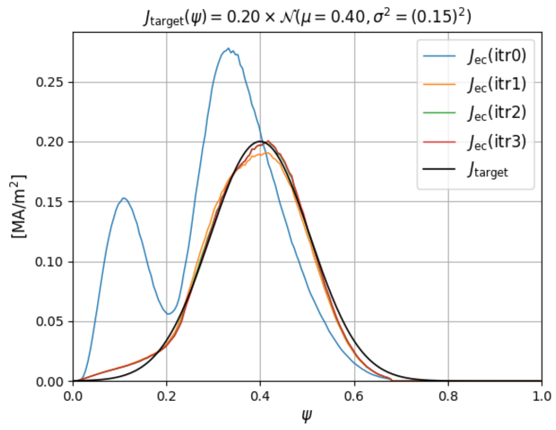

Fig.2: Automatic configuration of the EC current profile

izing the desired EC current profile has become possible. In this study, integrated simulations were conducted with the goal of developing a high-performance fusion plasma for JA-DEMO while avoiding MHD instabilities. To avoid the occurrence of the internal kink mode, the target profile $\boldsymbol{J}_{target}$ was designed to have a peak slightly outward. Additionally, this approach aims to locally heat the off-axis region with the relatively high density to increase fusion power while avoiding current drive in the magnetic axis.

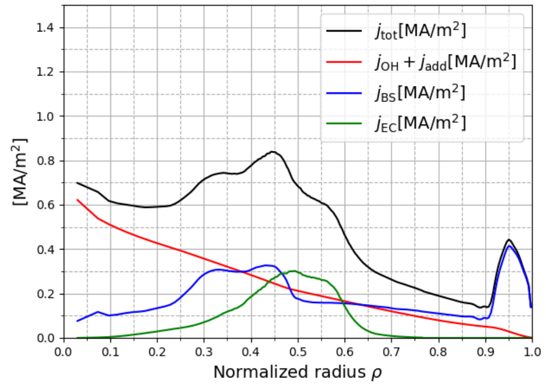

Fig.3: Current profiles of JA-DEMO operation scenario

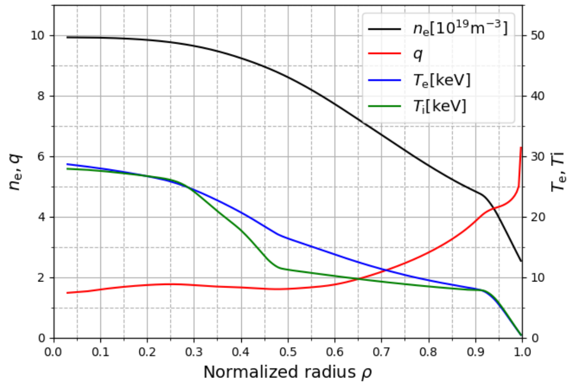

Fig.4: Plasma profiles of JA-DEMO operation scenario

	HH_{98y2}	β_N	$P_{fus}[GW]$	Q	f_{BS}	f_{GW}
target	1.13	2.6	1.085	13	0.46	1.2
result	1.182	2.68	0.900	8.20	0.48	1.25

Table.1: Target values and integrated simulation results of the JA-DEMO operation scenario

In the integrated simulation, an EC current profile with a peak outward (green line in Fig.3) was constructed, successfully suppressing the current flowing near the magnetic axis and avoiding the internal kink mode. Additionally, an internal transport barrier was formed near the peak of the total current density profile (blue and green lines in Fig.4), resulting in high fusion output. Table 1 compares the various target values expected for JA-DEMO with the results of the integrated simulation. Although the fusion output $P_{\rm fus}$ and energy gain Q are slightly lower, an MHD-stable plasma with good figures of merit close to the target values has been successfully developed.

4 Summary and perspectives

In JA-DEMO, a large number of gyrotrons are expected to be used for EC heating on a larger scale than current plasma experiment. As a result, it opens the way to arbitrarily construct the EC current profile by appropriately adjusting the gyrotrons power. However, it is difficult to manually configure the conditions of gyrotrons as usual. In this study, a method for automating this process has been developed. By incorporating this method into GOTRESS+, it has become possible to flexibly configure the current profile, making it easier to avoid MHD instabilities in the integrated simulation.

Suppressing MHD instabilities is not sufficient by only adjusting the EC current profile. This is because what is important for MHD stability is not just the EC current profile, but rather the total current profile, which also includes bootstrap current and Ohmic current. We will extend this method to automatically configure the total current profile.

References

[1] K Hamamatsu, T Takizuka, N Hayashi, and T Ozeki. *Plasma Physics and Controlled Fusion*, 49(12):1955, oct 2007.

[2] K. Tani, M. Azumi, and R.S. Devoto. *Journal of Computational Physics*, 98(2):332–341, 1992.

[3] M. Honda, N. Aiba, H. Seto, E. Narita, and N. Hayashi. *Nuclear Fusion*, 61(11):116029, oct 2021.

Particle and momentum transport analysis using multi-field singular value decomposition in plasma turbulence simulation

T. Kodahara, M. Sasaki

Nihon Univ.

1. Introduction

In magnetized plasmas, interactions between turbulence and structures drive abrupt phenomena such as Edge localized modes (ELMs) [1] and avalanches [2], which significantly impact confinement performance and wall damage. Developing analysis methods for these abrupt events is crucial for their prediction and control, yet a universal approach remains unestablished.

Due to their spatiotemporal localization, abrupt phenomana exhibit broad spectra, leading to a high number of degrees of freedom in Fourier mode analysis. Understanding the fundamental processes requires a decomposition with fewer degrees of freedom. Singular value decomposition (SVD) provides an optimal mode decomposition based on orthogonal bases. Furthermore, extensions of SVD for multiple fields have been proposed [3], along with classification methods based on pattern similarity in SVD modes [4].

In this study, we apply Multi-field SVD, an extended version of SVD, to identify modes contributing to intermittent transport.

2. Multi-field SVD

SVD is a diagonalization method for general matrices and can be expressed for an observed data matrix as:

$$X(\boldsymbol{x},t) = \sum_k u_k \sigma_k v_k^* \tag{1}$$

where u_k, v_k correspond to the spatial structure and temporal evolution of mode k, respectively, while the singular value σ_k indicates the contribution of the mode. Each mode is decomposed based on an orthogonal basis.

When analyzing particle transport, which involves correlations between multiple physical quantities, applying SVD separately to each quantity may result in different bases being chosen, causing interference between modes. To address this, we apply SVD to $X(\boldsymbol{x},t), Y(\boldsymbol{x},t)$, which concatenates different physical quantities and along the time direction:

$$F = (X(\boldsymbol{x},t_1), \cdots X(\boldsymbol{x},t_n), Y(\boldsymbol{x},t_1) \cdots Y(\boldsymbol{x},t_n)) \tag{2}$$

This approach, known as Multi-field SVD, allows extraction of common spatial bases shared among different physical quantities [3].

In this study, we apply Multi-field SVD to data from Kelvin-Helmholtz turbulence simulations obtained using the Numerical Linear Device (NLD) code, which employs a three-dimensional reduced fluid model with vorticity sources [5]. The dataset consists of density and electrostatic potential fields, along with the vorticity field computed from the electrostatic potential. Multi-field SVD is applied to these three physical quantities.

3. Abrupt Transport Analysis

We applied Multi-field SVD to the density field, electrostatic potential field, and vorticity field. Based on mode similarity, clustering is performed to classify modes into four degrees of freedom: background mode (A), zonal flow mode (B), coherent mode (C), and incoherent mode (D) [4]. The distance between modes was defined using the singular value distribution, and modes with close components were grouped into the same class. Transport was evaluated using the density N_α of mode α and the radial flow $V_{r\beta}$ of mode β, given by:

$$\Gamma_{r\alpha\beta} = N_\alpha V_{r\beta} \tag{3}$$

where $V_{r\beta}$ was computed from the azimuthal derivative of ϕ, assuming $E \times B$ drift. The results indicate that incoherent mode (D) predominantly contributes to intermittent transport [7].

4. Driving Mechanism of Incoherent Mode

Previous studies on structure formation have focused on 2nd-order nonlinearities such as Reynolds stress [6]. However, in our model, the vorticity equation:

$$\frac{\partial \Omega}{\partial t} + [\phi, \Omega] = -\nabla N \cdot [\phi, \nabla_\perp \phi] + LF \tag{4}$$

requires the consideration of 3rd-order nonlinear terms to satisfy charge conservation. The ratio of 2nd-order to 3rd-order nonlinear terms is given by: $\nabla N \cdot [\phi, \nabla_\perp \phi] / [\phi, \Omega] \approx 1/k_r L_n$. Where $1/k_r$ is the turbulence wavelength, and L_n is the density gradient length. When $1/k_r$ L_n and are comparable, the influence of 3rd-order nonlinear terms cannot be ignored.

Each mode's energy evolution equation is given by:

$$\frac{dE_\zeta}{dt} = J_2(\zeta) + J_3(\zeta) + LE_\zeta \tag{5}$$

$$J_2(\zeta) = \int \phi_\zeta \, [\phi, \Omega] d^2x \tag{6}$$

$$J_3(\zeta) = \int \phi_\zeta \, \nabla N \cdot [\phi, \nabla_\perp \phi] d^2x \tag{7}$$

Where $J_2(\zeta),\ J_3(\zeta)$ represent energy transfer from 2nd- and 3rd-order nonlinear terms, respectively. Our analysis shows that 3rd-order nonlinear terms contribute significantly to all modes. As an example, Figure 1 illustrates the contribution of both nonlinear terms to incoherent mode, revealing that 3rd-order nonlinear interactions predominantly drive its excitation.

Additionally, we investigated mode interactions in third-order nonlinear terms using SVD modes:

$$J_3(\zeta) = \int \phi_\zeta \, \nabla N_\alpha \cdot \left[\phi_\beta, \nabla_\perp \phi_\gamma\right] d^2x \tag{8}$$

We analyzed the dominant mode combinations driving Incoherent mode ($\zeta = D$). Dominant coupling is shown in figure 2. The results indicate that (α , β , γ) coupling between steady-state density gradients and fluctuating flows is crucial for incoherent mode formation [8].

5. Conclusion

We applied Multi-field SVD to three-dimensional reduced simulation data of cylindrical plasmas and identified dominant modes contributing to abrupt transport. Clustering analysis classified modes into four degrees of freedom, confirming that incoherent mode predominantly drives abrupt transport. Furthermore, comparison of 2nd- and 3rd-order nonlinear terms revealed that 3rd-order nonlinear interactions cannot be neglected in any mode. Finally, we demonstrated that the coupling between steady-state density gradients and fluctuating flows is a key factor in the formation of incoherent mode.

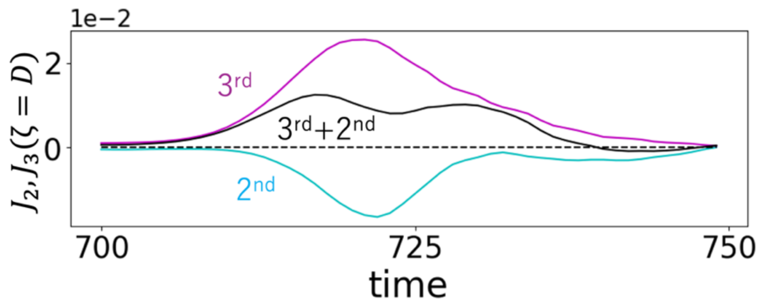

Figure 1 Contribution to the incoherent mode by nonlinear terms. (Red: 3rd-order, Blue: 2nd-order, Black: 3rd + 2nd) [7].

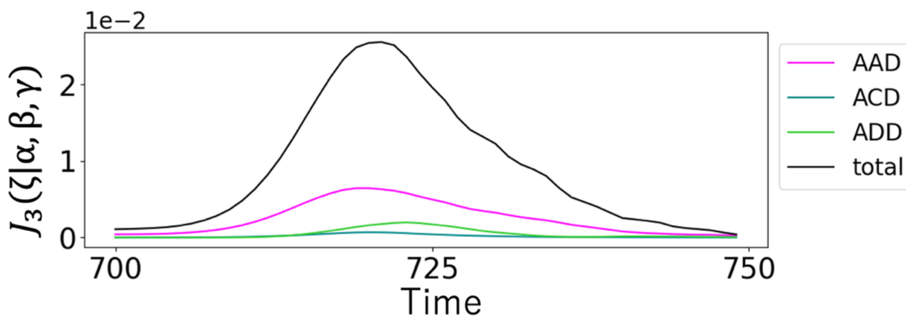

Figure 2 Contribution to the incoherent mode by mode coupling [8].

Acknowledgment

This work was partly supported by a grant-in-aid for scientific research of JSPS, Japan (JP21K03509, JP24K06997), the collaboration programs of NIFS (NIFS23KIST044, NIFS23KIIT002, NIFS24KIPS005, NIFS23KUHL114), and that of RIAM Kyushu University (2024S2-CD-2).

References

[1] D.F. Kong, et al., Nucl. Fusion, 59, 016016 (2019).
[2] P. H. Dimond, et al., Phys. Plasmas, 2, 3640 (1995).
[3] T. Kodahara, et al., Plasma Fusion Res. 18, 1202036 (2023).
[4] A. Okuno, et al., Plasma Fusion Res., 19, 1201035 (2024).
[5] M. Sasaki, et al., Phys. Plasmas, 26, 042305 (2019).
[6] M. Sasaki, et al., Plasma Phys. Control. Fusion, 63, 025004 (2021).
[7] T. Kodahara, et al., Plasma Phys. Control. Fusion, to be submited (2025).
[8] T. Kodahara, et al., in preparation (2025).

Analysis of MHD instabilities using mode decomposition in tokamak plasmas

Yusuke KAWAMURA[1], Naohiro KASUYA[1,2], Masahiko SATO[3], Makoto SASAKI[4]

IGSES, Kyushu Univ.[1], RIAM, Kyushu Univ.[2], NIFS[3], CIT,Nihon Univ[4]

1 Introduction

In order to maintain a steady state in a tokamak plasma, it is essential to understand the MHD instabilities that lead to plasma disruption. In recent years, a new analytical method DMD (Dynamic Mode Decomposition) has been attracting attention[1]. DMD obtains eigenmodes and eigenfrequencies from time-series data, and is used for data analysis including dimensionality reduction and time evolution prediction. In this study, we apply DMD for MHD simulations of tokamak plasmas to evaluate mode interactions. DMD analyses here are rather qualitative ones, and additional analyses with other methods are also carried out.

2 Simulation Method

The target plasma in this analysis is that for 'PLATO' tokamak[2], which is an experimental device in Kyushu University. The plasma parameters are as follows: major radius $R = 0.7$ (m), minor radius $a = 0.2$ (m), toroidal magnetic field $B_t = 0.3$ (T), plasma current $I_p = 40$ (kA), ellipticity $\kappa = 1.6$, triangularity $\delta = 0.3$.

The MHD instabilities analyzed here are caused by effects of a plasma pressure gradient and plasma current. Two kinds of instabilities appear in our PLATO simulations. The first one is a kink mode, in which a twist in the plasma increases due to the effect of the magnetic field created by the plasma current, leading to a major collapse of the plasma. The second one is a ballooning mode, which causes a localized bulge due to a pressure gradient.

The simulations use 'MIPS' code[3], which solves the following set of the MHD equations to show 3-D plasma behavior in space.

$$\rho\frac{\partial v}{\partial t} = \rho\omega \times v - \rho\nabla(\frac{v^2}{2}) - \nabla p + j \times B + \frac{4}{3}\nabla[vp(\nabla \cdot v)] - \nabla \times [v\rho\omega]$$

$$\frac{\partial p}{\partial t} = -\nabla \cdot (pv) - (\gamma - 1)p\nabla \cdot v + \chi\nabla^2(p - p_{eq}) + (\gamma - 1)[v\rho\omega^2 + \frac{4}{3}vp(\nabla \cdot v)^2 + \eta j \cdot (j - j_{eq})]$$

$$\frac{\partial B}{\partial t} = -\nabla \times E$$

$$\frac{\partial \rho}{\partial t} = -\nabla \cdot (\rho v)$$

$$E = -v \times B + \eta j$$

$$j = \frac{1}{\mu_0}\nabla \times B$$

$$\omega = \nabla \times v$$

The initial equilibrium fields required for the MHD simulation is calculated by using the integrated transport simulation code 'TASK'[4]. Three conditions with different q and β values are used: (1)$q = 0.8, \beta_0 = 3.5$ (both kink and ballooning modes appear), (2)$q = 0.8, \beta_0 = 0.5$ (only kink mode), (3)$q = 1.2, \beta_0 = 2.0$ (only ballooning mode).

3 Mode analysis

3.1 DMD (Dynamic Mode Decomposition)

DMD obtains eigenmodes and their temporal growth rates from time series data using the following representation:

$$\boldsymbol{\psi}_t \sim A^t \boldsymbol{\psi}_0 = \sum_{i=1}^{M} \boldsymbol{\varphi}_i \boldsymbol{u}_i^t \alpha_i$$

where $\boldsymbol{\psi}_t$ is the observation vector at time t, $\boldsymbol{\varphi}_i$ is DMD modes, $\boldsymbol{u}_i$ is DMD eigenvalues (growth rate) and α_i are contribution rates. $\boldsymbol{\psi}_t \sim A^t \boldsymbol{\psi}_0$ represents the assumption that the observation vector at all times evolves linearly from the initial observation vector, and each growth rate represents an exponential evolution and oscillation[5].

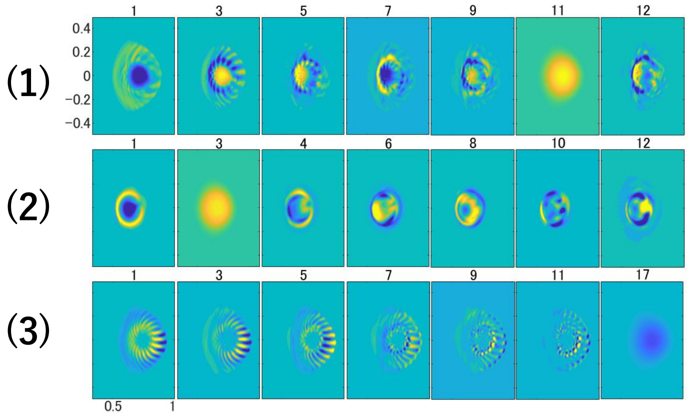

Fig.1 DMD modes in three conditions

Figure 1 shows the DMD eigenmodes in three conditions; (1) both kink modes and ballooning modes, (2) only kink modes, (3) only ballooning modes. Figure 1 (1)-11, (2)-3 and (3)-17 show eigenmodes that correspond to the background profile, and do not grow and decay over time. Eigenmodes with smaller index numbers than that of the background mode are growing modes, and those with larger index numbers are decaying modes. In addition, as the mode number increases, the oscillation frequency of the growth rate increases.

The ballooning mode is extracted in Fig.1 (1)-1 and (1)-3, which have smaller oscillation frequency of the growth rates than those of the kink mode extracted in Fig.1 (1)-5 and (1)-7. This corresponds to the time evolution in which the ballooning mode changes slowly compared to the kink mode.

Figure 2 shows the time evolution of the eigenmode(1)-3. The kink mode expands to inward (high field side) and outward (low field side) of the torus in the top and bottom rows, respectively. The high-pressure region near the plasma center moves inwards (or outwards) by the kink mode, eventually

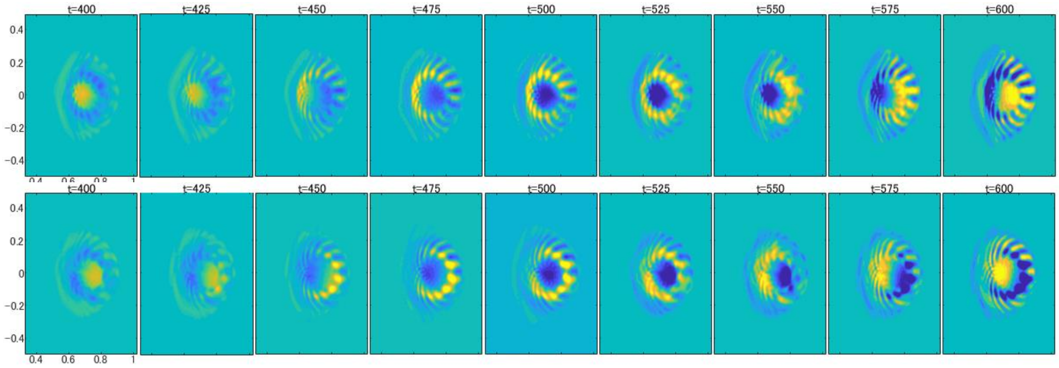

Fig.2　time evolution of the DMD mode (1)-3

reaching the region where the ballooning mode is excited, suggesting energy transfer between the kink and ballooning modes.

It is necessary to confirm the visual (qualitative) considerations obtained from the DMD by other quantitative analyses. Methods such as Fourier Mode Decomposition (FMD) and Singular Value Decomposition (SVD) are used for this consideration.

3.2 FMD (Fourier Mode Decomposition)

Fourier decomposition is a method to analyze frequency or wavenumber characteristics by converting time-series or spatial-variation data. Here, we used Fast Fourier Transform (FFT), which performs discrete Fourier decomposition with high computational speed. Figure 3 shows the results of FMD in condition (1). The red lines show the time evolution of the radial mode structure of the kink mode, and the green, blue and yellow lines are those of the higher wavenumber components consisting the ballooning modes. The dotted line in Fig.3 shows the radial position of $q = 1$ rational surface.

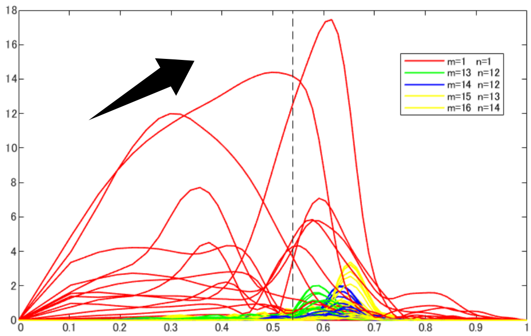

Fig.3　Time evolution of FMD modes in condition (1)

In Fig.3, it can be seen that the kink mode is excited at $r \sim 0.3$, which propagates outwards to the region with $r \sim 0.6$. The amplitude of the kink mode becomes small after reaching the region with $r \sim 0.6$, where the ballooning mode exist. The mode amplitude of the kink mode may be suppressed by the presence of the ballooning modes.

In the other simulation with large plasma current, the kink mode propagates to outer region. This is because the growth rate of the kink mode becomes larger, and the effect of the ballooning mode is negligibly small. The kink mode passes thorough the ballooning mode region before the ballooning mode becomes sufficiently large. This suggests that conditions such as the plasma current affect the interaction between the kink and ballooning modes. Their interaction should be investigated quantitatively by evaluating energy transfer between the modes.

3.3 SVD (Singular Value Decomposition)

SVD is the method decomposing time series data into the following form;

$$\boldsymbol{\phi}_t = \sum_{i=1}^{p} s_i \boldsymbol{u}_i \boldsymbol{v}_i^t$$

where, $\boldsymbol{\phi}$ is the observation quantities at time t, and s_i, $\boldsymbol{u}_i$ and $\boldsymbol{v}_i$ correspond to singular values, SVD modes and SVD eigenvalues, respectively. Unlike DMD, there is no assumption that each observed vector evolves linearly from the initial vector.

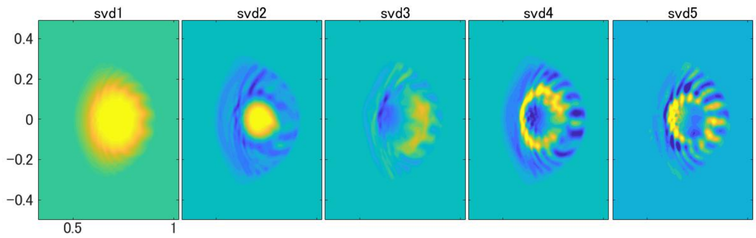

Fig.4 SVD modes when the kink and ballooning modes exist with the condition (1)

Figure 4 shows the result applying SVD to the time series data with the kink and ballooning modes in condition (1). The eigenmode svd1 corresponds to the mean pressure profile, which is almost stationary. Other modes are extracted as a mixture of kink mode and ballooning mode patterns.

There is other researches showed a clear role of each mode by using SVD[6]. Periodic oscillation with a small number of dominant modes can be clearly identified by this method, for example, but the phenomenon in this case is not repetitive, so the SVD eigenvalues also include characteristic time evolution. SVD modes are orthogonal to each other, so the energy transfer between SVD modes can be evaluated[7]. Development of the method is necessary to be applied to this kind of strong mixture mode case.

References

[1] 黒田侑. トカマクプラズマにおける MHD 不安定性の三次元構造の解析. プラズマ・核融合学会九州・沖縄・山口支部第 25 会支部大会,Vol. 18pA03, 2021.

[2] Akihide Fujisawa. Past and present experiments toward plato project. AIP Conf. Proc., Vol. 1993, No. 1, 2018.

[3] Yasushi TODO et al. Simulation study of ballooning modes in the large helical device. Plasma and Fusion Research, Vol. 5, No. S2062, 2010.

[4] http://bpsi.nucleng.kyoto-u.ac.jp/task/

[5] 草場彰, 久保山哲二. 動的モード分解におけるモード数低減手法の実験的比較. 人工知能学会研究会資料 人工知能基本問題研究会,Vol. 110, p. 01, 2019.

[6] M.Sasaki et al. Evaluation of abrupt energy transfer among turbulent plasma structures using singular value decomposition. Plasma Physics and Controlled Fusion, Vol. 63, No. 025004, 2021.

[7] S.Maeyama et al. On the triad transfer analysis of plasma turbulence: symmetrization, coarse graining, and directional representation. New Journal of Physics, Vol. 23, No. 043049, 2021.

Real-time prediction model and adaptive predictive control of LHD plasmas

[1]Y. Morishita, [1]S. Murakami, [2]N. Kenmochi, [2]H. Funaba, [2]Y. Mizuno, [2]K. Nagahara, [2]M. Yokoyma, [3]G. Ueno, and [2]M. Osakabe

[1]Department of Nuclear Engineering, Kyoto University, Kyoto, Japan
[2]National Institute for Fusion Science, National Institutes of Natural Science, Gifu and Aomori, Japan
[3]The Institute of Statistical Mathematics, Research Organization of Information and Systems, Tokyo, Japan

INTRODUCTION

The operation of future fusion reactors requires nonlinear and multivariate control of fusion plasma behavior under conditions of limited measurement. However, a predictive model (digital twin) essential for such complex control generally involves large uncertainties because it is inherently difficult to model all the components affecting the plasma behavior and their interactions with sufficient accuracy. To address this challenge, we are developing an analysis and control system, ASTI, based on a data assimilation framework that integrates model adaptation and control estimation [1]. Typical data assimilation is a statistical method to estimate the state vector, which consists of the variables in a numerical model, based on observation data and can make the behavior of the model similar to that of the real system. In addition to the state estimation, our data assimilation framework includes estimation of control input that leads the system state to the target state, which allows ASTI to achieve adaptive predictive control. The effectiveness of this control approach was demonstrated through a simple control experiment in LHD [2]. ASTI approximates the probability distribution of the state vector with a number of ensemble members (simulations with slightly different conditions) to realize its time evolution and the data assimilation computation. ASTI can control both observable and unobservable variables and can be applied to complex control with multiple variables. It is difficult to achieve a comprehensive control system in which many observations and actuators are harmoniously combined simply by combining conventional controllers, such as PID controllers. In ASTI, physical knowledge and control constraints can be easily incorporated into the control system through the state vector and the digital twin.

CONTROL SYSTEM IN LHD

To investigate the control performance of ASTI for complicated control problems, we have built a control system based on ASTI at LHD. We employ the integrated simulation code, TASK3D, as the digital twin of the LHD plasma in ASTI. The neutral beam injection (NBI) heating, electron cyclotron heating (ECH), and gas-puff systems are connected to ASTI as the actuators to control the plasma density and temperature. ASTI adjusts on/off of the four neutral beams, on/off of the five gyrotrons, and the valve voltage of the gas-puff every 0.3 seconds. Reaction of the LHD plasma is observed as the radial profiles of electron temperature and density by the real-time Thomson scattering measurement system [3] and the profiles are assimilated into the state distribution every 0.3 seconds. ASTI runs on a vector machine (128 parallel processes, maximum 384 ensemble members) or a part of Plasma Simulator RAIJIN (6144 parallel processes, maximum 12288 ensemble members). We have applied this control system to control problems such as radial profile control of electron temperature, simultaneous control of electron density and temperature, and simultaneous control of electron temperature and ion temperature.

CONTROL EXPERIMENTS

Here, we show the results of the simultaneous control of electron temperature and ion temperature. The target variables of this experiment are the electron temperature T_e (at normalized minor radius ρ=0 and 0.25) and the ion temperature T_i (ρ=0.25). The actuators are the NBI heating and the ECH which has two separate heating positions to control the radial profile of electron temperature: two gyrotrons (total ~700 kW) for ρ=0 and the other three (total ~1500 kW) for ρ=0.4. Factors for the electron and ion thermal diffusivities and parameters in the NBI heating model are included in the state vector and optimized by assimilating the observed T_e and T_i. The constant model and the gyro-Bohm model are employed for the electron and ion thermal diffusivities, respectively, based on the previous LHD experimental data. Figure 1 shows the results of a control experiment (shot number 193553). The target T_e is 3 keV (both ρ=0 and 0.25), and the target T_i varies stepwise, as shown by the red dashed line in Fig. 1(b). It can be seen from Fig. 1(a) and (b) that the T_e reaches the target temperature quickly from the start of the control, and the ion temperature also increases following the target temperature. The assimilation of observations optimizes the model parameters and improves both the prediction

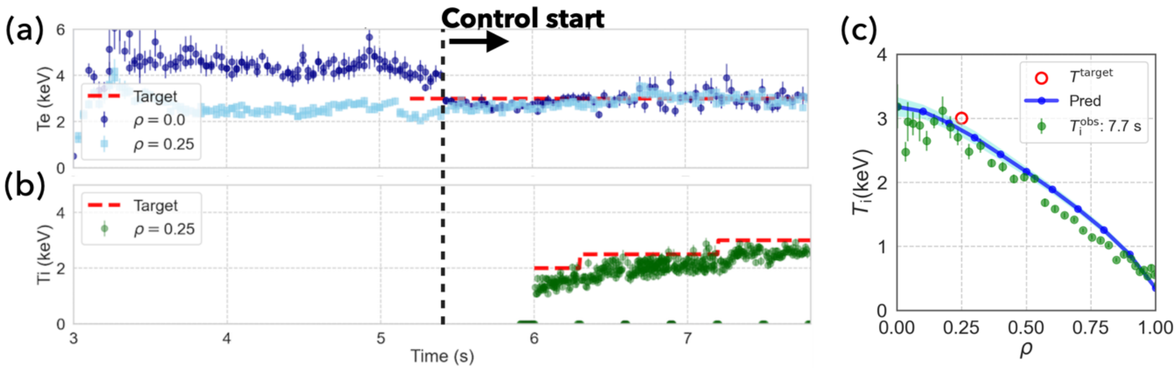

Fig. 1: Results of an experiment to control the electron and ion temperatures using NBI heating and ECH. (a) Control result of electron temperature at ρ=0 and 0.25. (b) Control result of ion temperature at ρ=0.25. The red dashed lines represent the target temperatures. (c) Radial profiles of predicted electron temperature and the observation at t=7.7 s. The hatching area around the prediction profile represents the standard deviation of the predicted distribution.

performance of the digital twin and the control performance. Figure 1(c) shows the predicted and observed radial profile of T_{i}. We can see good agreement between the prediction and the observations. Note that the plotted observations of the ion temperature in Figs. 1(b) and (c) were obtained after the experiment and not in real time. Multivariate predictive control involving unobserved variables has been achieved by combining the digital twin prediction, which captures the characteristics of the LHD plasma, with the actual partial observations. We have also confirmed the effectiveness of this data assimilation-based control approach for other control problems, such as radial profile control of electron temperature and simultaneous control of electron density and temperature.

CONCLUSION

This study has demonstrated the effectiveness of the data assimilation-based control using ASTI, which compensates for the imperfections of the digital twin using real-time observations and addresses complex multivariate control problems involving unobserved variables. This approach can construct a comprehensive control system for fusion plasmas by synergistically integrating physical knowledge (including data-driven models), various real-time observations, and actuators. ASTI can also contribute to controls that require avoiding terminating events by implementing relevant alarm rates and physics experiments that require a high degree of control. ASTI is currently being extended for control of tokamak plasmas, and actual digital twin control experiments are planned. ASTI can realize nonlinear and multivariate control of fusion plasma behavior under conditions of limited measurement and provide a foundation for flexible control of fusion reactors.

[1] MORISHITA Y. et al., Data assimilation and control system for adaptive model predictive control, J. Comput. Sci. **72** (2023) 102079.

[2] MORISHITA Y. et al., First application of data assimilation-based control to fusion plasma, Sci. Rep. **14** (2024) 137.

[3] FUNABA H. et al., Electron temperature and density measurement by Thomson scattering with a high repetition rate laser of 20 kHz on LHD, Sci. Rep. **12** (2022) 15112.

Extension of the data assimilation system ASTI for the real-time prediction of tokamak plasmas
トカマクプラズマの実時間予測に向けたデータ同化システム ASTI の拡張

Ryu ICHIKAWA, Yuya MORISHITA, Emi NARITA, Mitsuru HONDA, Sadayoshi MURAKAMI

Kyoto University

1 Backgrounds

Integrated simulation has been developed to predict and analyze the behavior of plasmas, and to design a burning plasma operation scenario. Real-time and control-oriented predictions of tokamak plasmas have also been achieved using integrated simulation codes. However, modules in integrated simulation codes have uncertainties that arise from various approximations and assumptions of the physical model. The uncertainties interact each other and negatively impact the simulation results. There are also a lot of physical phenomena that are not considered in a code. For these reasons, predictions from integrated simulations often do not match the actual plasma behavior.

To address these issues, we have introduced data assimilation technique, which has been studied mainly in the fields of meteorology and oceanography for accurate forecasts, to integrated simulation. We have developed a data assimilation system ASTI for accurate prediction and control of fusion plasmas[1].

ASTI was originally developed for helical plasmas, but we are expanding it for transport control of tokamak plasmas.

2 Transport simulations using data assimilation

DA is a method to improve the simulation accuracy by optimizing the simulation model using information from the actual observations. ASTI employs the ensemble Kalman filter as the DA scheme. We employ the integrated simulation code TASK as the simulation model. TASK solves the 1-D diffusive transport equations of particles and energy:

$$\frac{\partial}{\partial t}(n_s \mathcal{V}') = -\frac{\partial}{\partial \rho}\left(\mathcal{V}'\Gamma_s\right) + S_s\mathcal{V}', \tag{1}$$

$$\frac{\partial}{\partial t}\left(\frac{3}{2}n_s T_s \mathcal{V}'^{5/3}\right) = -\mathcal{V}'^{2/3}\frac{\partial}{\partial \rho}\left(\mathcal{V}' Q_s\right) + P_s\mathcal{V}'^{5/3}. \tag{2}$$

Time evolution of temperature and density of electrons and hydrogen ions are calculated from the equations above. Each time the observations are gained, data assimilation is performed and the model parameters of TASK are optimized to improve the prediction accuracy.

In this study, a predictive simulation of NBI heated plasma of JT-60U(shot 44180)[2] is performed. We optimize temperature, density, thermal and particles diffusivity, particles pinch velocity, and heat and particle source term by data assimilation, using the experimental measurements of temperature and density.

The comparison of prediction results from a simulation without data assimilation and a simulation in which the model is optimized by the data assimilation is shown in 1. In this simulation, time evolution of MHD equilibrium is not calculated in the code, and the pre-analyzed data is loaded. It is seen from the graph that the predictive accuracy has been improved significantly using the data assimilation technique.

3 Introduction of the magnetic field diffusive equation

To accurately evaluate transport in tokamak plasmas, it is important to accurately calculate the detailed time evolution of the magnetic field. In the simulations presented in the previous section, time evolution of the poloidal field is updated by loading the pre-analyzed data approximately every second. To obtain a more detailed time evolution of the poloidal field, the magnetic field diffusion equation is introduced.

$$\begin{aligned}\frac{\partial B_\mathrm{p}}{\partial t} = \frac{\partial}{\partial \rho}\Bigg[&\frac{\eta_\parallel}{\mu_0}\frac{F}{\mathcal{V}'\langle R^{-2}\rangle}\frac{\partial}{\partial \rho}\left(\frac{\mathcal{V}'}{F}\left\langle\frac{|\nabla\rho|^2}{R^2}\right\rangle B_\mathrm{p}\right)\\ &-\frac{\eta_\parallel}{FR_0}\frac{|\nabla\rho|^2}{\langle R^{-2}\rangle}\langle JB\rangle\Bigg]\end{aligned} \tag{3}$$

This equation enables the poloidal field B_p to be updated at each time step of transport calculation (approximately every 0.001 seconds) since this equation is solved simultaneously with Eqs.(1, 2).

To optimize the calculation of Eq.(3) by data assimilation as well as the calculation of the other equations, we assimilate the neoclassical bootstrap current obtained from the analysis based on the observations. The prediction of the poloidal field is modified by this optimization. It is seen from Fig.2 that as the bootstrap current profile is modified using observation-based analysis, the poloidal field profile is also modified based on correlations. Bootstrap current and poloidal field have a strong

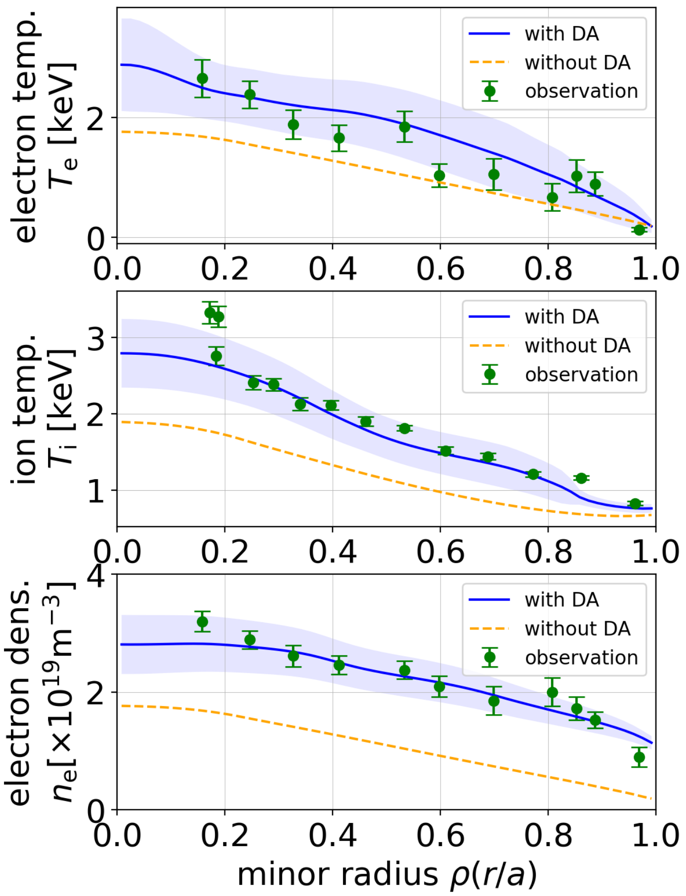

Fig. 1: Predicted radial profiles of electron temperature, ion temperature, and electron density. The dashed lines show the results from a simulation without data assimilation, and the solid lines show the results from a simulation with data assimilation. The hatched areas around the solid lines represent the standard deviations of probability distribution. The dots with the error bars show the observations.

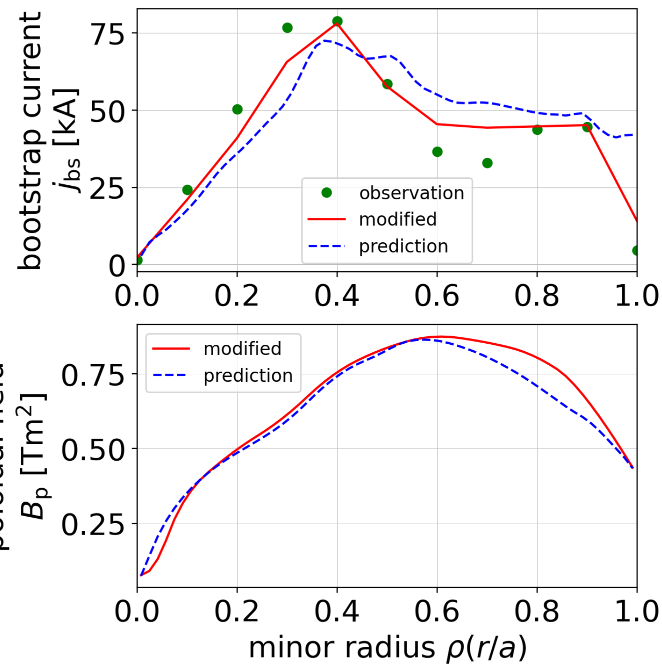

Fig. 2: Modification of the bootstrap current profile and the poloidal field profile. The dashed lines show the predicted profiles, and the solid lines show the profiles modified by the data assimilation. It is seen that the poloidal field profile is modified based on the modification of the bootstrap current profile.

negative correlation, especially in the peripheral region ($\rho \sim 1.0$), so as the bootstrap current density is modified downward in the outer region, the poloidal field is modified upward.

4 Outlooks

In the simulations in this paper, time evolution of equilibrium is not solved in the code, and the precalculated data is loaded dynamically to TASK/TR code. In tokamak simulations, it is important to accurately assess time evolution of magnetic field and equilibrium. Our next step is to extend ASTI to a transport and equilibrium prediction system of tokamak plasmas by implementing an equilibrium code in it.

References

[1] Y. Morishita et al. *Comput. Phys. Commun.*, 274, (2022).

[2] H. Urano et al. *Nucl. Fusion*, 53, (2013).

Extraction of Spatio-Temporal Dynamics of Geodesic Acoustic Modes and its Turbulence Modulation by Using Conditional Average

K. Ozawa[1)], M. Sasaki[1)], Y. Hara[1)]

[1)]*Collage of Industrial Technology, Nihon University, Narashino 275-8575, Japan*

1. Introduction

Particle and heat transport in magnetically confined plasmas are governed by the nonlinear processes of turbulence driven by the plasma inhomogeneities. Turbulence often drives large scale structures nonlinearly, such as zonal flows and streamers etc. The spatio-temporal behavior of the transport is determined by the interaction among turbulence, large scale structures and background plasma profiles[1]. As a consequence of the interaction, the turbulence sometimes shows ballistic propagation phenomena, known as the avalanches and/or turbulence spreading. Recent theoretical works have reported that the geodesic acoustic modes (GAMs) capture the turbulence and propagate with each other, and this turbulence trapping is one of the key important physical mechanisms to drive the ballistic turbulence transport[2,3]. Thus, the validation of the turbulence trapping by the GAMs is strongly required. In this study, we aim to extract the spatio-temporal dynamics of GAMs and its turbulence modulation, and to validate the turbulence trapping mechanisms. Conditional average is applied to an experimental data obtained in JFT-2M tokamak, and to a set of data calculated from the gyro-kinetic simulation.

2.Analysis Data

The analysis is based on electrostatic potentials measured using a Heavy Ion Beam Probe (HIBP) in the JFT-2M tokamak fusion test device (major radius R=1.3m, minor radius a=0.3 m). The target plasma conditions are as follows: toroidal field B=1.2 T, plasma current I_p =190 kA, neutral beam injection (NBI) heating power of P_{NB} =750 kW, line-averaged electron density $\langle n_e \rangle = 1.1 \times 10^{19} m^{-3}$, and a flux surface safety factor. The data are measured simultaneously at four spatial points within the device, with precise measurement positions determined on a shot-to-shot basis. Radial dynamics in the L-mode of JFT-2M are extracted from the HIBP signal using the conditional averaging method. Additionally, the results are compared with simulations. The simulation used in this study is the GyroKinetic Vlasov code (GKV), a local turbulent transport simulation. The frequency spectrum from GKV is shown in Fig.1, where a peak around 20 kHz is observed, corresponding to the theoretically predicted GAM spectrum. In addition to the JFT-2M conditions, the simulation parameters are as follows: reference temperature Tref=1.7, collision frequency ν =1.0, temperature gradient L_{ref}/L_{T_s}=6.92, and density gradient L_{ref}/L_{n_s}= 2.22. Here, the subscript “ref” denotes the reference value, L_{ref} represents the major radius.

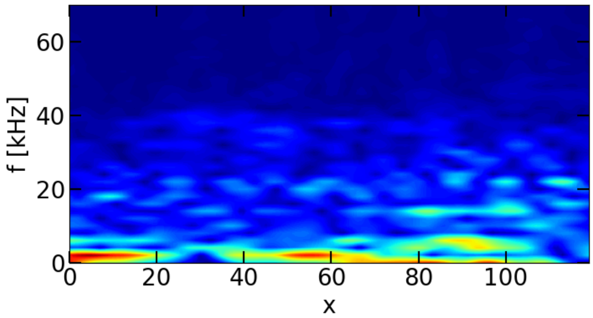

Fig.1 Frequency Spectrum of Electrostatic Potential Simulation

3. Conditional Average

The conditional average method is used as the statistical approach in this study [4,5,6]. The method is performed as follows. First, an initial template $x_{j=0}(t')$ is prepared for $-T/2 < t' < T/2$. Here, we assume a simple sine wave, and j represents the number of iterations. The correlation between $x_{j=0}(t')$ and the analyzed data $y(t)$ is then calculated for each period of $x_{j=0}(t')$.

$$C_j(t) = \int_{-\frac{T}{2}}^{\frac{T}{2}} \frac{1}{\sigma_y(t)\sigma_x} \left(y(t-t') - \bar{y}(t)\right) \cdot \left(x_j(t') - \bar{x}_j\right) dt' \tag{1}$$

Where $\sigma_y(t)$ and σ_x are the standard deviations of $y(t)$ and $x_j(t')$, respectively. The time at which the calculated $C_j(t)$ reaches its maximum correlation is identified as the trigger. The observed data corresponding to this trigger are then extracted over one period of $x_{j=0}(t')$. The initial templates are obtained by averaging these extracted waveforms. The conditional average is then calculated using the following formula, where $t_{peak,j}(i)$ represents the j-th iteration for the i-th trigger.

$$x_{j+1}(t') = \sum_i \frac{y(t - t_{peak,j}(i))}{n} \tag{2}$$

where n represents the total number of triggers. We obtained $x_{j+1}(t')$ is used for iteration until j-th converges. The converged waveform is a statistically certain nonlinear waveform.

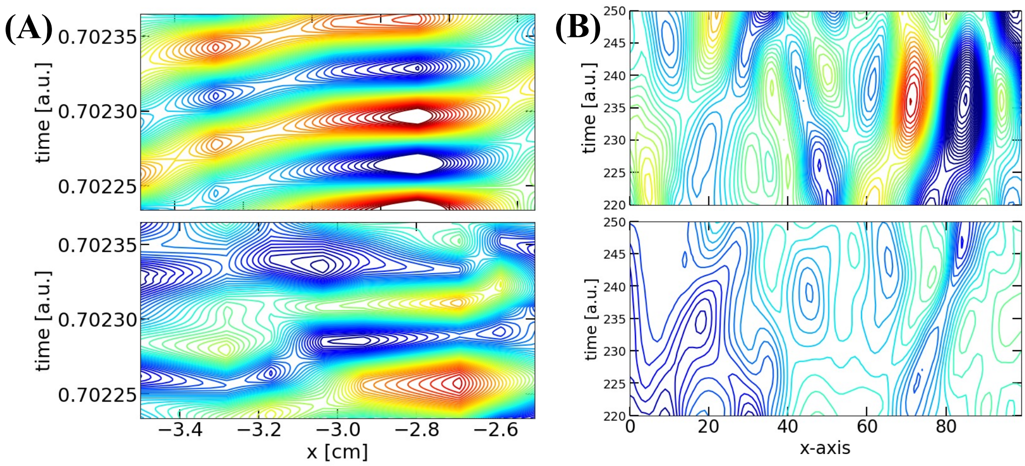

Fig.2 Radial dynamics in (A) JFT-2M, (B) GKV

4. Analysis results

The radial dynamics in JFT-2M were analyzed. Since a GAM period was observed in the Dα signal obtained from outside the device, this signal was used as a trigger to apply the conditional average method to the HIBP signal. The radial dynamics of GAMs and turbulence in JFT-2M are shown in Fig.2(A). The turbulence intensity, modulated by the GAM, propagates and oscillates at the same velocity as the GAM. Next, the spatio-temporal behavior observed in simulations was examined. The radial dynamics of the GAM and turbulence in the GKV simulation is shown in Fig.2(B). As seen in Fig.2(B), the GAM and turbulence propagate with the same phase. This confirms that the structure of GAMs and turbulence propagating at the same velocity, as observed in the experimental data, is also reproduced in the simulation. These results are consistent with the turbulence-trapping mechanism predicted by wave-kinetic theory.

5. Summary

In this study, the statistical method of conditional average was used to analyze the spatiotemporal behavior of GAMs and turbulence. Electrostatic potential data from HIBP measurements of the JFT-2M tokamak were used for analysis. By applying conditional average to the HIBP signal, triggered by the Dα signal, the radial dynamics of JFT-2M were extracted, revealing the structure of GAMs and turbulence propagating at the same velocity. A similar structure was observed in simulations, and the phase relationships were found to be consistent with the turbulence-trapping mechanism predicted by wave-kinetic theory.

References

[1]Diamond, Patrick H., et al. Plasma Physics and Controlled Fusion 47.5 (2005)

[2]Sasaki, Makoto, et al. Physics of Plasmas 25.1 (2018)

[3]Garbet, Xavier, et al. Physics of Plasmas 28.4 (2021)

[4]Kawachi, Yuichi, et al., Plasma and Fusion Research 14 (2019)

[5]Inagaki, Shigeru, et al., Plasma and Fusion Research 9 (2014)

[6]Kin, Fumiyoshi, et al., Plasma and Research 14 (2019)

Estimation of global turbulence profile from partial measurements by using Generative Adversarial Networks for drift waves

R. Kazami and M. Sasaki

Nihon University

1. Introduction

The global turbulent structure of plasmas is crucial for understanding phenomena such as avalanches [1,2], turbulence spreading [3], turbulence trapping [4], the global structure formation in response to instantaneous plasma changes [5], and the formation of streamer structures [6]. However, conventional measurement techniques (e.g., electrostatic probes, HIBP, Doppler reflectometers, and PCI) are limited to local observations, making global observation challenging. In addition to direct measurements, mathematical approaches like tomography have also been proposed, but they have been highly dependent on experimental devices that require a large glass port [7], limiting the adaptability of this method. Given this background, data-driven estimation methods have gained attention as general-purpose estimation techniques, although previous studies mainly focused on one-dimensional distributions of electron density and ion temperature [8,9]. In this study, we propose a novel approach using a generative adversarial network (GAN) to reconstruct global turbulence structures based on locally measured physical quantities from external plasma diagnostics.

2. Generative adversarial networks (GAN)

GAN consists of two neural networks, the Generator and the Discriminator, which compete against each other. This adversarial learning framework enables a wide range of image processing tasks, including realistic image generation, super-resolution, and style transfer. The applications of GAN have expanded across various fields of physics, including anomaly detection [10] and tomographic image reconstruction [11].

This study aims to estimate the global turbulence profile from local measurement data using Pix2Pix [12], a type of conditional GAN. The Generator estimates the global turbulence field by complementing local measurement data. The Discriminator evaluates whether the generated data (Prediction) aligns with the actual simulation results (Answer) and provides feedback to enhance the Generator's performance. This adversarial learning process improves their performance.

The input data consists of signals of electron density fluctuations based on the Hasegawa-Wakatani (HW) model [13], which the magnetic field chosen to be z-direction and the direction of the gradient of the density is set to be the x-direction. We configured the parameters of this model to achieve a turbulence-dominant state and applied a mask to simulate partial measurements, creating a dataset by removing regions that are difficult to measure. The measurable region in this study corresponds to the electron density distribution on the device wall, as obtained from electrostatic probe measurements. For data generation, conditions in which turbulence is dominant were selected [14]. To ensure stable learning, transient behavior from the initial conditions was excluded, and 15000 snapshots of the spatial distribution of density field fluctuations were extracted after turbulence reached a saturated state at $t = 2000$. The snapshot interval Δt_{save} was set to approximately $\Delta t_{save} \cong 0.2 \cdot T_{turb}$, corresponding to about 3000 turbulence cycles in total, where T_{turb} denotes the turbulence period. For model evaluation, 1500 validation snapshots were selected at regular intervals from $2000 \leq t < 17500$, ensuring that they were not included in the training dataset.

3. Prediction of turbulence

The results of the density field estimation are presented in Figure 1(a). The left panel illustrates the spatial distribution obtained from the simulation, while the right panel displays the estimated distribution produced by the network. The snapshots correspond to estimates derived from local measurement data, with 90% of the difficult-to-measure regions removed. The estimated eddy structures exhibit a high degree of similarity to the answer data in terms of global characteristics, including spatial distribution and scale, with a correlation coefficient of 0.8 when considering temporal evolution.

To validate the estimated turbulence scale, a coherence analysis in the spatial frequency domain was conducted. The coherence between the spatial distribution obtained from the simulation and that estimated by the network was evaluated. The results demonstrate effective estimation, achieving a coherence of approximately 0.6 over a broad wavenumber range, extending to fine structures corresponding to vortex scales around kx=10kx, even when the measurement domain was limited to 10%.

Similarly, estimations were performed for electrostatic potential fluctuations. The estimated spatial distribution is shown in Fig.1(b). The electrostatic potential estimation also demonstrated high accuracy across a broad wavenumber range. The same hyperparameters used for training the model on density field fluctuations were also applied to the potential estimation. These results suggest that a single model can be applied to various simulation datasets.

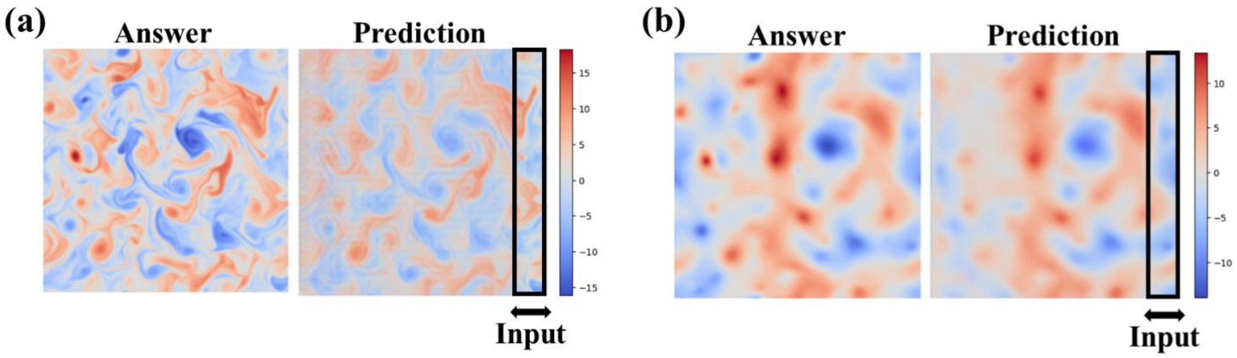

Figure 1. (a) Snapshot of the electron density, Left: simulation data(answer), Right: model output(prediction). **(b)** Snapshot of the electrostatic potential, Left: simulation data(answer), Right: model output(prediction).

4. Summary

In this study, we apply a generative adversarial network (GAN) to local turbulence signals obtained from a two-dimensional reduced fluid model to estimate the global turbulence profile. Furthermore, we perform Fourier analysis to evaluate the estimation accuracy for turbulence wavelengths that can be reconstructed. The results demonstrate that high-precision estimation is feasible over a broad frequency range corresponding to turbulence vortex scales. Similarly, we train the model on electrostatic potential fluctuations using the same hyperparameters and confirm its applicability to various simulations.

Acknowledgement

This work was partly supported by a grant-in-aid for scientific research of JSPS, Japan (JP21K03509, JP24K06997), the collaboration programs of NIFS (NIFS23KIST044, NIFS23KIIT002, NIFS24KIPS005, NIFS23KUHL114), and that of RIAM Kyushu University (2024S2-CD-2).

Reference

[1] P. H. Diamond, *et al*., Plasma Phys. Control. Fusion **47**, R35 (1995)
[2] J. Candy and R. E. Waltz, Phys. Rev. Lett **9**, 045001 (2003)
[3] O. D. Gurcan, *et al*., Phys. Plasmas **12**, 032303 (2005)
[4] M. Sasaki, *et al*., Sci. Rep. **7**, 16767 (2017)
[5] S. Inagaki, *et al*., Nucl. Fusion **53**, 113006 (2013)
[6] T. Yamada, *et al*., Nat. Phys. **4**, 1029 (2008)
[7] C. Moon, et al., Sci. Rep. **11**, 3720 (2021)
[8] T. Nishizawa, *et al*., Plasma Phys. Control. Fusion **65**, 125006 (2023)
[9] Z. Lin, *et al*., Nucl. Fusion **64**, 106061 (2024)
[10] T. Schlegl, *et al*., arXiv:1703.05921v1 (2017)
[11] N. Kenmochi, *et al*. Plasma Fusion Res. **14**, 1202117 (2019)
[12] P. Isola, *et al*, Conf. Comput. Vis. Pattern Recognit., pp. 1125-1134, (2017)
[13] A. Hasegawa and M. Wakatani, Phys. Rev. Lett. **59**, 14 (1987)
[14] R. Numata, *et al*, Phys. Plasmas **14**, 102312 (2007)